Measurement of the breakup probability of $\pi^+\pi^-$ atoms in a Nickel target with the DIRAC spectrometer

Inauguraldissertation

zur

Erlangung der Würde eines Doktors der Philosophie vorgelegt der Philosophisch-Naturwissenschaftlichen Fakultät der Universität Basel

von

Christian Peter Schütz

aus Sumiswald, Bern

Basel, 2004

Genehmigt von der Philosophisch-Naturwissenschaftlichen Fakultät auf Antrag von Prof. Dr. L. Tauscher und Prof. Dr. L. Nemenov

Basel, den 6. April 2004

Prof. Dr. M. Tanner Dekan

Abstract

The DIRAC Collaboration aims to determine the lifetime of the pionium atom, a $\pi^+\pi^-$ bound state, by measuring the breakup probability of such a bound state. This breakup probability measurement with the DIRAC spectrometer at CERN searches for an excess of $\pi^+\pi^-$ pairs from breakup at very low relative momenta (Q < 4 MeV/c) on top of a dominant background coming from correlated and uncorrelated pion pair from the proton beam - target interaction. The number of found $\pi^+\pi^-$ pairs from breakup can be put in relation to the number of produced atoms to yield the breakup probability. The number of produced atoms is related to the number of produced $\pi^+\pi^-$ pairs with Coulomb final state interaction through the production process.

The Nickel target data amounts to the biggest measured homogeneous sample recorded by the DIRAC collaboration, which translates into a small statistical error. Systematical influences are studied and shown to be not dominant.

The measurement of the breakup probability and hence the determination of the lifetime of pionium allows to calculate the difference between the isoscalar and isotensor $\pi\pi$ scattering length using only quantum mechanics. This calculation can be used to cross check the predictions coming from Chiral Perturbation Theory.

Contents

1	Intr	roduction	6		
2	Theory				
	2.1	Theoretical Motivation	8		
	2.2	Scattering of $\pi^+\pi^- \to \pi^0\pi^0$	8		
	2.3	Experimental results on a_0^0 and a_0^2	10		
	2.4	Obtaining a_0^0 and a_0^2 from $A_{2\pi}$	10		
		2.4.1 $A_{2\pi}$ lifetime	11		
		2.4.2 Lifetime predictions	11		
	2.5	Production of pion pairs in high energy collisions	11		
		2.5.1 Coulomb and atomic pairs	12		
		2.5.2 Coulomb and Non Coulomb pairs	15		
		2.5.3 Accidental pairs	17		
	2.6	Interaction of relativistic $A_{2\pi}$ with matter	17		
		2.6.1 Cross section with atoms	17		
		2.6.2 $A_{2\pi}$ breakup probability	17		
		2.6.3 Direct calculation of the break-up probability	18		
		2.6.4 Lifetime dependence of the break-up probability	21		
3	DIR	RAC apparatus	23		
	3.1	General apparatus layout description	23		
	3.2	Proton beam and target station	24		
	3.3	MSGC	26		
	3.4	Scintillation Fiber Detector	27		
		3.4.1 Readout electronics and the PSC circuit	28		
		3.4.2 Performance	29		
	3.5	Ionization Hodoscopes	31		
	3.6	Magnet	34		
	3.7	Drift Chambers	34		
	3.8	Vertical Hodoscopes	37		
	3.9	Horizontal Hodoscopes	39		

CONTENTS 3

	3.10	Cerenk	ov Counters
	3.11	Presho	wer
	3.12	Muon	Counters
4	DIR	AC Trig	ger 47
	4.1	Genera	l Trigger Scheme
	4.2	Pretrig	ger T0
	4.3	First L	evel Trigger T1
	4.4	Neural	Network Trigger DNA
	4.5	Fourth	Level Trigger T4
	4.6	Rate ar	nd Acceptance
5	Data	Acquis	sition System - DAQ 55
	5.1	DAQ h	ardware
	5.2	DAQ s	oftware
6	BAS	EL Tra	cking 58
	6.1	Introdu	ction
	6.2	Kalma	n Filter
		6.2.1	Prediction
		6.2.2	Correction
		6.2.3	Error of Prediction 61
		6.2.4	Optimality Criterion 62
	6.3	Downs	tream track finding and fitting 64
		6.3.1	Selection of track candidates 64
		6.3.2	Track fitting
		6.3.3	Momentum determination I 65
	6.4	Upstrea	am track finding and fitting
		6.4.1	Ambiguity of prompt events 66
		6.4.2	Track finding in SFD X
		6.4.3	Momentum refinement using the SFD X hits 68
		6.4.4	Smearing P_x within one fiber
		6.4.5	Track finding in SFD Y
		6.4.6	Smearing P_y within one fiber
		6.4.7	Track finding in the MSGC
		6.4.8	Target measurement
		6.4.9	Upstream track fitting - Kalman filter procedure 72
		6.4.10	Momentum calculation at the target
		6.4.11	Overview of the BASEL tracking
	6.5	Treatin	g accidentals like prompt events
	6.6	Further	improvements

CONTENTS 4

7	Mon	te Carlo Software Package GEANT	80
	7.1	Generator	80
		7.1.1 Atomic pair generator	82
		7.1.2 Coulomb, non-Coulomb and accidental pair generator	82
	7.2	Detector digitalization	85
		7.2.1 SFD Simulation	86
		7.2.2 VH and HH detectors	88
	7.3	Comparing Monte Carlo data to measured data	89
8	Cali	bration Measurements and Resolution	92
	8.1	Λ decay	92
	8.2	Track reconstruction efficiency and resolution of atomic pairs	93
	8.3	Track reconstruction efficiency and resolution of Coulomb and	
		accidental pairs	97
9	Expe	erimental k-factor	104
	9.1	Calculation	104
	9.2	Results for Nickel 2001	106
		9.2.1 94 μ m target	106
		9.2.2 98 μ m Target	
	9.3	Systematic influences	107
10	$A_{2\pi}$	detection and P_{br} determination	112
	10.1	Variables	112
	10.2	Description of the method	113
	10.3	Event selection	114
	10.4	Background description	115
		10.4.1 Accidental pairs	117
		10.4.2 Coulomb and non-Coulomb pairs	117
	10.5	Atomic pair signal	120
	10.6	Breakup probability	121
	10.7	Fitting with atomic pair shape constraint	124
	10.8	Three hit events	127
	10.9	Finite size correction	130
11	Syste	ematic effects	133
	11.1	Accidental background	133
		Coulomb and non-Coulomb background	
		Additional restrictions in Q_{trans}	
		Atomic pair shape	
	11.5	Influence of multiple scattering	138

GON TENENTE	_
CONTENTS	5

11.6 Summary	140
12 Lifetime determination	143
13 Summary and conclusion	146
References	148
Acknowledgments	153
Curriculum vitae	154
Zusammenfassung	155

Chapter 1

Introduction

The lifetime measurement of the $\pi^+\pi^-$ atom $(A_{2\pi})$ [1] enables to determine in a model independent way the combination $|a_0-a_2|$ of the S-wave $\pi\pi$ -scattering lengths for isospin I=0 and 2 ([2]-[8]). The $\pi\pi$ scattering lengths a_0 , a_2 have been calculated within the framework of Chiral Perturbation Theory [9] by means of an effective Lagrangian with a precision of better than 2.5% [10]. The lifetime of $A_{2\pi}$ in the ground state is predicted to be $\tau=(2.9\pm0.1)\times10^{-15}$ s. These results are based on the assumption that the spontaneous chiral symmetry breaking is due to a strong quark condensate as confirmed recently [11, 12, 13]. An alternative scenario with an arbitrary value of the quark condensate [14] admits larger a_0 , a_2 compared with those of the standard scheme [10]. This is the reason why a measurement of scattering lengths will deepen the current understanding of chiral symmetry breaking in QCD and for verifying the magnitude of the quark condensate.

Based on the double differential two pion production cross sections in proton-nucleus interactions, $A_{2\pi}$ yields have been calculated as a function of the $A_{2\pi}$ energy and angle in the proton energy range from 24 GeV/c to 1000 GeV/c ([15]-[17]). The method for observing $A_{2\pi}$ and to measure their lifetime has been proposed in [15]. Pairs of $\pi^+\pi^-$ are produced as unbound ("free") pairs or with small probability as $A_{2\pi}$. The latter may either annihilate into $\pi^0\pi^0$ or break up into $\pi^+\pi^-$ pairs ("atomic" pairs) after interaction with target atoms. For thin targets $(10^{-3}X_0)$ the relative momentum Q in the atomic pair c.m. system is $Q \leq 3 \text{ MeV/c}$. Their yield is $\sim 10\% \div 20\%$ of the number of free pairs with the same $Q \leq 3 \text{ MeV/c}$. The number of broken-up atoms n_A is a function of the momentum of the atom and depends on the dynamics of the $A_{2\pi}$ interaction with ordinary atoms allows to calculate all the relevant cross sections ([18]-[30]). For a given target material, target thickness and momentum, the theoretical ionization probability for $A_{2\pi}$ is obtained with a precision of 1% and is uniquely linked to

the lifetime τ .

The first observation of $A_{2\pi}$ [31] has been achieved in the interaction of $70\,\mathrm{GeV/c}$ protons with Tantalum at the U-70 synchrotron of Serpukhov. In that experiment the atoms were produced in a few $\mu\mathrm{m}$ thick Ta target inserted into the internal proton beam. Using the statistics of only 270 ± 50 atomic pairs, it already was possible to set a lower limit on the $A_{2\pi}$ lifetime [32, 33]: $\tau>1.8\times10^{-15}~\mathrm{s}$ (90% CL).

In this work we present high statistics experimental data on $A_{2\pi}$ production on a Ni target at an external proton beam of the CERN PS and determine the resulting pionium breakup probability.

Chapter 2

Theory

2.1 Theoretical Motivation

Chiral symmetry allows to design the QCD Lagrangian describing quarks and gluon interactions. At low energies due to the running coupling constant α_s , QCD perturbation theory can not be used. But we can write at low energies an effective Lagrangian in terms of physical fields. For this effective Lagrangian, a perturbation theory, Chiral Perturbation Theory (ChPT), was developed using as expansion parameters the quark masses and the momentum. This works very well for $\pi\pi$ scattering because the expansion parameters, the momentum and the quark masses as compared to Λ_{QCD} are very small.

2.2 Scattering of $\pi^+\pi^- \to \pi^0\pi^0$

Charge exchange transforms an initial $\pi^+\pi^-$ -state into an $\pi^0\pi^0$ final state as shown in figure 2.1). This interaction conserves isospin, and the transition matrix element

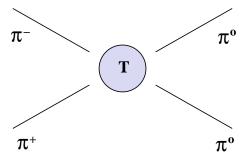


Figure 2.1: Schematic layout of the decay of a $\pi^+\pi^-$ pairs into a $\pi^0\pi^0$ pair. The transition matrix describing the interaction is denoted T.

 $<\pi^0\pi^0|T|\pi^\pm\pi^\mp>$ may be decomposed into the respective isospins. If we define the three pions as an isospin triplet,

$$\pi^+ = |11>$$
 (2.1)

$$\pi^0 = |10>$$
 (2.2)

$$\pi^{-} = |1 - 1\rangle \tag{2.3}$$

we can use the Clebsch-Gordan coefficient [34] to build the combined isospin states $|\pi^0\pi^0\rangle$ and $\pi^{\pm}\pi^{\mp}\rangle = |\pi^+\pi^-\rangle + |\pi^-\pi^+\rangle$:

$$|\pi^0 \pi^0\rangle = \sqrt{\frac{2}{3}} |20\rangle - \sqrt{\frac{1}{3}} |00\rangle$$
 (2.4)

$$|\pi^{+}\pi^{-}\rangle + |\pi^{-}\pi^{+}\rangle = \sqrt{2}(\sqrt{\frac{1}{6}}|20\rangle + \sqrt{\frac{1}{3}}|00\rangle)$$
 (2.5)

where $|20\rangle$ and $|00\rangle$ are the combined isospin states with isospin 2 and 0, respectively. The transition matrix elements in their respective isospin states can be written:

$$<\pi^0\pi^0|T|\pi^{\pm}\pi^{\mp}\rangle = (\sqrt{\frac{2}{3}} < 20|-\sqrt{\frac{1}{3}} < 00|) \cdot T \cdot$$
 (2.6)

$$\sqrt{2}\left(\sqrt{\frac{1}{6}}|20\rangle + \sqrt{\frac{1}{3}}|00\rangle\right) \tag{2.7}$$

$$= \sqrt{\frac{2}{9}} (\langle 20|T|20\rangle - \langle 00|T|00\rangle) \tag{2.8}$$

$$\propto T_{20} - T_{00}$$
 (2.9)

Hence the transition matrix is directly proportional to the difference of the $|20\rangle$ to $|20\rangle$ and $|00\rangle$ to $|00\rangle$ transition. In the limit of zero relative momentum Q, the imaginary part of the transition matrix elements T_{20} and T_{00} become zero [35] so that we can write the transition matrix elements as their real part only

$$Re(T_l^I(s)) = Q^{2l}(a_l^I + Q^2b_l^I + \mathcal{O}(Q^4))$$
 (2.10)

where l refers to the partial wave, I to the isospin number, and the a_l^I and the b_l^I are constants. The a_l^I are called the scattering lengths. We see that for l=0 and in the limit of zero relative momentum, the transition matrix elements T_{20} and T_{00} are uniquely defined by these (real) scattering lengths.

From equation 2.9 we see that the transition is directly proportional to the the difference of T_{20} and T_{00} . Combined with equation 2.10 we can conclude that for the case of Q=0 MeV/c the total scattering amplitude is proportional to the difference between the isoscalar and isotensor scattering length, $\Delta=|a_0^0-a_0^2|$.

We can calculate the scattering lengths in the framework of ChPT. Using chiral perturbation theory, we can expand the difference between the isoscalar and isotensor scattering length, $\Delta = |a_0^0 - a_0^2|$ in terms of the pion mass,

$$\Delta = \Delta_0 (1 + \Delta_2 m_\pi^2 + \Delta_4 m_\pi^4 + \dots) \tag{2.11}$$

The leading term Δ_0 was first calculated by Weinberg [36] to be

$$\Delta_0 = \frac{9m_\pi^2}{32\pi F_\pi^2} = 0.16 \tag{2.12}$$

Gasser and Leutwyler [37] evaluated Δ up to one-loop order. The most recent theoretical evaluation of the two $\pi\pi$ scattering lengths including next-to-next-to leading order from Colangelo et al [10] gives:

$$a_0^0 = 0.220 \pm 0.005 \tag{2.13}$$

$$a_0^2 = 0.0444 \pm 0.001 \tag{2.14}$$

$$\Delta = |a_0^0 - a_0^2| = 0.265 \pm 0.004 \tag{2.15}$$

2.3 Experimental results on a_0^0 and a_0^2

The value of a_0^0 was obtained from detailed investigation of the decay $K \to \pi^+\pi^-e^+\nu_e$. The most recent results of the E865 experiment [13] are the following. If both a_0^0 and a_0^2 are treated independently, then $a_0^0=0.203\pm0.033$ and $a_0^2=0.055\pm0.023$. Using Roy equations and a relation between a_0^0 and a_0^2 from the Chiral perturbation theory, the final results read:

$$a_0^0 = 0.216 \pm 0.013(stat) \pm 0.004(syst) \pm 0.002(theor)$$
 (2.16)

$$a_0^2 = 0.0454 \pm 0.031(stat) \pm 0.001(syst) \pm 0.0008(theor)$$
 (2.17)

2.4 Obtaining a_0^0 and a_0^2 from $A_{2\pi}$

The first clear experimental evidence for the existence of an atom consisting of two bound pions with opposite charge ($A_{2\pi}$ or pionium) was seen in a previous experiment[32]. The relation between the lifetime of pionium and a_0^0 and a_0^2 was first proposed by Uretsky [3]. Nemenov [15] determined the production cross section of the pionium atoms and determined the yield. He also investigated the properties of excited states.

DIRAC aims to see more than 20000 $A_{2\pi}$'s and measure its lifetime. This should yield an accurate value for the lifetime with an error of 10% , which translates into an error for Δ of the order of 5% .

2.4.1 $A_{2\pi}$ lifetime

 $A_{2\pi}$ main decay channel (99.6%) is strong into two π^0 's [38]:

$$\pi^+\pi^- \to \pi^0\pi^0$$
 (2.18)

The decay width of this channel can be written as:

$$\Gamma_{2\pi^0} = \frac{16\pi p^*}{9M_{\pi}^3} \cdot |a_0^0 - a_0^2|^2 \cdot \sum_n |\psi_{n,0}(0)|^2 = \sum_n \frac{2}{9} \frac{1}{n^3} \cdot \alpha^3 p^* \cdot |a_0^0 - a_0^2|^2 \quad (2.19)$$

where $p^* = \sqrt{M_\pi^2 - M_{\pi^0}^2 - 0.25 M_\pi^2 \alpha^2}$, α is the fine structure constant, n is the principal quantum number and $\psi_{n,0}(0)$ is the pure Coulomb wave function at zero distance between the two pions.

The lifetimes of higher n states τ_{n00} is connected to the ground state (1S) lifetime τ_{100} as:

$$\tau_{n00} = \tau_{100} \cdot n^3 \tag{2.20}$$

Corrections from strong interactions and vacuum polarization are small. The most recent connection between Δ and the pionium lifetime comes from Gasser et al.[7]:

$$\frac{1}{\tau} = \frac{2\alpha^3 p^*}{9} (\Delta + \epsilon)^2 (1 + K) \tag{2.21}$$

K= $(1.15\pm0.16)\cdot10^{-2}$ takes into account Coulomb corrections, $\epsilon=(0.61\pm0.16)\cdot10^{-2}$ isospin breaking effects.

Thus a measurement of τ with an accuracy of 10% will give a precision of 5% on Δ .

2.4.2 Lifetime predictions

Translating equation 2.21 into a lifetime, using recent estimates for the a's from Colangelo *et al.* yields [7, 10] as lifetime for the 1S state of:

$$\tau = (2.9 \pm 0.1) \cdot 10^{-15} [s] \tag{2.22}$$

The problem is that this lifetime is too small to be measured directly. However an indirect way to measure this quantity was proposed by DIRAC, which is explained in the following.

2.5 Production of pion pairs in high energy collisions

Let us consider an inelastic collision of the protons from the 24 GeV/c PS beam and the target atoms. With some probability a $\pi^+\pi^-$ pair will be produced. This

 $\pi^+\pi^-$ pair can have various origins: it can come from two different proton nucleus collision or it can come from the same one with or without Coulomb final state interaction (FSI). Depending on their origin, these pion pairs can be uncorrelated (accidentals), time correlated without Coulomb FSI (non-Coulomb) as well time correlated with Coulomb FSI (Coulomb and atomic pairs). Atomic pairs are $\pi^+\pi^-$ pairs which origin from the breakup of $A_{2\pi}$ due to interaction with target atoms. This section explains the production mechanism of these pion pairs in turn and relates some of them to each other.

2.5.1 Coulomb and atomic pairs

Pions that are produced close one to each other compared with the pionium Bohr Radius ($a_{\pi} = 387 \times 10^{-15} \ m$) exhibit Coulomb Final Interaction (FSI). We call such pion pairs **Coulomb pairs** in our notation. This stands in contrast to **non-Coulomb pairs**, pions produced from decays of long-lived resonances (e.g. η , K_S^0 and Λ) and created far away from the production point 1 , and hence from the other pion of the pair. The yield of non-Coulomb pairs is given by the double inclusive cross section

 $\frac{\mathrm{d}^2 \sigma_s^0}{\mathrm{d}\vec{p} \, \mathrm{d}\vec{q}}$

where \vec{p} and \vec{q} are the π^+ and π^- momenta in the laboratory system. The superscript 0 means that FSI has not been considered.

With a certain probability some of these pion pairs will bind one to each other by means of the Coulomb final state interaction (FSI) leading to pionium, the $\pi^+\pi^-$ bound system. The mathematical representation of pionium production is given by the cross section [15]:

$$\frac{\mathrm{d}\sigma_{nlm}^A}{\mathrm{d}\vec{P}} = (2\pi)^3 |\psi_{nlm}(0)|^2 \frac{E}{M} \lim_{\vec{O}\to 0} \left(\frac{\mathrm{d}^2 \sigma_s^0}{\mathrm{d}\vec{p} \,\mathrm{d}\vec{q}}\right). \tag{2.23}$$

where the effect of the final state Coulomb interaction is a bound state with quantum numbers n, l, and m as the squared wave function at the origin reflects. The production process for the atoms is shown in figure 2.2.

While traveling through the target, the atoms interact with the target nuclei and sometimes break up into atomic pairs, $\pi^+\pi^-$ pairs with Coulomb FSI interaction².

¹The range of Coulomb interaction between two pions is given by the Bohr radius of pionium, 387.5 fm. The mean free paths of relativistic η , K_S^0 and Λ are 1.7 Å, 2.2 cm and 7.89 cm. The η' is the only resonance with a mean free path of the same order as the Bohr radius, 786 fm. However, only 1% of π^- pions are created from its decay [40]. The production of pionic atoms from $\pi^+\pi^-$ pairs from the same decay is also posible but tiny [41].

²The breakup process is explained in more detail in the following section.

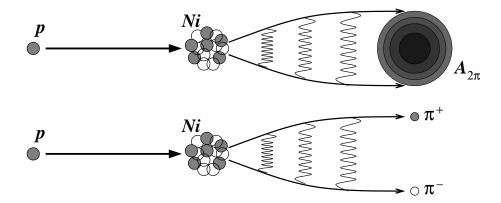


Figure 2.2: This figure shows the parallel production mechanism of atomic bound states (top) and free $\pi^+\pi^-$ Coulomb pairs (bottom).

Aside from atoms, the Coulomb FSI also leads to an enhancement of $\pi^+\pi^-$ double inclusive cross section for low relative momentum (Q) pairs from short lived sources (see also figure 2.2) [39]

$$A_C(Q) = \frac{2\pi M_\pi \alpha / Q}{1 - e^{-2\pi M_\pi \alpha / Q}},$$
 (2.24)

 $A_C(Q)$ has a pole at zero and tends to one for large Q. This means that low Q pairs are bent into even lower relative momentum while large relative momentum pairs are only slightly affected by the FSI. The Coulomb pairs production cross section can then be written as:

$$\frac{\mathrm{d}^2 \sigma_s}{\mathrm{d}\vec{P} \,\mathrm{d}\vec{Q}} \approx A_C(Q) \frac{E}{M} \lim_{Q \to 0} \left(\frac{\mathrm{d}^2 \sigma_s^0}{\mathrm{d}\vec{p} \,\mathrm{d}\vec{q}} \right). \tag{2.25}$$

which is the analogue of equation (2.23) for the production of not bound states. The analogy is complete if we notice that the Coulomb enhancement factor $A_{\mathcal{C}}(Q)$ can be written as

$$A_C(Q) = (2\pi)^3 \left| \psi_{\vec{Q}}^{(+)}(0) \right|^2$$
 (2.26)

where the $\psi_{\vec{Q}}^{(+)}(\vec{r})$ are a particular complete set of solutions of the continuum spectrum with the characteristic of asymptotically becoming an outgoing plane wave with \vec{Q} momentum. This set of solutions was obtained by A. Sommerfeld and this is why they are sometimes referred to as the Sommerfeld wave functions.

Dividing equations (2.23) and (2.25) we eliminate the laboratory momentum dependence and calculate the relative yield between Atoms and Coulomb pairs. Integrating (2.25) in a region of the phase space, Ω , the ratio between the number

-		raides a	10 111 111 0 1 / 01		
	Ω_1	K_Q	$\Omega_2(Q_T < 4.)$	K_{Q_l}	
	Q < 1.	2.493	$Q_l < 1.$	0.252	
	Q < 1.5	1.104	$Q_l < 1.5$	0.174	
	Q < 2.	0.615	$Q_l < 2$.	0.134	
	Q < 2.5	0.387	$Q_{l} < 2.5$	0.111	
	Q < 3.	0.263	$Q_l < 3$.	0.094	
	Q < 3.5	0.188	$Q_l < 3.5$	0.083	
	Q < 4.	0.140	$Q_l < 4$.	0.074	
	Q < 4.5	0.107	$Q_l < 4.5$	0.067	
	Q < 5	0.084	$O_1 < 5$	0.061	

Table 2.1: K factor value, according to equation (2.27) for two different choices of Ω . All relative momentum values are in MeV/c.

of created atoms (N^A) , created in any bound state, and the number of Coulomb pairs (N^{Coul}) holding $\vec{Q} \in \Omega$ is ³:

$$\text{k-factor} = \frac{N^A}{N^{Coul}(\vec{Q} \in \Omega)} = \frac{\sum_{nlm} \frac{d\sigma_{nlm}^A}{d\vec{P}}}{\int_{\vec{Q} \in \Omega} \frac{d\sigma_s^C}{d\vec{P}d\vec{Q}} d\vec{Q}} = \frac{(2\pi)^3 \sum_{nlm} |\psi_{nlm}(0)|^2}{\int_{\vec{Q} \in \Omega} A_C(Q) d\vec{Q}} \quad (2.27)$$

In Table 2.1 and Figure 2.3 we show the value of the K factor for two particular Ω choices, $\Omega_1 = \{\text{events with } Q < Q^0\}$ and $\Omega_2 = \{\text{events with } Q_T < 4 \ MeV/c \text{ and } Q_l < Q_l^0\}$.

Since the atomic pairs are predominantly produced below Q<2 MeV/c, we choose this particular Q value also for Ω , which makes us in first approximation independent on the efficiency and acceptance of the setup. Making this choice yields a theoretical k-factor of

$$k^{th} = \frac{N^A}{N^{Coul}(Q < 2\text{MeV/c})} = 0.615$$
 (2.28)

Source finite size corrections are calculated to the final state correlation. The results show that the Coulomb enhancement function $A_c(Q)$ should be multiplied by a corrective factor affecting only the Q<2 MeV/c region. The change is smaller than 2.5% [42]. Also the bound states wave function is changed at the

³The effect of the strong interaction between the two pions changes the Coulomb factor and the atomic wave function by the same multiplicative factor which is also suppressed when the ratio for the k-factor is calculated [43].

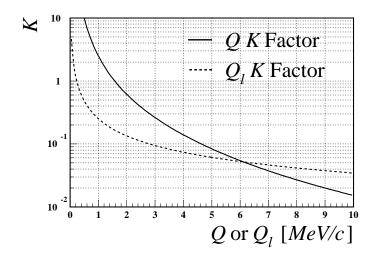


Figure 2.3: K factor value at the generation point. The Q_l value has a cut on $Q_T < 4MeV/c$.

same level. The simultaneous corrections of the Coulomb and atomic pairs tends to cancel the effect in the k-factor for very low Q's⁴.

2.5.2 Coulomb and Non Coulomb pairs

In addition to atomic and Coulomb correlated pairs also Non Coulomb $\pi^+\pi^-$ pairs are produced. These are time correlated pairs, and hence both pions come from the same proton-target interaction, where at least one of the pions is produced in the decay of a long lived particle. The production mechanism is schematically shown in Figure 2.4.

The total production of time correlated $\pi^+\pi^-$ pairs is given by the short lived and long lived sources. The proportion of pion pairs produced by long lived sources (ω_l) has been shown to depend only on P [44] for small Q, the magnitude of the total momentum of the pair. Hence we can write the production cross section for this type of pairs as:

$$\frac{\mathrm{d}^2 \sigma_l}{\mathrm{d}\vec{p} \mathrm{d}\vec{q}} = \omega_l(P) \frac{\mathrm{d}^2 \sigma}{\mathrm{d}\vec{p} \mathrm{d}\vec{q}}$$
 (2.29)

where $d^2\sigma/d\vec{p}d\vec{q}$ is the double differential inclusive total cross section (no matter whether short or long lived sources). It can be obtained after the acceptance

⁴There are also strong interaction effects which cancel as well for the calculation of the k-factor.

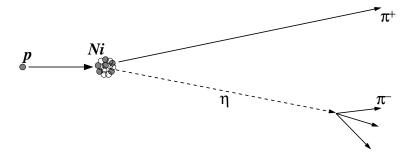


Figure 2.4: Production mechanism of non-Coulomb pairs.

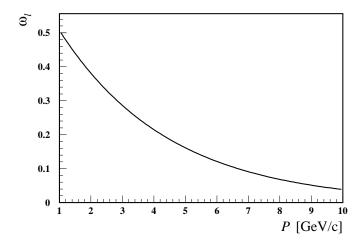


Figure 2.5: The ratio of pion pairs from long lived sources $(\omega_l(P))$ for a Nickel 94 μ m target.

cuts of DIRAC spectrometer from the experimental prompt events data. We have obtained $\omega_l(P)$ using pure FRITIOF6 Monte Carlo distributions [45].

Knowing $d^2\sigma/d\vec{p}d\vec{q}$ and $\omega_l(P)$ we can also obtain the double inclusive cross section from short-lived sources:

$$\frac{\mathrm{d}^2 \sigma_s}{\mathrm{d}\vec{p} \mathrm{d}\vec{q}} = (1 - \omega_l(P)) \frac{\mathrm{d}^2 \sigma}{\mathrm{d}\vec{p} \mathrm{d}\vec{q}}$$
 (2.30)

2.5.3 Accidental pairs

Most pions that are produced in the target are uncorrelated to each other. They origin from different proton nucleus interactions. Figure 2.6 shows as a diagram the production of such $\pi\pi$ pairs. Such pairs are called 'accidental' pairs or acci-

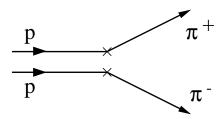


Figure 2.6: The production of uncorrelated $\pi^+\pi^-$ pairs in two 24 GeV/c proton nucleon interactions.

dentals. Since they come from two different interactions, we can write the cross section as

$$\frac{1}{\sigma_{inel}} \frac{d\sigma}{d\vec{p}_1} \frac{d\sigma}{d\vec{p}_2} \tag{2.31}$$

where $\frac{d\sigma}{d\vec{p_1}}$ is the single inclusive cross section.

2.6 Interaction of relativistic $A_{2\pi}$ with matter

2.6.1 Cross section with atoms

After production, the pionium atom is moving in the target interacting mostly with the electromagnetic field of the target atoms. The Coulomb interaction with the target atoms can be described in first approximation using the Born approximation, which considers only one photon exchange. This approach yields a relative accuracy on the cross section of less than 1% [46] for Nickel and increases with Z. More precise calculations are available using the Glauber approximation, which takes into account multi-photon exchange as well [22]. The most recent results comes from Heim *et al.* [27], calculating the cross section with an accuracy of 1%

2.6.2 $A_{2\pi}$ breakup probability

The evolution of the pionium population through the target has been described by Afanasyev and Tarasov [20]. The $A_{2\pi}$ atom in the target can either decay into two π^0 ,

$$A_{2\pi} \to \pi^0 + \pi^0$$
 (2.32)

get excited (de-exited) into higher (lower) states or get ionized (breakup) into a $\pi^+\pi^-$:

$$A_{2\pi} \to \pi^+ \pi^-$$
 (2.33)

Hence, the breakup probability can be calculated residually as:

$$P_{br} = 1 - P_{anh} - P_{dsc} (2.34)$$

where P_{br} is the breakup probability, P_{anh} is the annihilation probability and P_{dsc} is the probability that the atom leaves the target in a discrete state.

For practical reasons we apply a cut on the upper value of n. Equation 2.34 becomes then

$$P_{br} = 1 - P_{anh}(n < n_{cut}) - P_{anh}(n > n_{cut}) - P_{dsc}(n < n_{cut}) - P_{dsc}(n > n_{cut})$$
(2.35)

where n_{cut} is the highest state we consider in the calculations. The two probabilities for higher states can now be approximated. We can find an upper limit to be:

$$P_{anh}(n > n_{cut}) < 10^{-6} (2.36)$$

for $n_{cut} = 6$. This is very small compared to the annihilation probabilities of lower states and hence can be neglected.

The same logic can be applied to $P_{dsc}(n > n_{cut})$. The remaining higher states can be written as a sum which is estimated to be smaller than

$$P_{dsh}(n > n_{cut}) < 10^{-3} (2.37)$$

From experimental data we can obtain the breakup probability as

$$P_{br} = \frac{n_A}{N_A} \tag{2.38}$$

for $A_{2\pi}$ atoms (number of produced atoms N_A) breaking up into $\pi^+\pi^-$ pairs (number of broken up atoms n_A) as a function of the target nuclei charge, the target thickness and the atom lifetime.

2.6.3 Direct calculation of the break-up probability

The description of the pionium population evolution in the target leads to a system of coupled differential equations [20] which can be solved numerically or using Monte Carlo. C. Santamarina *et al.* [30] implemented a Monte Carlo simulation to determine the break-up probabilities for those states with low principal quantum number $n \le n_{cut}$. The result of the Monte Carlo study are shown in the following. The current precision of these calculations is of the order of 1% [30]. Figure 2.7

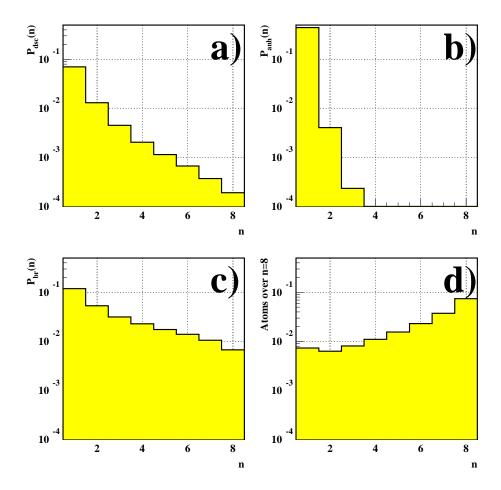


Figure 2.7: Discrete state (a), annihilation (b), break-up (c) and to-higher-state transition (d) probabilities as a function of the principal quantum number. Plot (a) illustrates the probability that an atoms leaves the target as a bound state, (b) describes the annihilation probability, (c) the break-up probability and panel (d) shows the probability for an atom to jump to a state with principal quantum number higher than n_{cut} . The calculations are based on a Nickel 94 μ m layer with 3 fs lifetime pionium atoms with 4.7 GeV/c momentum.

shows the probabilities as a function of the principal quantum number for 4.7 GeV/c monochromatic $A_{2\pi}$ atoms assuming 3 [fs] lifetime. Plot (a) shows the probability that the pionium atom leaves the target as a bound state (P_{dsc}) , plot (b) is the annihilation probability (P_{anh}) , (c) reflects the break-up probability (P_{br}) and finally panel (d) shows the probability that an atoms gets excited in a state

with $n > n_{cut}$. Also figure (a) illustrates the break-up probability as a function of the principal quantum number follows a power law and it can approximately be parametrized as:

$$P_{br}(n) \sim \frac{1}{n^{1.3}}$$
 (2.39)

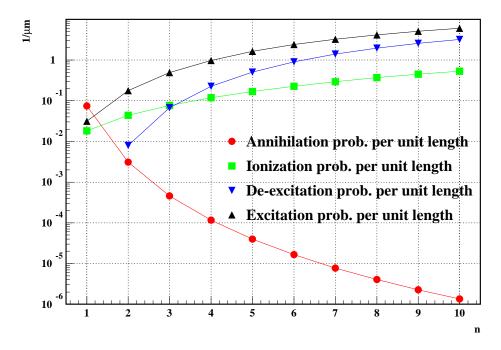


Figure 2.8: Annihilation, ionization, de-excitation and excitation probabilities per unit length as a function of the principal quantum number.

Figure 2.8 shows the same annihilation, ionization, de-excitation and excitation probabilities per unit length as a function of the principal quantum number in one (log) plot. It illustrates the relative importance of each process for the principal quantum numbers 1 to 10. If we compare the process of annihilation versus break-up we find the intuitive reasoning confirmed that for higher quantum number the break-up dominates the annihilation process due to a larger Bohr radius. Only for n=1 principal quantum number the annihilation process dominates.

The knowledge of the different probabilities further allows to calculate the integrated break-up probability of the atoms as a function of the position of the atom in the target as figure 2.9 demonstrates. The calculation was performed assuming a 94 μ m Nickel layer for monochromatic 4.7 GeV/c momentum pionium atoms.

21

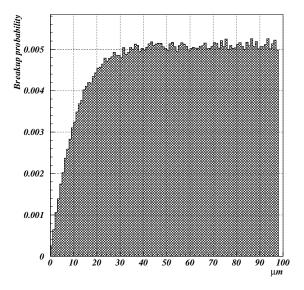


Figure 2.9: Break-up probability of $A_{2\pi}$ atoms as a function of the atom breakup position in the target. The used target is a 94 μ m Nickel layer for monochromatic 4.7 GeV/c momentum pionium atoms.

2.6.4 Lifetime dependence of the break-up probability

In addition one can calculate the breakup probability for various targets. To make the signal and background shape for different targets comparable, the target size per radiation length, $\frac{S}{X_0}$, where S is the target thickness and X_0 the radiation length has to be chosen to be the same for all targets. Figure 2.10 shows the breakup probability for various targets as a function of the atom lifetime.

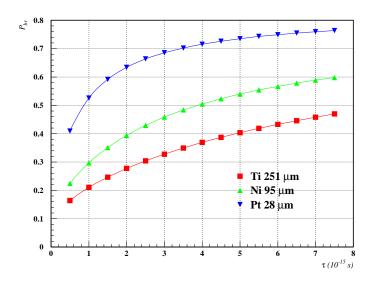


Figure 2.10: Breakup probability as a function of the atom lifetime for different target materials.

Chapter 3

DIRAC apparatus

The experimental setup is designed to measure $\pi^+\pi^-$ pairs and to select 'atomic pairs' with low relative momentum. After a calibration run at the end of 1998 DIRAC has been collecting data since summer 1999. A description of the DIRAC spectrometer is published [48].

3.1 General apparatus layout description

The DIRAC experiment is located at the T8 proton beam line of 24 GeV/c momentum in the East Hall of the PS accelerator at CERN. Figure 3.1 shows the CERN East Hall with the DIRAC experimental setup. The DIRAC apparatus consists of a target station, the secondary vacuum channel, a spectrometer magnet and detectors which are placed upstream and downstream of the magnet. In order to avoid background in the detectors, the secondary particle channel is arranged at an angle of 5.7° upwards with respect to the proton beam. A top view of the experimental setup with the indications of the various detectors can be seen in figure 3.2 while figure 3.3 shows the setup from the side. The upstream section of the secondary particle channel consists of the following detectors: Micro Strip Gas Chamber (MSGC), Scintillating Fiber Detectors (SFD) and Scintillating Ionization Hodoscopes (IH). Downstream of the analyzing magnet the setup splits into two identical arms for the detection and identification of positive and negative particles respectively. The angle between the arms of the spectrometer amounts to $2 \times 19^{\circ}$. Along each arm there are Drift Chambers (DC), Vertical Hodoscopes (VH), Horizontal Hodoscopes (HH), gas Cerenkov counters (C), a preshower detector (PrSh) and Muon counters (Mu).

Table 3.1 summarizes the material thicknesses (in units of radiation length $\cdot 10^{-4}$) encountered by secondary particles before they reach the DC system where their momenta are measured.

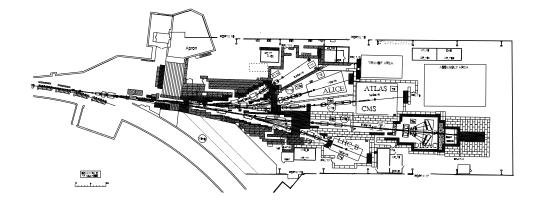


Figure 3.1: East Hall general view.

3.2 Proton beam and target station

The protons are extracted from the PS using a slow ejection mode in spills of around 450ms duration. During data taking DIRAC was assigned between 1 and 5 cycles per PS super-cycle (14-19 s). The intensity can be varied from $0.5 \ 10^{11}$ to $3 \ 10^{11}$ protons per spill. For the Nickel layer data taking in 2001 a beam intensity of about $1 \ 10^{11}$ was delivered. The beam dimensions in the vertical and horizontal planes are 1.6 mm and 3.2 mm respectively at 2σ . After the target station the proton beam continues under the secondary channel in a vacuum tube and is finally absorbed by the beam dump.

The target station harbors a device with 12 holders for targets, which can remotely be changed. The Nickel 2001 layer has a size of 10mm by 10 mm and a thickness of 94 μ m.

The DIRAC setup is sensitive to backscattering particles. This is due to the fact that the target is very thin and that the upstream detectors are placed closely to the target itself (around 20 cm from the beam). Nevertheless the halo is suppressed by special shielding and the detector's counting rates are 25 times higher with a target in place than without one.

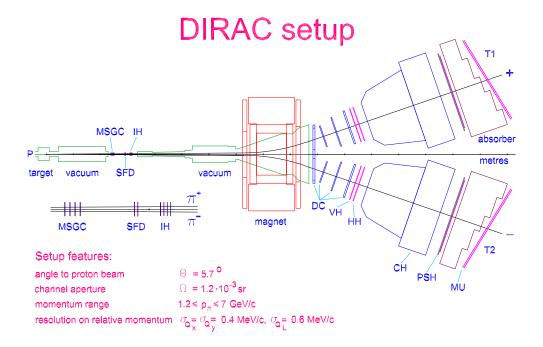


Figure 3.2: Experimental setup of the DIRAC experiment: P-proton beam, MSGC-micro strip gas chamber, SFD-scintillation fiber detector, IH-ionization hodoscope, DC-drift chamber, VH-vertical hodoscope, HH-horizontal hodoscope, Ch-Cerenkov detectors, PSh-preshower scintillation detector, Mu-muon counter.

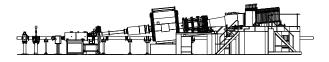


Figure 3.3: Side view of the DIRAC apparatus. The secondary particle channel is inclined by 5.7° with respect to the proton beam.

Table 3.1: Material contributions along the secondary particle channel in units of radiation length $\cdot 10^{-4}$.

Ni-target	33.5
Mylar window	8.7
4 planes MSGC	224.1
2 planes SFD	173.3
4 planes IH	153.1
Air gap	34.7
Mylar window	8.7
Al-window	76.4
Total	679.0

3.3 MSGC

The micro strip gas chamber (MSGC) is placed just downstream of the target. It consist of 4 consecutive chambers, each covering an active area of $10.24 \times 10.24 \text{ cm}^2$. Each chamber consists of a drift electrode, a GEM foil and a MSGC sensor. The GEM foil is evenly spaced between the two other layers as indicated in figure 3.4. The drift electrode is made of a Chromium-coated thin glass (200 μ m). The GEM is a 50 μ m thick kapton foil copper-cladded on both sides with a 4 μ m thick Cu layer. The etching pattern is characterized by 50μ m wide holes, 140 μ m apart. Application of a potential difference of 400 V between the two metal layers ($V_1 = -1600V$, $V_2 = -2000$ V) produces electron amplification by a factor of 30 [48].

The MSGC sensor consists of 200μ m pitch alternating chromium strips, with 9μ m and 100μ m anode and cathode width, respectively. Applied voltages are: -410V on cathodes and -3000V on the drift electrode, whereas anode strips are set to ground. The gas employed is a mixture of Ar-DME($\frac{60}{40}$). Under these conservative conditions an overall detector gain of approximately 3000 is achieved.

The read out of the MSGC supplies the user with an ADC value of the deposited energy.

Adjacent hit strips are recognized as clusters. Figure 3.5 shows the number of hit strips per cluster (a) and the cluster multiplicity per plane (b). Single track resolution was measured in a dedicated run in 2000 by setting all four planes parallel to each other yielding a typical single track resolution of $54\mu m$ [48]. Double track resolution for close-lying hits suffers from the ambiguity of the clustering due to high multiplicity of hit strips per cluster (figure 3.5 a) and is of the order of 500 to 700 μm [49]. The average distance between the two pions originating from $A_{2\pi}$

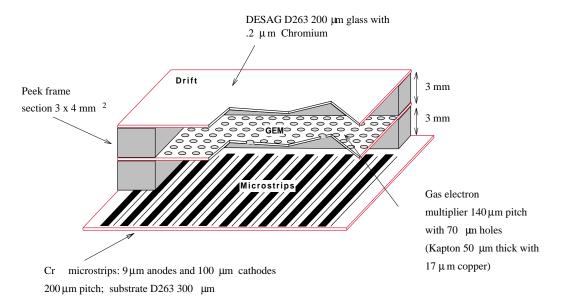


Figure 3.4: Layout of the MSGC detector.

at the level of MSGC is also of the order of 500 μm .

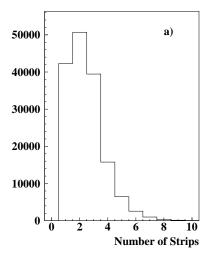
The MSGC are operational since 2001 with an 'off-time' of typically 40% in 2001. The efficiency per plane was measured to be around 93% which yields an efficiency requiring 4 planes of 0.74.

3.4 Scintillation Fiber Detector

The scintillation fiber detector (SFD) is used for tracking and triggering. It consists of 2 perpendicular planes (X and Y) separated by 2.5 cm. Each plane is made of 240 channels. Since 2002 a third inclined U plane with 340 channels was added. The U plane is rotated with respect to the X axis by an angle of 45° . The SFD fibers have a diameter of 500 μ m. This leads to an active area of 10.5×10.5 cm².

The SFD X and Y layers consist each of five layers of KURARAY fibers forming one sensitive column which is mapped to one channel of a position sensitive photomultiplier (PSPM). Figure 3.6 illustrates the detector layout. The fiber column pitch is 440 μ m which defines the single track resolution. Each column is connected to a light guide of about 300 mm length which is glued into one channel of the PSPM. In total there are 16 channels per PSPM and 15 PSPM to yield the 240 channels per SFD plane. The level of optical cross-talk among the PSPM channels was measured to be of the order of 1% [48].

28



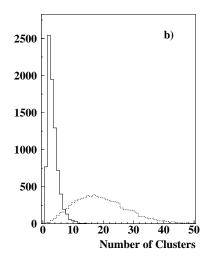


Figure 3.5: a) GEM/MSGC strip multiplicity per hit-cluster b) cluster multiplicity per event in one plane (X). The dotted line shows all clusters registered by the data acquisition, whereas the continuous line shows only those having a time tag, established when the cluster has a corresponding hit in the SFD aligned with the interaction point

3.4.1 Readout electronics and the PSC circuit

The readout electronic harbors a dedicated peak sensing circuit (PSC) which provides signal discrimination and rejection of cross-talk from adjacent channels. An accurate description of the peak sensing circuit can be found in the paper of Gorin et al [50]. In short the PSC discriminates signals according to the condition

$$2A_i - A_{i-1} - A_{i+1} > A_{thres}$$

where A_i are the channel signal amplitudes and A_{thres} denotes the threshold value. For time correlated (up to 5 ns time difference) double track events which are separated by more than one fiber pitch the PSC successfully eliminates unwanted cross-talk. However, if two adjacent fibers are crossed by two particles simultaneously, the PSC algorithm suppresses one hit with around 50% probability. In such cases the signature from a double track event can not be distinguished from a single track event using the SFD detector alone. The distinction between single track events and close-lying double track events can partly be remedied using the ionisation hodoscope signals, since double track events deposit on average more energy in the IH than single track events. For events with a relative time difference greater than 5ns the PSC behaves as an ordinary discriminator. The inefficiencies due to the PSC and the PSC time-correlation were studied independently by D.

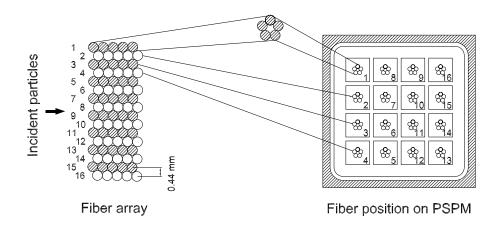


Figure 3.6: The SFD structure. A 16-channel fragment is shown.

Goldin[51] and F. Takeutchi[52]. For particle pairs with relative time differences greater than 5 ns, the PSC behaves as an ordinary leading edge discriminator.

The read out supplies time information in digital form (TDC values).

3.4.2 Performance

The SFD performance is influenced by the high flux of particles due to the position of the detector close to the target and by particles which are scattered toward the detector. Nevertheless the detection efficiency is sufficiently high. D. Goldin and L. Tauscher [51] estimated the single track inefficiencies for the 2001 run to be 5%. For double ionization events with 2 track requirement the efficiency of detecting one or two hits with the active area of the SFD is 91% with no track constraints and 95% with the track constraint. The cross-talk (i.e. double hits in SFD with the singly ionized slab in the IH) is observed in 2.2% of the events (with the track requirement on).

The time resolution per SFD is found to be around 0.8 ns [48] which translates into a relative time resolution between the two planes of about 1.2 ns, in agreement with Goldin and Tauscher [51]. Figure 3.7 shows the time difference between the two SFD planes for reconstructed single track events which also exhibits a relative time resolution of 1.2 ns.

The space resolution for single track events using SFD alone is given by the typical fiber pitch size of 440 μ m. Double track resolution is distorted for closelying tracks due to the PSC.

The multiplicities per plane are shown in figure 3.8. The average hit multiplicities within the trigger window are 3.9 (X) and 4.1 (Y). The average hit multiplicities for time and space correlated hit candidates from the tracking are 2.7 for X

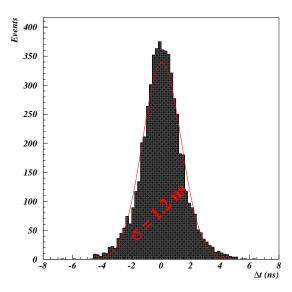


Figure 3.7: Time difference between the two SFD planes for reconstructed single track events.

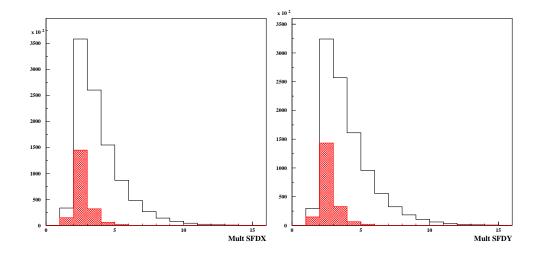


Figure 3.8: Multiplicities of the SFD X (left) and Y (right) plane. The black distribution illustrates all hits within the trigger window, while the red distribution shows time and space correlated hit candidates from the tracking. The two distributions come from different samples.

and Y.

3.5 Ionization Hodoscopes

From the discussion of the PSC algorithm of the SFD detector it is clear that closelying tracks create an ambiguity for the tracking. One possible way to remedy this situation is to measure the ionization energy loss. A dedicated ionization hodoscopes (IH) has been built to separate single tracks from close-lying double tracks by means of their ionization energy loss.

The ionization hodoscopes IH consists of two X and two Y planes with a sensitive area of 11×11 cm². Each plane harbors 16 plastic scintillator strips. One strip has a width of 7 mm, a length of 11 cm and a thickness of 1 mm. They are connected to the PM photo cathodes via 2 mm thick and 7 mm wide lucite light guide. Figure 3.9 shows an isometric view of the IH detector.

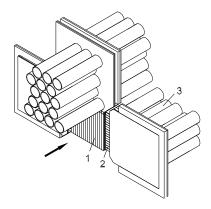


Figure 3.9: Isometric view of the Ionisation Hodoscopes. 1 – scintillators, 2 – light-guides, 3 – photo multipliers with shielding.

The ADC and TDC signals of the IH are read out and are available for the off-line analysis. The ADC spectra for single and double ionization events are shown in figure 3.10. If a threshold is set to retain 95% of the double ionisation signal from pairs, the contamination from single particle amplitudes is less than 15% (Fig. 3.11).

The time resolution per IH plane can be seen from figure 3.12, which shows the time difference between the VH and the first X plane of IH to be around 1 ns. Because the intrinsic time resolution of the VH is around 130 PS (see section VH), the plotted time difference is largely dominated by the intrinsic IH time resolution.

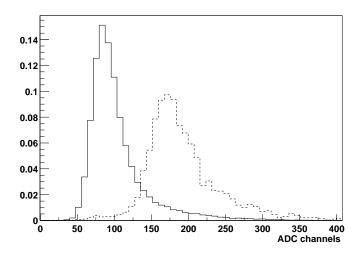


Figure 3.10: Typical ADC spectra for single (solid line) and double (dashed line) ionization loss from particles crossing one IH scintillating slab.

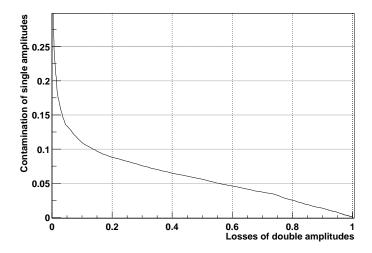


Figure 3.11: Contamination of single ionization amplitudes as a function of losses of double ionization as obtained from the analysis of the spectra of Fig. 3.10.

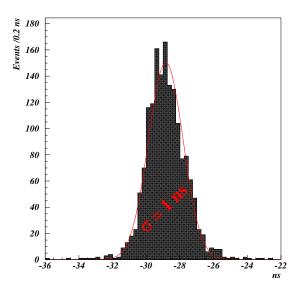


Figure 3.12: Time difference between VH and first X plane of IH. The time resolution is of the order of 1 ns.

3.6 Magnet

The spectrometer dipole magnet splits the positive and negative particles with its magnetic field of 1.65 Tesla (BL = 2.2 Tm) into two separated arms downstream. The two arms are placed at $\pm 19^{\circ}$ relative to the central axis. The magnetic field has been measured and parametrized [53].

3.7 Drift Chambers

The drift chamber system is used to perform the particle tracking downstream the magnet. The drift chamber system is capable to handle high rates reaching up to 10 kHz/cm^2 .

The drift chamber for each arm are separate except for the first drift chamber set which is one single large module (DC-1) with two separated sensitive areas of 0.8 x 0.4 m² each. This chamber provides 6 successive measurements per particle of the coordinates X,Y,W,X,Y,W, where W denotes a measurement with an angle of 11.3° with respect to the X-coordinate. The DC-1 incorporates 800 channels.

Both arms are further equipped with 3 identical chambers performing the measurements X,Y (DC-2), X,Y (DC-3) and X,Y,X,Y (DC-4). Their sensitive area is $0.8 \times 0.4 \text{ m}^2$ (DC-2 and DC-4) and $1.12 \times 0.4 \text{ m}^2$ (DC-3). Both arms together are instrumented with 1216 channels. The characteristics of the drift chamber system are summarized in Table 3.2.

Table 3.2. General properties of the De modules.				
Module	Sensitive	Measured	Number of	
type	area, cm^2	coordinate	planes	
DC-1	80×40	X	2	
	left arm	Y	2	
		W	2	
	80×40	X	2	
	right arm	Y	2	
		W	2	
DC-2	80×40	X	1	
		Y	1	
DC-3	112×40	X	1	
		Y	1	
DC-4	128×40	X	2	
		Y	2	

Table 3.2: General properties of the DC modules.

A schematic drawing of the sensitive element is shown in Fig. 3.13. The anode wires pitch is 10 mm, the distance L between the anode and cathode planes is 5 mm. The cathode planes and potential wires are at equal voltages. The sensitive area, corresponding to an anode wire and limited by the cathode planes and potential wires, has a square $(10 \times 10 \text{ mm}^2)$ shape. With a suitable gas mixture, it is possible to achieve an almost linear behavior of the drift function, except in a small region near the anode wire.

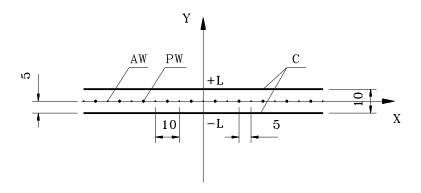


Figure 3.13: Schematic view of the wire chamber electrodes: AW – anode wires, PW – potential wires, C – cathode foils. Dimensions are in mm.

Cathode planes are made of $20~\mu m$ thick carbon-coated mylar foils with a surface resistivity of about $400~\Omega$ per square. Such cathode foils provide stable chamber operation due to a high work function of the carbon coating and, being thin, add only a small amount of material along the particle path.

Anode and potential wires of $50~\mu m$ and $100~\mu m$ diameter, respectively, are made of a copper-beryllium alloy. The rather large diameter of the anode wires has been chosen in order to operate the chambers at high current avalanche amplification mode.

The chamber design of the second drift chamber (DC-2) is shown in figure 3.14.

The module is constructed using stacks of aluminum and fiberglass frames, each of 5 mm thickness, fixed by screws. The fiberglass frames are the supports for the chamber electrodes (anode and potential wires and cathode foils). The two outer aluminum frames in the stack are used to fix the mylar window, and the inner ones are the spacers between the fiberglass frames. Rigidity of the module is enforced by aluminum rectangular tubes screwed to the surface of the frame package. The DC-1 drift chamber set differs from the others by means of its construction with two independent sensitive areas. The middle zone which is exposed to heavily radiating particles is insensitive to the particle flux.

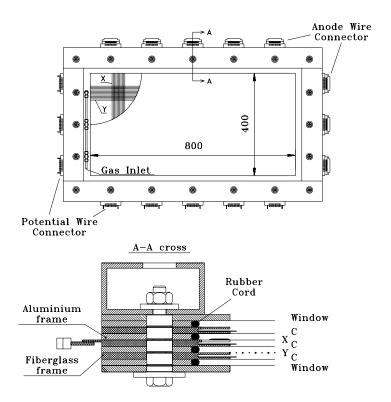


Figure 3.14: Design of the DC-2 module. Upper figure: general view. Lower figure: structure of the frame stack; X - X-plane, Y - Y-plane, C – cathode foils.

The chambers are operated in a high current avalanche mode which is characterized by high pulse amplitudes, small pulse width and stable operation. The single track efficiency for a particle flux of about 10kHz/cm^2 is higher than 96%. The gas used consists of Ar $(50\%)+iC_4H_{10}(50\%)+H_2O(0.5\%)$. The space to time relation was extracted from the time spectrum and its integral distribution, which are shown in figure 3.15 for a sample of clean events with a small background contribution, which demonstrates the proportional operation mode.

The resulting coordinate resolution of the DC system is measured to be around 100μ m as can be seen from figure 3.16. The measured space resolution of 100μ m also takes into account the uncertainty due to the track predictions so that the space resolution of the chamber alone is considered to be better than 90μ m. The track efficiency of the DC system as a whole is about 99%, which is due to the redundancy of the measurement.

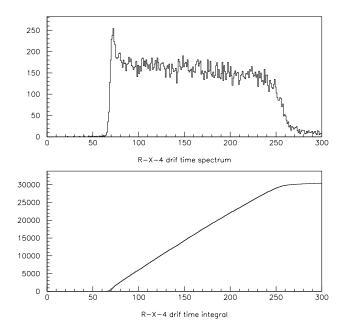


Figure 3.15: Distribution of the drift time (upper) and its integral spectrum (lower) for the X4-plane. Horizontal scale is in TDC channels, bin width is $0.5 \ ns$.

3.8 Vertical Hodoscopes

The vertical hodoscopes (VH) are built as an array of 18 vertical scintillating slabs per arm placed downstream the DC system. The VH system is used for coincidence between the two arms. It is used in the first level trigger to define a trigger time window of 40 ns per event and in the DNA trigger to select good events. It is further crucial to the detection of pion pairs that originate from the same proton interaction (prompt events). The VH has been specially designed to achieve a very good time resolution. The slabs are placed behind the DC system and matches its acceptance. The scintillating material used for the slabs is BICRON BC420. The slab dimensions are 40cm length, 7cm width and 2.2cm thickness.

The light from the scintillators is collected at each slab end by photo multipliers. The voltage dividers used are capable to operate in a high particle rate environment of up to 2 MHz, without any degradation of the time resolution. The front-end electronics uses LeCroy L3420 constant fraction discriminators, followed by CAEN C561 meantimers to provide a position independent time measurement.

The VH single-hit detection efficiency was estimated to be 99.5% for the positive and 98.8% for the negative arm.

The time resolution can be estimated using electron pairs from γ conversion

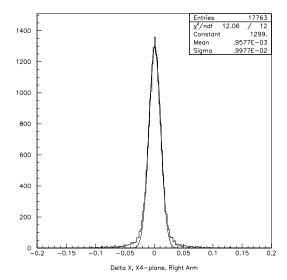


Figure 3.16: Distribution of differences between the measured and predicted X-coordinate for one drift chamber plane (X4).

or Dalitz decays of π^0 , which are almost synchronous in time, because the time-of-flight of the electrons is momentum independent in the available momenta acceptance. Figure 3.17 shows the time difference in the vertical hodoscopes for these time-correlated electron pairs after path length corrections. The fitted Gauss function reveals a relative time resolution of around 180ps. The intrinsic absolute time resolution per slab is therefore of the order of 120 ps [54].

The time difference for pion flagged events is shown in figure 3.18. The time-correlated prompt peak exhibits a signal over background ratio of about 14. The fitted Gauss function to the peak yields a σ of 190 ps. Figure 3.18 also gives rise to the definition of time-correlated (prompt) events in the peak and time-uncorrelated (accidental) events outside the peak.

The VH can also be used as a time-of-flight detector to suppress background $p\pi^-$ pairs for prompt events. Figure 3.19 shows the time difference in the VH versus the momentum of the positive particle. The vertical band results from time-correlated $\pi^-\pi^+$ pairs, while the curved band originates from π^-p and π^-K^+ pairs. Hence this timing capability allows to suppress proton contamination in the momentum range from 1 to 5 GeV/c and Kaon contamination in the momentum range from 1 to 2.5 GeV/c.

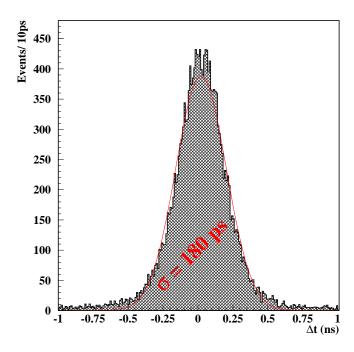


Figure 3.17: Time difference of the two arms for prompt electron pairs measured in 2001. The standard deviation of the fitted Gauss function is 180ps.

3.9 Horizontal Hodoscopes

The horizontal hodoscopes system (HH) is built as the VH ones as an array of 16 independent slabs per arm covering a region of $130 \times 40 \, \mathrm{cm^2}$. A positive answer is required from HH for each arm for the first level trigger. Furthermore its response is used to select events with small relative opening angle in the y direction.

The HH system in each arm constitutes of 16 horizontal scintillating slabs with the dimensions $130 \times 2.5 \text{ cm}^2$, with a thickness of 2.5cm. The slabs are made of BICRON BC420 scintillating material, its ends are connected to Philips XP 2008 photo multipliers which are equipped with voltage dividers to allow high counting rate capability.

The single-hit detection efficiency of the HH is estimated to be greater than 96.6% for both arms. The time resolution of the time difference for pion tagged events is around 440 ps as shown in figure 3.20 which translates into an absolute intrinsic time resolution per slab of around 320 ps [54].

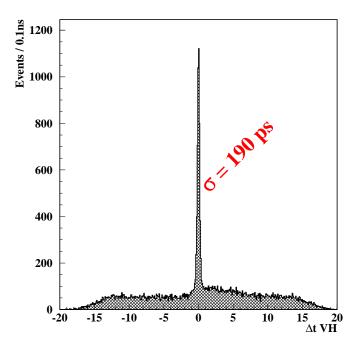


Figure 3.18: Time difference of the two arms for pion pairs for 2001. The standard deviation of the fitted Gauss function for the prompt signal is 190ps. The signal over background ratio for the prompt peak is 14. A cut on the absolute momenta in the positive arm was applied to suppress protons.

3.10 Cerenkov Counters

The Cerenkov counters (C) are gas detectors, used to reject electron-positron pairs from photon conversion and Dalitz decays and are therefore essential to suppress a major source of background. The response from the Cerenkov counters is used in the first level $\pi^-\pi^+$ trigger and in the calibration e^-e^+ trigger.

The DIRAC setup incorporates two identical Cerenkov counters, each covering one arm. The gas mixture used is $\rm N_2$ at normal temperature and pressure. The counters have a length of 285 cm.

Each counter is equipped with 20 mirrors and 10 photo multipliers on two rows. The light from two mirrors is collected by one photomultiplier. The analog signal of each photomultiplier is fed into two custom-made summing modules, one per counter (10 channels input). The output of the summing module is a linear sum of the input signals. The output is further attenuated by a factor of 3 with respect to individual channels. The sum output is fed into the trigger subsystem,

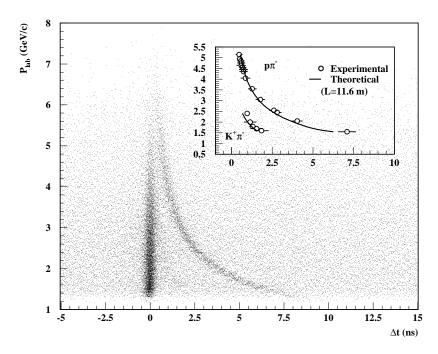


Figure 3.19: Correlation between the measured momentum of the positive particle and the VH time difference between the positive and negative spectrometer arm, taking into account the correction for the difference in path length. The accumulation bands correspond to $\pi^-\pi^+$ (vertical band) and π^-p (curved band) pairs. A small cluster of π^-K^+ pairs is also visible in the intermediate region.

while for offline analysis the sum and the individual counters are available.

The installed Cerenkov counters are used to tag electrons. Figure 3.21 shows the ADC spectrum from one Cerenkov counter. We can see that the ADC spectrum from pions peaks around ADC channel 30, while the one from one single electron has its peak already at ADC channel 40. Figure 3.22 shows the number of photoelectrons detected by one counter for (a) the positive and (b) the negative Cerenkov detector arm. The mean values are $N_{pe}=16.2$ and 16.4, respectively. From these values we infer that both counters have an efficiency greater than 99.8% when operated at a threshold slightly less than 2 photoelectrons [48].

In the offline analysis the pions are separated from the electrons by a cut on the summed ADC spectrum of 75 channels for the right arm and 62 channels for the left one.

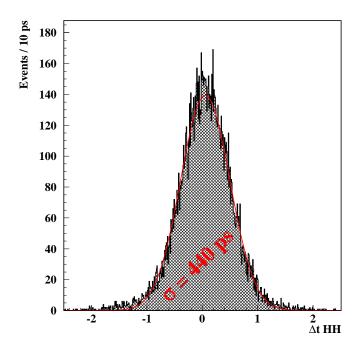


Figure 3.20: Time difference of the two arms for tagged pion pairs for 2001. The σ of the fitted Gauss function for the prompt signal is 440 ps.

3.11 Preshower

The preshower detector (Psh) is used to further eliminate background from electrons that are not recognized by the Cerenkov detector. Its response is also used in the trigger T1 decision.

The detector concept of the preshower is based on an array of lead converters followed by scintillators. A detector scheme is shown in figure 3.23. The Psh is built as an array of 8 elements per arm. Each element has a Pb converter and a scintillation counter. The converters of the two outermost elements are 10mm thick while the others are 25mm thick, which corresponds to 2 and 5 units of radiation length, respectively. The scintillating material used is BICRON type BC-408. Each element is 35 cm wide, 75 cm long and 1 cm thick. The scintillators are connected to photo multipliers, placed at the upper end only, see figure 3.23.

Electrons (positrons) can be separated from pions using the ADC information of the Psh detector. Electrons which pass through the lead converter shower electromagnetically while pions behave mainly as minimum ionizing particles. The resulting energy loss distribution as measured by the scintillators is shown in fig-

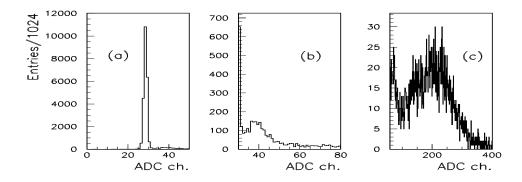


Figure 3.21: ADC spectrum from one Cerenkov photomultiplier: (a) spectrum from pions (practically equal to the ADC pedestal distribution), (b) amplitude signal from single photo electron, (c) spectrum from electrons.

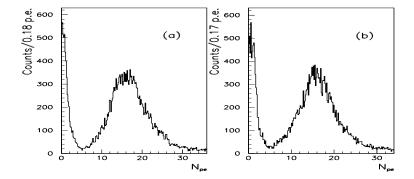


Figure 3.22: Distribution of the number of photoelectrons detected from the (a) positive and (b) negative Cerenkov detector arms.

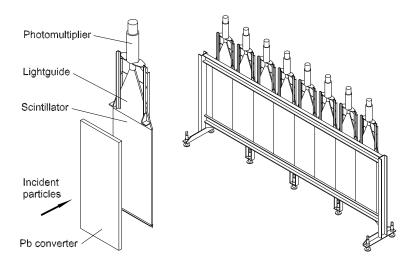


Figure 3.23: Preshower detector concept for one element and one spectrometer arm.

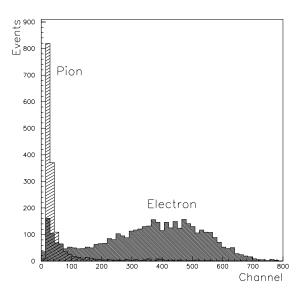


Figure 3.24: Pulse-height spectra for pions and electrons in one element of PSH.

ure 3.24. The tail of the pion spectrum is due to nuclear interactions of the pions with the converter material. From this figure one can define a cut on the ADC amplitude to further suppress electrons. For the offline analysis we use a cut at channel 80 that keeps 95% of the pions while simultaneously rejecting 85% of the

electrons. Most of the electrons in the pion region are detected by the Cerenkov counters.

The single arm detector efficiency for both arms is estimated to be 99.5%.

3.12 Muon Counters

The Muon counters (Mu) are designed to suppress background from muons. Most muons originate from pion decays with a small admixture of other decays and direct $\mu^+\mu^-$ pair production.

The muon detector is built using scintillation counters which are placed behind a thick iron absorber which almost entirely absorbs hadrons and related hadron showers. The Muon counters are installed symmetrically as two layers of 28 elements per arm. They are placed at the downstream end of the DIRAC apparatus, few meters away of the intense primary proton beam dump.

The iron absorber blocks have a thickness ranging from 60 to 140 cm. The thickness is larger in the region close to the spectrometer symmetry axis in order to compensate for the higher particle momenta. The counter itself is built as a double layer structure, each layer consisting of 28 counters with equal scintillating slabs of $75 \times 12 \text{cm}^2$ front area and 0.5cm thickness. The registered data is read out only if there is a response in both layers. The scintillation light is guided to photo multipliers at one end of the counter. Signals from both layers are fed into a constant fraction discriminator followed by a meantimer to generate an output signal only if both layers are hit by the same particle. Figure 3.25 shows the layout of the muon counters for one arm.

The time resolution of the muon counter is around 1.3 ns. Figure 3.26 shows the time difference between the time at the level of VH and the time measured at the muon counters.

The suppression of muon events is done offline by applying a time cut between VH and the Muon counters. The fraction of events which contain at least one muon was estimated at around 10% [55]. Such muon-like events originate mainly from pion decays on their way between the DC and the muon counter system. Decays upstream are heavily suppressed by the trigger system.

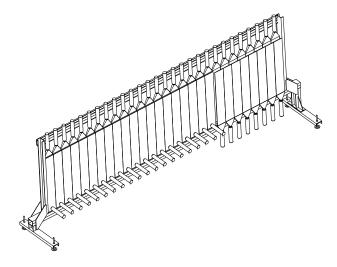


Figure 3.25: Schematic layout of muon counters on their support structure, indicating light guides and photo multipliers.

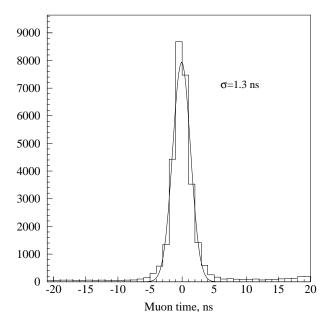


Figure 3.26: Time difference between the signals of the muon detector and the vertical hodoscopes.

Chapter 4

DIRAC Trigger

In order to operate with a high rate while at the same time being able to use precise tracking devices, the DIRAC experiment has a very sophisticated multilevel trigger scheme. In addition to a very fast first level trigger, there are two higher level trigger. The DIRAC multilevel trigger scheme is described in detail in [56, 48]. The trigger performance was studied in detail by S. Vlachos [57].

Due to the very specific data analysis procedure the DIRAC trigger scheme has to select not only time correlated events – such as pion pairs originating from $A_{2\pi}$ – but also uncorrelated $\pi^+\pi^-$ pairs. The optimal ratio of time-correlated to time-uncorrelated events is achieved by using a time window of coincidence of ± 20 ns between tracks in the positive and the negative arm. Specifically the time coincidence is obtained using the vertical hodoscopes.

4.1 General Trigger Scheme

The general trigger scheme is shown in figure 4.1. The pretrigger (T0) starts the neural network trigger (DNA). The first level trigger T1 starts digitization of the detector signals in the data acquisition modules (ADC, TDC). The drift chamber trigger processor (T4) starts with a positive decision from the first level trigger (T1). A positive decision of DNA in coincidence with a positive decision of T1 is used again in coincidence with the decision of T4. If the result is positive the readout of all detectors starts. If not, the buffers are cleared. The reason for this two stage process is to reduce dead-time due to a long readout time requirement of the MSGCs. So after a fast decision of DNA the Micro Strip Gas Chambers are readout.

In addition to the main trigger aimed at detecting pionium atoms, there are also several specialized calibration triggers which can be run in parallel or used separately. When the specialized calibration triggers are running in parallel with

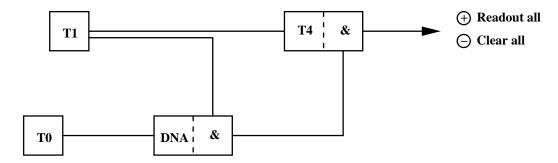


Figure 4.1: General block diagram of the DIRAC 2001 multilevel trigger.

the main trigger, appropriate prescaling factors are used. All trigger level besides T1 (and T0) can be run in transparent mode.

4.2 Pretrigger T0

The DNA trigger needs a fast initial signal which a simple early pretrigger is used to provide. To is defined as a coincidence of hit slab in VH1, VH2 PS1 and PS2. The coincidence time window is chosen as for the T1 trigger to be \pm 20 ns.

4.3 First Level Trigger T1

The first level trigger (T1) is used as a fast trigger to make a coincidence between crucially needed detectors. Specifically it performs the following tasks:

- Select events with response from both arms
- Classify the particles in electrons and pions. Kaons, protons and muons are also flagged as pions, but can be rejected in the off-line analysis using the time of flight information and a dedicated muon counter detector.
- Establish a coincidence between the two arms in a window of 40 ns. For the coincidence time the vertical hodoscopes are used.
- Applies a cut on the vertical opening angle (Coplanarity cut) for pion pairs.
 The cut requires that the difference of hit slab of the horizontal hodoscopes in the two arms is less than three.

Pion signature The pion signature (π^+,π^-) of arm i (i=1,2) is therefore a coincidence of a hit in vertical hodoscopes, horizontal hodoscopes, no hit in the

Cerenkov counters and a signal coming from preshower:

$$VH_i \cdot HH_i \cdot \overline{C_i} \cdot PS_i \text{ for i=1,2}$$
 (4.1)

Electron signature The electron signature (e^+,e^-) of arm i (i=1,2) is a coincidence of a hit in vertical hodoscopes, horizontal hodoscopes, a hit in the Cerenkov counters and a signal coming from preshower:

$$VH_i \cdot HH_i \cdot C_i \cdot PS_i \text{ for i=1,2}$$
 (4.2)

The decision from both arms are combined to produce the final first level decision (π_1, π_2) for pion pairs and (e_1, e_2) for electron pairs. The electronic of the T1 trigger gives a result within 120ns. The vertical hodoscopes is used to define the timing of the pions or electrons and establish the time coincidence window.

 Λ signature In addition to the pions and electron pair signature the first level trigger also accepts events which are likely to come from a Λ decay $\Lambda \to p + \pi^-$. Due to the asymmetric kinematics of this decay the Λ signature is defined as:

$$(VH_1[17] \cdot HH_1 \cdot \overline{C_1} \cdot PS_1) (VH_2[1-16] \cdot HH_2 \cdot \overline{C_2} \cdot PS_2)$$
 (4.3)

For the vertical hodoscopes only slab 17 is used in arm 1 while for arm 2 the slabs 1 to 16 are looked at. Because there is not use of accidental events for this sub-trigger, the coincidence time window is reduced to ± 2.5 ns.

'Copl' signature At this stage also the decision 'Copl' from the Coplanarity selection processor is obtained, which reduces the trigger rate by a factor of 2.

In short for the data taking period we are considering (Ni, 2001) there are the following trigger configuration which have been accepted:

- $T1\pi^+\pi^-$ Copl
- e⁺e[−]
- Λ

4.4 Neural Network Trigger DNA

The DIRAC neural network trigger (DNA) [58] is a processing system which uses a neural network algorithm. DNA receives as input the hit patterns of VH1, VH2, the x-planes of the ionization hodoscopes and optionally the two preshower detectors. Figure 4.2 shows the setup and the detectors used for DNA. DNA is able to

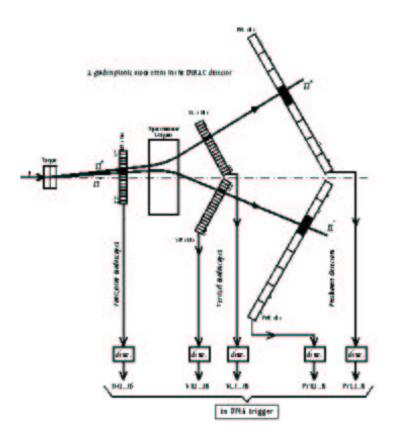


Figure 4.2: Scheme of the DNA neural network trigger.

cope with up to 2 hits per VH plane and up to 5 hits per IH x-plane. Events with more hits are accepted for further off-line evaluation. Each x-plane in conjunction with the input signals from the two VH are evaluated independently and simultaneously. Both decisions are then put in OR in order to eliminate inefficiencies due to gaps between the ionization hodoscope slabs:

$$(VH_1 \cdot VH_2 \cdot IH_{x,1}) \wedge (VH_1 \cdot VH_2 \cdot IH_{x,2}) \tag{4.4}$$

The neural network was trained to select particle pairs which have low relative momenta: $Q_x < 3 \text{MeV/c}$ and $Q_{long} < 30 \text{MeV/c}$. The training was first performed with Monte Carlo simulated data and then rechecked with real experimental data. The acceptance for low Q events using the full trigger is discussed below and is shown graphically in figure 4.5.

The DNA starts with a T0 signal and processes an event in about 210 ns. In a second step the decision of it is put in coincidence with that one from T1 so that only events that have a positive decision from T1 and DNA are further processed. The DNA rejection rate is about 2.3 with respect to T1 and the efficiency for the low Q region of the order of 94% .

4.5 Fourth Level Trigger T4

The T4 trigger uses the drift chamber information to reconstruct straight tracks in x-direction which in turn allows to select events with small relative momenta. The T4 trigger works in two stages; first the track finder evaluates the hit wire information from the drift chamber to select tracks, then the track analyzer compares the found pattern with the patterns from a look-up table. The look-up table is constructed from measured data and includes all possible patterns coming from tracks with relative momenta of $Q_x < 3 \text{MeV/c}$ and $Q_{long} < 30 \text{MeV/c}$.

Track finder In the first stage the T4 track finder evaluates the hit wire information from the drift chamber to find straight tracks. Drift times are not used. The track finder uses the endpoint method: drift chamber planes X1 (or X2) and X5 (or X6) are the base planes for the track search. For each combination of hits in the two base planes the algorithm defines hit windows for the intermediate x-planes and the number of detected hits in these hit windows are counted. A track is established if the number of detected hits of a track is bigger than 3. Parasitic combinations (i.e. repeated track identifiers) are suppressed by the track finder.

Track analyzer Once a track is found the track analyzer is invoked. The look-up table of the track analyzer allows to relate all relevant track combinations with

relative momenta of $Q_x < 3 {\rm MeV/c}$ and $Q_{long} < 30 {\rm MeV/c}$. These 'allowed' combinations were obtained using simulation and the precise knowledge of the geometry of the setup. The track analyzer obtains the track parameters, compares them with the look-up memory and issues a positive or negative decision.

Operation modes T4 can be run in different operation modes. The standard mode stops T4 for a negative DNA decision. Also because of the variable event decision time – which depends on the events complexity – a time cut is applied which generates after a preset time window unconditionally a positive decision. This time-cut is introduced to reduce dead-time. In the standard mode the average rate reduction with respect to T1 is about 5, while the efficiency for Q < 30 MeV/c exceeds 99% (see figure 4.3).

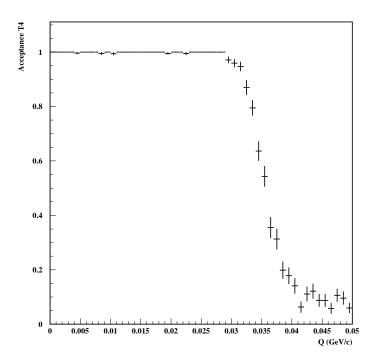


Figure 4.3: Acceptance of the T4 trigger in Q in GeV/c for events with $|Q_x| < 3$ MeV/c and $|Q_y| < 3$ MeV/c.

4.6 Rate and Acceptance

For typical experimental conditions the rate after applying T1 is about 5000/spill, after DNA it drops to 2000/spill and after T4 to 700/spill. The calibration triggers e^+e^- and Λ are prescaled with 14 and 6, respectively and yield about 7% of the total accepted event sample.

The acceptance of different triggers as a function of Q is shown in figure 4.4. The selected triggers are $T1\pi\pi$ Copl (black), DNA (blue), T4 (green) and full trigger $T1\pi\pi$ Copl*DNA*T4 (red). The acceptance for low Q events is shown in

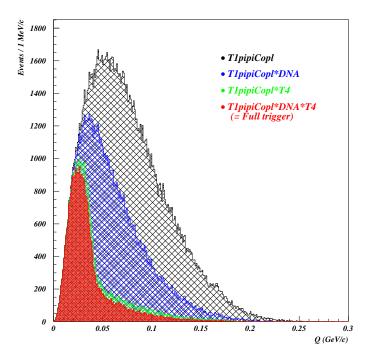


Figure 4.4: Total relative momentum for selected triggers: $T1\pi\pi$ Copl (black), DNA (blue), T4 (green) and full trigger $T1\pi\pi$ Copl*DNA*T4 (red).

figure 4.5 and is for the full trigger around 95%.

The complete trigger provides a reduction factor of 1000 with respect to the signal counting rate of the downstream detectors while at the same time keeping events with low relative momenta. In addition, the Q acceptance above 15 MeV/c is reduced by the full trigger.

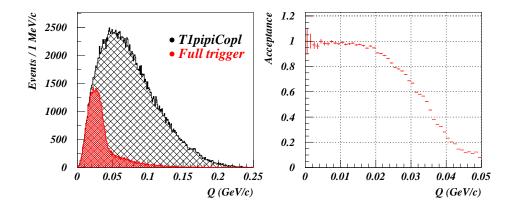


Figure 4.5: Total relative momentum for first level trigger $T1\pi\pi$ Copl (black) and full trigger $T1\pi\pi$ Copl*DNA*T4 (red) on the left and the acceptance of the full trigger relative to T1 on the right.

Chapter 5

Data Acquisition System - DAQ

The DAQ system has been specially designed to cope with the time structure of the proton beam. The machine super-cycle of the CERN PS accelerator has a duration of 15-20s. DIRAC receives protons within this super-cycle in spills of 400-450ms width, from 1 to 5 spills per super-cycle. The interval between spills can be as short as 1s.

During the accelerator burst the data from all detectors are read out into VME buffer memories without any software intervention. The data transfer to the VME processor boards, the event building, the data transfer to the main host computer and other relatively slow operations are performed during the pause between bursts.

The operation rate of the DAQ has to deal with 2048 channels from MSGC, 512 channels from SFD, 2016 channels from the drift chambers and 224 channels from other scintillation detectors and from the Cerenkov detector. For every channel, the time, the amplitude or both are read out. In addition to the main readout mode, the readout of the scalers at the end of every spill is arranged via a CAMAC bus. Also the counting rates of all detectors, the trigger rates of the different trigger levels and the value of the beam intensity are transfered to the host computer.

5.1 DAQ hardware

The data readout is arranged using 12 readout branches: Four branches come from the MSGC, three branches from the DC system and five FERA branches for the other detectors. The models used in the FERA and DC branches are the VME CESHSM 1870 and the LeCroy 1190 modules. The MSGC branches use dedicated VME modules. The FERA branches include different FERA compatible LeCroy modules. The details of the used hardware can be found here [59, 60, 61].

The read-out system is installed as follows: The first level trigger T1 starts the digitalization of the ADC and TDC of the FERA and the DC branches. The read-out of the modules to the buffer memories is inhibited until there is a decision from T4. If the decision is positive, the data are transferred to the buffer memories, if the decision is negative, a fast clear is issued. In contrast to the above, the MSGC branches are read-out directly after a positive decision of DNA. This reduces the dead time since the MSGC read-out electronics takes longer. A negative decision of T4 will thus only clear the MSGC data. If the T4 decision is positive, the MSGC data is transferred to the buffer memories.

The total read-out time per event takes 45μ s which is limited by the fixed read-out time of the MSGC branches.

5.2 DAQ software

The main part of the DAQ software runs on two VME processor boards and on the main DAQ host and is described here [62].

A schematic view of the DAQ process is illustrated in figure 5.1. The basic processes that run on the VME platform and on the DAQ main host are shown. In addition the figure also shows some processes on a further monitoring computer.

The DAQ software process can be split up into different stages. The first stage contains the read-out programs (which run on the VME boards) and the event builder software (on the main host). During the event building the data are checked for consistency. The second stage then includes programs for data distribution (primary data receiving and primary data sending) over the network and for on-line monitoring. The primary data receiver is crucial for the data acquisition system because it is the only component to receive data directly from the event builder and it has therefore to run at all times. The third stage bundles some programs to control the run status. It allows to set parameters, to select the different trigger types and to change the run status (stop, run, pause). In addition it displays the user information about the current run status. The forth stage finally incorporates programs that control the slow-control process providing access to any hardware of the DAQ system. These programs allow for example to control high voltage.

The DAQ system has been designed to accept data from five consecutive bursts in one super-cycle with up to 2 MBytes of data per burst, to build the events and to distribute the data finally to the central computing facilities.

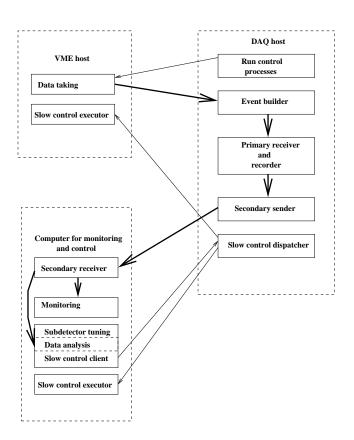


Figure 5.1: Layout of the DAQ architecture.

Chapter 6

BASEL Tracking

The BASEL extended tracking for the DIRAC experiment [63] is a development based on the standard offline code ARIANE [64]. It was developed to improve on some issues of the standard tracking procedure and has therefore also influenced the standard ARIANE tracking code. By virtue of its independence it can also be used to cross-check results obtained from the standard DIRAC tracking code.

6.1 Introduction

The tracking procedure for pion pairs in the DIRAC experiment can be separated into two parts: downstream and upstream tracking. In addition, the tracking algorithm itself can be split into pattern recognition (i.e. track finding) and track fitting.

The tracking algorithm starts at the downstream detectors. Each track is measured with high precision in the drift chambers. The relative timing of the two tracks is obtained from the time-of-flight information of the vertical hodoscopes. The absolute total lab momentum p_{tot} is determined by the drift chamber information, by the parametrized magnetic field and the position of the target, which is assumed to be the origin of the particles. The total momentum is then fine-adjusted with the X plane of the SFD detector. Making use of a Kalman filter and the target as a supplementary measurement point, one finds the x and y projections of the total momentum. The ionization hodoscopes (IH) is used to resolve ambiguities for multi-hit events in the SFD. Once the absolute momentum is found, the relative momentum Q can be determined. Since the two pions have small relative opening angle, Q in the center of mass system (CMS) is also small.

This chapter is organized as follows: First a quick overview of the Kalman filter procedure is given. Then the Basel track finding and track fitting is explained.

6.2 Kalman Filter

The Kalman filter algorithm has a 'progressive' approach. It first predicts for each measurement an extrapolated state at this point, then it corrects it with the measurement to yield the final filtered value. The filtered value is the best estimate of the state, taking into account all prior measurements.

This is exactly the progressive approach of the filter: It updates the state and its covariance matrix with every measurement. Hence the predictions become more and more accurate.

6.2.1 Prediction

For each measurement point, the algorithm first calculates a prediction. This prediction is based on the 'System Equation', which describes the evolution of the true state of our system, i.e.

$$x_{t+1} = A_t x_t + \omega_t \tag{6.1}$$

Here x_{t+1} and x_t denote the state at times t+1 and t, A_t is a (n×n)matrix, that incorporates the evolution of the system from time t to time t+1. ω_t represents the white, Gaussian-distributed noise of the process. Its mean equals 0. Whiteness implies that the process noise is not correlated in time.

For tracking purposes, the state vector x_t incorporates the coordinates and the velocity vector of the particle at any given time t, i. e.

$$x = \begin{pmatrix} Coordinate \ 1 \\ Coordinate \ 2 \\ \dots \\ Velocity \ 1 \\ Velocity \ 2 \\ \dots \end{pmatrix}$$

The evolution matrix A describes how the coordinates and the velocities change over time. This can be a straight line for the case of no external field, but it can also be a circle or a helix for example, if there is a magnetic field present. The process noise ω_t is the multiple scattering at time t. It changes the state vector randomly.

If, for example, we have a two-dimensional space (yz) with no external field and a particle moving with constant speed (no energy loss) along the z-axis, the system equation can be written as (see Eq.1):

$$x = \begin{pmatrix} y \\ v_y \end{pmatrix} \xrightarrow{(1)} \begin{pmatrix} y_{t+1} \\ v_{y_{t+1}} \end{pmatrix} = \begin{pmatrix} 1 & \Delta t \\ 0 & 1 \end{pmatrix} \cdot \begin{pmatrix} y_t \\ v_{y_t} \end{pmatrix} + \begin{pmatrix} \delta y_t \\ \delta v_{y_t} \end{pmatrix}$$
(6.2)

The y coordinate at any time t+1 can be written as

$$y_{t+1} = y_t + v_{y_t} \cdot \Delta t + \delta y_t \tag{6.3}$$

The multiple scattering (MS) δy_t changes the y coordinates randomly. The velocity vector v_{y_t} is also changed by the MS process at each scatterer:

$$v_{y_{t+1}} = v_{y_t} + \delta v_{y_t}$$

So y_{t+1} and $v_{y_{t+1}}$ have to be updated after each scatterer.

The true state x_t is not known, it can be estimated as \hat{x}_t . To predict the state at time t+1 the best we can do is (since we don't know the true MS, we set it equal to its mean, which is zero):

$$E[x_{t+1}] = \hat{x}_{t+1}^P = A\hat{x}_t \tag{6.4}$$

The index P denotes prediction. Not only can we predict the state at time t+1, also the covariance matrix $P_{\hat{x}_t}$ of the state at time t can be extrapolated to t+1:

$$E[(x_{t+1} - \hat{x}_{t+1}^P)(x_{t+1} - \hat{x}_{t+1}^P)^T] = P_{\hat{x}_{t+1}}^P = AP_{\hat{x}_t}A^T + \Omega$$
 (6.5)

 Ω is the covariance matrix of the process noise ω and is connected in the following way:

$$p(\omega) \sim N(0, \Omega)$$

where N(...) represents a normal probability distribution.

6.2.2 Correction

If we obtain a measurement z_{t+1} at time t+1, we can 'correct' the prediction of the state with this measurement. The measurement itself has an error r_{t+1} and is connected to the true state by the 'Measurement Equation':

$$z_{t+1} = H \cdot x_{t+1} + r_{t+1} \tag{6.6}$$

The linear (m×n) matrix H translates the true state x_t to the frame of the measurement z_t . r_t represents the measurement error which is also white and Gaussian-distributed around 0. It is connected to the measurement noise covariance matrix R_t by:

$$p(r) \sim N(0, R)$$

where N(...) represents a normal probability distribution.

For our example above, if we have a detector measuring the y coordinate, equation (6.6) becomes:

$$z_{t+1} = \begin{pmatrix} 1 & 0 \end{pmatrix} \cdot \begin{pmatrix} y_{t+1} \\ v_{y_{t+1}} \end{pmatrix} + r_{t+1}$$
 (6.7)

$$z_{t+1} = y_{t+1} + r_{t+1}$$

This makes sense: The measured y value is composed of the y coordinate of the true state plus the measurement error.

The weights of how the prediction and the measurement enter into the corrected (=filtered) value are incorporated in the **gain matrix K**:

$$K_{t+1} := (P_{\hat{x}_{t+1}}^P H^T) (R_{t+1} + H P_{\hat{x}_{t+1}}^P H^T)^{-1}$$
(6.8)

Now we can correct the predicted value and its covariance matrix by applying the weights in K:

$$\hat{x}_{t+1}^F = \hat{x}_{t+1}^P + K_{t+1} \{ z_{t+1} - H \hat{x}_{t+1}^P \}$$
(6.9)

F stands for 'filtered' (= corrected). The filtered covariance matrix becomes:

$$P_{\hat{x}_{t+1}}^F = \{I - K_{t+1}H\}P_{\hat{x}_{t+1}}^P \tag{6.10}$$

What does this imply? The gain matrix K weights the measurement and the prediction of a state at time t+1 according to their relative errors. This can easily be seen by taking the limit of no measurement error

$$\lim_{R_{t+1}\to 0} K = H^{-1} \xrightarrow{(9)} \hat{x}_{t+1}^F = H^{-1} z_{t+1} = \hat{x}_{t+1}$$
 (6.11)

In this case \hat{x}_{t+1}^F becomes simply $H^{-1}z_{t+1}=\hat{x}_{t+1}$. The more accurate the measurement is compared to the prediction, the more it is weighted. In the limit of no measurement error, only the measurement is used. The same logic applies vice versa. For no prediction error

$$\lim_{P_{\hat{x}_{t+1}}^P \to 0} K = 0 \xrightarrow{(9)} \hat{x}_{t+1}^F = \hat{x}_{t+1}^P$$
 (6.12)

K becomes zero and \hat{x}_{t+1}^F is equal to \hat{x}_{t+1}^P . The measurement has no influence on the filtered value for this case.

Prediction - Correction View Therefore the Kalman Filter algorithm can be seen as a feedback control. It predicts the state at some time and then corrects it by some (noisy) measurement.

6.2.3 Error of Prediction

The mean \hat{x}_t^F and the covariance matrix $P_{\hat{x}_t}^F$ fully describe the Gaussian-distributed conditional probability density function of the true state x_t . But what would be

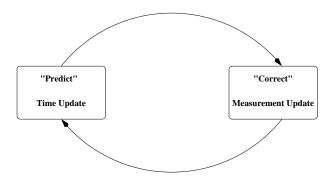


Figure 6.1: The ongoing Kalman Filter cycle. Time Update predicts the current state estimate ahead in time. The measurement update corrects the projected estimate by an actual measurement at that time.

interesting in this context is the distribution of the error of the estimate, denoted as

$$e_t = x_t - \hat{x}_t^F \tag{6.13}$$

It can be shown that (Maybeck[65], P.226)

$$E[e_t|z_t, z_{t-1}, \dots] = 0 (6.14)$$

and

$$E[e_t e_t^T | z_t, z_{t-1}, \dots] = P_{\hat{x}_t}^F$$
(6.15)

Thus, \hat{x}_t^F is an unbiased estimate of the true state. In addition, the $P_{\hat{x}_t}^F$ calculated through (10) assumes additional significance: it is the covariance to describe the Gaussian error committed to the estimate.

6.2.4 Optimality Criterion

As already stated, \hat{x}_t^F is the optimal estimate of the true state x_t given all prior measurements. It is optimal in the sense, that it is the mean, the median and the maximum likelihood estimate of the entire probability density function of x_t , conditioned on all available information (prior measurements). The covariance $P_{\hat{x}_t}^F$ can then be seen as either the covariance of this conditioned probability density function, as well as the covariance of the Gaussian error between x_t and \hat{x}_t^F .

Another optimality criterion for an estimate \hat{x}_t^F would be, that it minimizes the covariance

$$E[ee^{T}],$$
 where $e_{t} = x_{t} - \hat{x}_{t}^{F}.$ (see Eq. (11) and Eq. (13))

It is then called the minimum mean square error estimate (MMSE). By virtue of being the conditional mean, \hat{x}_t^F is also the MMSE.

In fact it can be shown, that the conditional mean of a Gaussian-distributed cond.p.d.f. minimizes any function of the form $E[eMe^T]$. As a consequence, also the least square sum over all filtered residuals $[z_t - H\hat{x}_t^F]$ with any weight matrix M is minimized:

$$\chi^2 = \sum_{t=1}^n \left[z_t - H \hat{x}_t^F \right] M \left[z_t - H \hat{x}_t^F \right]^T$$
 (6.16)

Specifically, one can choose the covariance matrix Q_t^F of the filtered residuals: $M = (Q_t^F)^{-1} = (R_t - H_t P_t^F H_t^T)^{-1}$. For Q_t^F to have an inverse matrix, it has to be positive definite.

This means for our previous example that the χ^2 sum of the residuals

$$[z_t - H\hat{x}_t^F] = z_t - z_t^F \tag{6.17}$$

is minimized. $(z_t)^F$ is the transformation of the filtered value in the z-measurement frame.

6.3 Downstream track finding and fitting

The BASEL tracking algorithm starts downstream by fitting a straight line using the information available from the drift chambers, the vertical hodoscopes (VH) and the horizontal hodoscopes (HH) and the preshower (PrSh). Once a track is established, a first approximation to the total lab momentum can be calculated.

6.3.1 Selection of track candidates

As a first step the drift chamber information is used to construct tracks by hit wires and drift times. The algorithm forms a 'track road' connecting the hits from the wires in the first and the last plane of x (or y) orientation to a straight line. The interpolated intersections of this straight line with the other DC planes are then compared to the measured hits. If there are more than three measured hits close to the constructed line on all DC planes together, the constructed line becomes a track candidate.

Once a track candidate is established, the tracking program extrapolates it to the VH and the HH detectors and checks whether it matches a hit slab geometrically and time wise. In addition, a correlated hit is also required in the PrSh. All track candidates with corresponding hits are selected for further processing.

The number of found track candidates depends mostly on the efficiency of the DC reconstruction which in turn is related to the intensity of the incoming beam. For the whole of 2001 we have around 96% with only one track candidate for the negative arm, and 92% for the positive one¹. The remaining events are predominantely two-track events.

Due to the increased ambiguity which events with higher track multiplicities generate at the SFD, we reject higher multiplicity events.

6.3.2 Track fitting

The next stage of the tracking algorithm establishes the parameters of the track candidates found in the DC's using a χ^2 fit². In general terms, the track parameters θ are the solution to the equation

$$\begin{pmatrix} a_{11} & \cdots & a_{1n} \\ \vdots & \ddots & \vdots \\ a_{p1} & \cdots & a_{pn} \end{pmatrix} \begin{pmatrix} \theta_1 \\ \vdots \\ \theta_n \end{pmatrix} = \begin{pmatrix} m_1 \\ \vdots \\ m_p \end{pmatrix}$$
(6.18)

¹The difference between the positive and the negative arm stems mostly from additional proton admixture in the positive arm and the trigger, which starts with a signal in the positive arm.

²This stage is identical to ARIANE. A very detailed description of the DC track fit can be found here [66]. What follows is a short explanation of the used procedure.

The vector m contains the measured coordinate in the local frame³. The matrix A is a transformation matrix. The length of the measurement vector m is up to $L_m = 14$. Assuming a straight line, the track is described by 6 parameters: 3 coordinates and 3 unit vectors $(\theta_X, \theta_Y, \theta_Z, \theta_{ax}, \theta_{ay}, \theta_{az})$.

To reduce the parameter space, we define for all track candidates the parameter θ_Z as the Z-coordinate of the exit membrane of the vacuum chamber in front of the DC planes. In addition, the angles are defined with respect to θ_{az} , so that we can set $\theta_{az}=1$. This reduces the number of parameters to 4 and the dimensions of the transformation matrix A to $[L_m,4]$. The measurement errors which are induced by multiple scattering define the measurement error matrix D. Its component D_{ij} for example corresponds to the uncertainty induced by the multiple scattering in plane i on the measurement in plane j.

If we now apply the standard χ^2 method, defining the error matrix of the track parameters as E_{θ} , we obtain:

$$B = A^{T} \cdot D^{-1} \cdot A$$

$$\theta = B^{-1} \cdot A^{T} \cdot D^{-1} \cdot m$$

The errors of the track parameters can be calculated as:

$$E_{\theta} = B^{-1}$$

and the χ^2 value is equal to:

$$\chi^2 = (m - A \cdot \theta)^T \cdot D^{-1} \cdot (m - A \cdot \theta)$$

6.3.3 Momentum determination I

Once the DC track parameters are established, one can generate a first momentum determination which relies on the assumption, that the track originates from the target. This is possible, because there exists a unique relation, see equation 6.19, assuming a homogeneous magnetic field in y direction, with no magnetic field component in x and z direction (Fernow [67], P. 327):

$$\sin(a) + \sin(b) = \frac{\int B \, dl}{3.33p}$$
 (6.19)

Where a and b are the incident and exit angle, B is the magnetic field in y direction, p the total momentum of the particle and dl is the integration over the path of the particle in the magnetic field, see figure 6.2.

³The local frame has only one coordinate. It is the matrix A which transforms the track parameters from the global to the local frame.

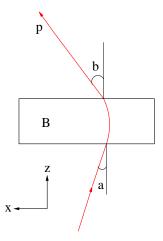


Figure 6.2: Scheme of the particle flying through the magnet. a is the entrance angle, b the exit angle, B the vertical magnetic field in y direction and p is the absolute value of the total momentum.

The calculation itself is done by an iterative procedure. The magnetic field is described in polynomial form. The momentum determination and the track parameters obtained with the DC fit allow to extrapolate the DC track to the upstream detectors. In addition, the tracks need to be within the geometrical magnet aperture as well as within the active area of the upstream detectors.

6.4 Upstream track finding and fitting

The upstream track finding and fitting first refines the total momentum determination using a measurement in the SFD X plane. It then uses a Kalman filter to lead the track through the other SFD plane to the target.

6.4.1 Ambiguity of prompt events

The signal events we are looking for exhibit very small time differences. The accidental pairs on the other hand have well defined absolute time differences of more than 5 ns. This leads to a different treatment of prompt versus accidental events.

If the tracks of a prompt event are extrapolated to the upstream detectors, there are mostly two good hit candidates for each track to choose from. For accidental pairs, due to their large time difference, there is normally just one.

Figure 6.3 illustrates the problem: For prompt events, $|t_3-t_4|<0.5ns \rightarrow |t_1-t_2|<4.2$ ns (at 3σ confidence level). The chosen time cut for the SFD X

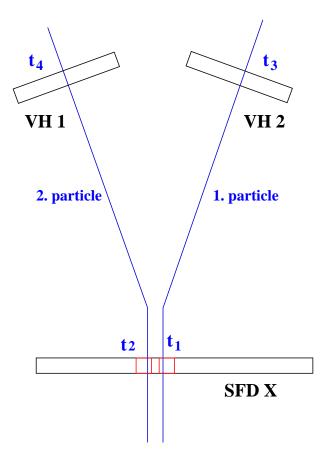


Figure 6.3: Measured times upstream and downstream in the DIRAC setup for $\pi^+\pi^-$ pairs.

plane (details see below) would accept both hits for both particles. For a typical accidental event, however, the time difference at the level of VH is around 10 ns. This leads to an equal time difference at the level of SFD X. Due to the time cut, the tracking would thus only find one good hit candidate per track.

In order to treat prompt and accidental events equal, we search for hit candidates in the upstream detectors using the time information of both arms: Track 1 is extrapolated to SFD X using its intrinsic time in the VH, t_3 , but also the VH time of the other track, t_4 . Thus each track has two time information per SFD plane. Such a mechanism makes sure that both, prompt and accidental pair events, are treated equally.

This method is applied to find hit candidates on both layers of the SFD.

6.4.2 Track finding in SFD X

In a first step the measurements of the X plane in the SFD detector are checked against a geometrical (equation 6.20) and time cut (equation 6.21).

Geometrical cut For the geometrical cut we use as ARIANE a 6 σ interval taking into account the multiple scattering. The beam movement is also considered by adding 0.2cm. This defines a total acceptance region for hit candidates on the SFD X layer of:

Acceptance region =
$$\pm \left(0.2 + \frac{4.8}{p_{tot}[GeV/c]} \text{ cm}\right)$$
 (6.20)

Time cut For the time cut we use a slightly looser cut. In agreement with AR-IANE we accept measurements that occur within 4 ns around the predicted time of the track:

$$\Delta t \text{ (VH} \rightarrow \text{SFD X)} \leq \text{ Time of Flight } \pm 4 \text{ ns}$$
 (6.21)

Judging from figure 6.4, this amounts to more than 3σ acceptance.

The measurement closest to the extrapolation is consequently selected for each track.

Double ionization cut In case both tracks select the same hit fiber on SFD X, the tracking algorithm checks the ionization hodoscopes. Specifically it looks in the first two X layers of the IH detector for a time- and space correlated hit pattern originating from a double ionization hit or from two adjacent single ionization hits. If there is such a pattern, the event is accepted. If not, the program looks for a close-lying second hit around in the SFD X to move one of the tracks to this second hit. Which track is moved to the other hit candidate is decided at random. The resulting decision tree is shown graphically in figure 6.5.

6.4.3 Momentum refinement using the SFD X hits

Once the hit SFD X fiber is established, the total laboratory momentum of the track is fine-adjusted. This fine-tuning is an iterative procedure: The total momentum of the track is adjusted so that it passes exactly through the selected hit fiber. This is achieved by writing the function (the θ vector incorporates the track parameters):

$$\theta_{upstream} = f(\theta_{DC}, p_{tot}) \tag{6.22}$$

up to the linear term with respect to the total momentum p_{tot} :

$$p_{tot}^{1} = p_{tot}^{0} + \frac{\Delta p_{tot}}{\Delta x} \cdot \Delta x^{0}$$
 (6.23)

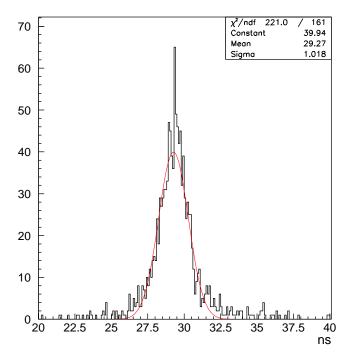


Figure 6.4: Time difference for single tracks between VH and SFD X. All events are required to have only one hit per SFD plane. The $\sigma_t \approx 1 ns$, so a 3 σ environment would correspond to 3 ns.

 p_{tot}^0 is the zero-th approximation of the momentum (see section 6.3.3). p_{tot}^1 becomes the linear correction of the total momentum. Δx^0 is the difference between the estimated x coordinate of the track, x_{track}^0 , using p_{tot}^0 , and the desired hit fiber:

$$\Delta x^0 = x_{track}^0 - x_{fiber} \tag{6.24}$$

The iteration algorithm (Newton-Raphson) now uses p_{tot}^1 to obtain x_{track}^1 and dx^1 . Then the second correction to the total momentum is calculated:

$$\Delta x^{1} = x_{track}^{1} - x_{fiber}$$
$$p_{tot}^{2} = p_{tot}^{1} + \frac{\Delta p_{tot}}{\Delta x} \cdot \Delta x^{1}$$

 P_{tot} is refined until dx becomes small as compared to the SFD fiber width (until the ratio $\frac{dx}{\text{fiber width}}$ becomes smaller than 10^{-2}).

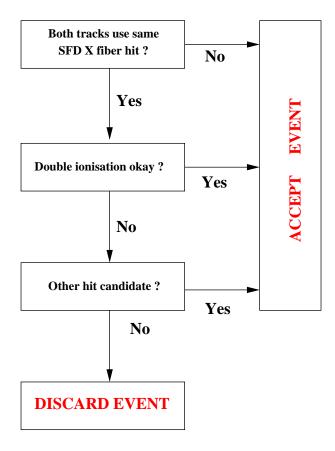


Figure 6.5: Decision tree for the track finding at the level of SFD X.

6.4.4 Smearing P_x within one fiber

The tracking algorithm also allows to distribute the track over the entire fiber width in order to smear P_x . For this purpose, x_{fiber} is uniformly chosen over the entire column width.

6.4.5 Track finding in SFD Y

The track finding algorithm that we use for the SFD Y plane does not use the magnetic field description – which was used for the SFD X plane – but uses instead the track parameters as established in the DC system and the assumption that the tracks originate from the target. We developed this different algorithm in order to increase the accuracy of the SFD Y prediction. It is described in detail as an internal note [68].

Geometrical cut As for the SFD X plane, the geometrical cut used for the SFD Y plane includes a 6 σ interval. The cut is defined as:

Acceptance region =
$$\pm \left(0.2 + \frac{4.8}{p_{tot}[GeV/c]} \text{ cm}\right)$$
 (6.25)

For the timing restriction, the algorithm controls the time difference between the VH and SFD Y as well as the time difference between the two SFD layers. The two cuts read:

Time cut VH - SFD Y In agreement with ARIANE the following cut is used:

$$\Delta t \text{ (VH} \rightarrow \text{SFD Y)} \leq \text{ Time of Flight } \pm 4 \text{ ns}$$
 (6.26)

Time cut SFD X - SFD Y For the SFD Y time cut a 3 σ interval around the relative timing between the two planes of SFD is chosen. The relative timing is obtained by using single tracks and allowing only one hit per SFD plane. Figure

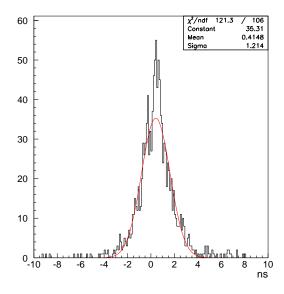


Figure 6.6: Time difference for single tracks between the two SFD planes. All events are required to have only one hit per SFD plane. The $\sigma_t \approx 1.2ns$, so a 3 σ environment would correspond to 3.6 ns. The mean equals 0.4 ns.

6.6 shows the relative timing of the two SFD planes. The mean is around 0.4 ns and the σ is around 1.2 ns, so we can take as a time cut for SFD Y:

$$\Delta t(SFD X - SFD Y) < 0.4 \pm 3 \cdot 1.2 \ ns = 0.4 \pm 3.6 \ ns$$
 (6.27)

Double ionization cut For events in which both tracks pass through the same SFD Y fiber, the program requires a time- and space correlated double ionization signal in the Y layers of IH. Figure 6.5 describes the decision tree also for the Y plane.

6.4.6 Smearing P_u within one fiber

As for the SFD X, the track program allows to distribute the track uniformly over the entire SFD Y slab width. This is achieved by randomly changing the measured y coordinate within one fiber. The Kalman filter procedure does then subsequently use the smeared value.

6.4.7 Track finding in the MSGC

The MSGC measurements are not used in the Basel tracking.

6.4.8 Target measurement

The target is included in the tracking as a measurement point. Specifically, the beam position is taken as the target's X and Y coordinate, the measured beam width then giving the uncertainty.

6.4.9 Upstream track fitting - Kalman filter procedure

After establishing the hit candidates in SFD X, the total momentum is fine-adjusted. Then the SFD Y hit candidates are found, as well as the target point and the Kalman filter routine is started to extrapolated the track parameters to the target.

Propagation of DC track parameters to SFD X First the DC track parameters and their covariance matrix are propagated through the magnet to SFD X. Then the covariance matrix is updated with all the MS coming from membranes in between.

State vector The state vector used for the Kalman filter can now be described as:

$$\hat{x}_{t} = \begin{pmatrix} x_{SFDX} \\ y_{SFDX} \\ z_{SFDX} \\ v_{x} \\ v_{z} \\ v_{y} \\ v_{z} \\ v_{z}$$

 v_x , v_y and v_z are the x, y and z direction-vector of the track. v_x and v_y are normalized to v_z in the state vector (6.28). This normalization has the convenient property that we can immediately calculate the momentum projections: Since the

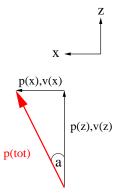


Figure 6.7: Geometry of the momentum. The red arrow symbolizes the projection of the total momentum onto the XZ plane. The direction vectors and the momentum projections can be set into a correspondence $\frac{v_x}{v_z} = \tan(a) = \frac{p_x}{p_z}$.

normalization of v_x with respect to v_z is directly tan(a), see figure (6.7), we have :

$$p_x^2 + p_y^2 + p_z^2 = p_{tot}^2 = \left(\left(\frac{v_x}{v_z} \right)^2 + \left(\frac{v_y}{v_z} \right)^2 + 1 \right) p_z^2$$
 (6.29)

Hence knowing the total momentum and the direction vectors yields immediately the projections of the momentum on the x and y axis.

Kalman filtering The Kalman filtering now uses the SFD Y measurement and the target measurement to update the state vector and extrapolate it to the target. Figure (6.8) shows how Qy changes using the SFD Y measurement. Figure 6.9 illustrates the target picture of reconstructed tracks before the target is put into the Kalman filter. It gives an idea of the accrued MS from the DC to the target. The x

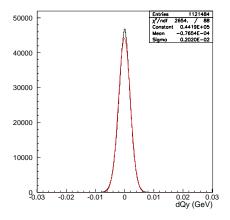


Figure 6.8: The change in Qy by applying the Kalman filter for the measurement obtained with the ARIANE method.

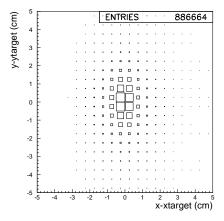


Figure 6.9: Target picture in the XY plane for tracks coming from arm 1.

and y projections are shown in figure (6.10). Most tracks are within 1.5 cm in x direction and 2 cm in y direction.

The plots in figure 6.10 can be used to cross check the tracking algorithm: In x direction, the total momentum is corrected with a SFD X slab. This implies that the track passes through the SFD X slab and is very precisely defined at this point. The multiple scattering expected at the target in x direction comes therefore from the way between the SFD X plane and the target. From MC we obtain that this corresponds to an uncertainty of:

$$\sigma_x = \frac{1.0}{p_{tot}} \left[\text{GeV/c cm} \right] \tag{6.30}$$

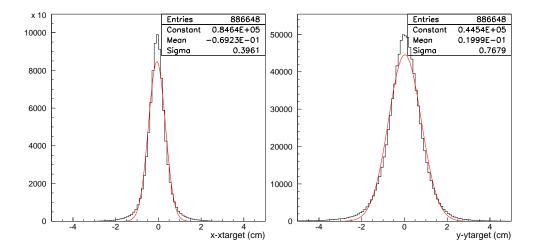


Figure 6.10: Target picture in the X or Y plane for tracks coming from arm 1.

On the other hand, the y direction of the track is precisely known at the first drift chamber⁴. All uncertainty in the target in y direction comes therefore from the way between the first DC set and the target. Using MC we establish that this corresponds to an uncertainty of:

$$\sigma_y = \frac{2.0}{p_{tot}} \left[\text{GeV/c cm} \right] \tag{6.31}$$

These values can now be used to cross check the track reconstruction: The mean of p_{tot} is around 2.5 GeV/c. Dividing the two MS values above by 2.5 yields

$$\sigma_x = \frac{1.0 \text{ [GeV/c cm]}}{2.5 \text{[GeV/c]}} = 0.4 \text{ cm}$$

and

$$\sigma_y = \frac{2.0 \text{ [GeV/c cm]}}{2.5 \text{[GeV/c]}} = 0.8 \text{ cm}$$

Comparing the thus obtained sigmas with the ones from the target projection in figure (6.10) shows that they are in good agreement.

6.4.10 Momentum calculation at the target

The state vectors of the tracks at the target level can be used to calculate the relative momenta in the CMS. We do this by first transforming the direction vector into

⁴The hit in the SFD Y is hence not used

the momentum projections, as demonstrated above in equation (6.29). Then the absolute momenta are transformed into the relative momenta by using a Lorenz transformation.

6.4.11 Overview of the BASEL tracking

An overview of the BASEL tracking is given in figure 6.11.

6.5 Treating accidentals like prompt events

As mentioned in section 6.4.1 the track finding for two track events at the SFD detector uses the timing in the vertical hodoscopes of both tracks. This method treats prompt and accidental events equally; in both cases the use of two different time information creates an ambiguity for the track finding to select a hit fiber. This ambiguity would only exist for prompt events, but not for accidental events, if only the corresponding time of each track in the VH is used.

The use of the measured accidental spectrum for the analysis asks for a further correction to the accidentals: The peak-sensing circuit (PSC) [50] installed in the SFD detector treats accidental pairs and prompt pairs differently. If a time correlated event hits two adjacent fibers, they are sometimes merged into one single fiber. If, on the other hand, the absolute time difference between the two hits in the SFD is larger than 4 ns, the merging does not occur anymore. The inefficiencies of adjacent hit fibers due to the PSC was estimated previously [51, 52].

In addition, the read-out electronics of the SFD suppresses events which hit the same column in SFD, but are not time-correlated: The time gates of the TDC of the SFD are 20 ns. If an accidental event with a time difference in the VH of, say, 10 ns passes through the same fiber in the SFD X or Y layer, only one hit is recorded and the time stored being the earlier one. If the tracking then applies a time cut between the hit SFD fiber and the VH time, one track is rejected. Figure 6.12 illustrates the problem: Both tracks from an accidental pair event hit the same fiber at times t_1 and t_2 , $t_1 < t_2$, but due to the open TDC gate of the SFD, only t_1 is recorded. If the tracking now requires a time cut between the VH and SFD X, i.e.

$$t_3 - t_1 < \text{tof (SFD} \rightarrow \text{VH}) \pm 3\sigma$$
 (6.32)

then particle 1 will be reconstructed, since

$$t_3 - t_1 < \text{tof (SFD} \rightarrow \text{VH}) \pm 3\sigma$$
 (6.33)

but particle 2 will not be reconstructed, because

$$t_4 - t_1 = t_4 - (t_2(th) - 10ns) = t_4 - t_2(th) + 10ns > \text{tof (SFD} \rightarrow \text{VH)} \pm 4ns$$
(6.34)

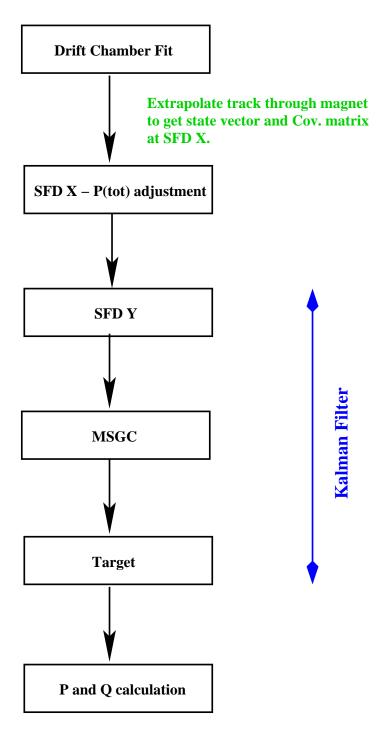


Figure 6.11: Flowchart of the BASEL tracking. The blue part corresponds to the part of the tracking where a Kalman filter was used.

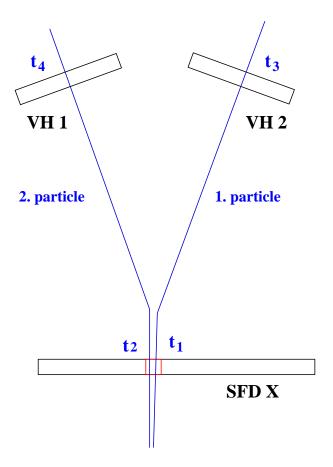


Figure 6.12: Time cut between VH and SFD in the BASEL tracking and its implication for accidentals.

where $t_2(th)$ is the time where particle 2 would have hit SFD X. As a consequence, there are no accidental events reconstructed with adjacent hit fibers in the SFD as is displayed in figure 6.13. This situation can be remedied if the track finding algorithm uses not only the VH time of the track itself, say t_3 for track 1, but also the VH time of the other track, t_4 . Since this procedure is included already to create an ambiguity for accidental events, no further corrections have to be applied.

The merging of the PSC is simulated in analogy to the detector simulation used for Monte Carlo data. The idea is to destroy for two track events which hit two adjacent SFD fiber with some probability one of the two SFD hits to match the measured hit fiber difference in the SFD. A detailed description of the method can be found in chapter 7.

The resulting SFD distributions for the corrected accidentals and for prompt events are displayed in figure 6.14. The Q of the plotted events was restricted to

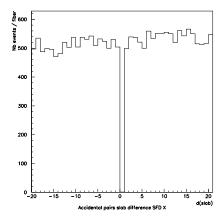


Figure 6.13: Difference of hit fibers chosen by the tracking for accidental pairs uncorrected. No Q_{trans} cut was applied.

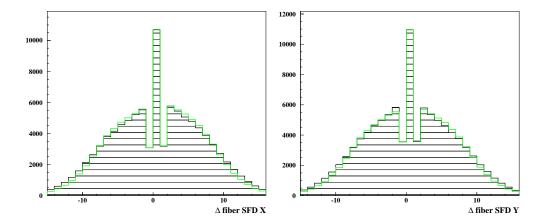


Figure 6.14: Difference of hit fibers chosen by the tracking for prompt (black) and corrected accidental events (red) for Ni 2001 data in the X (left) and Y layer (right) of the SFD. There was a cut applied on $Q_{trans} < 4 \text{ MeV/c}$.

 Q_{trans} <4 MeV/c and $|Q_l|$ < 15 MeV/c.

6.6 Further improvements

In addition to the here presented tracking algorithm, the Basel tracking makes use of a new SFD Y determination method which is described in detail in [68].

Chapter 7

Monte Carlo Software Package GEANT

This chapter describes the Monte Carlo Package GEANT which has been adapted to the DIRAC experiment in its version 2.61 [69]. The adaption of the GEANT software package was performed mainly by P. Zrelov and V. Yazkov. A user's guide can be found here [70]. The digitalization of the detectors and the simulation of noise is performed inside the offline software and was implemented mainly by A. Benelli. A user's guide to the detector simulation is available [71].

The DIRAC setup is completely simulated. Once the input distributions are defined, the program simulates the DIRAC spectrometer. In addition, the detectors and triggers are simulated as well. This allows to create artificial data which resembles the measured one very precisely.

The background determination due to accidental, non-Coulomb and Coulomb pairs is crucial for the extraction of the pionium signal. It also influences the normalization factor. In order to study the behavior of the setup with respect to atomic, Coulomb, non-Coulomb and accidental pairs, a dedicated $\pi^+\pi^-$ generator has been developed.

7.1 Generator

The Monte Carlo Package supports input files generated by FRITIOF [45] as well as input files from a dedicated $\pi^+\pi^-$ generator, which produces atomic, Coulomb, non-Coulomb and accidental pion pairs. The generator is explained in detailed here [30, 72].

As a pion pair is a two particle system, six degrees of freedom have to be determined to completely specify its state. Also the position of the center of mass has to be generated.

We have chosen our set of variables to be the $\pi^+\pi^-$ center of mass in the laboratory and the relative momentum polar coordinate (P,θ,ϕ) and (Q,θ',ϕ') , see figure 7.1. These have to be generated according to the corresponding distributions of atomic pairs, Coulomb pairs, non-Coulomb pairs or accidental pairs.

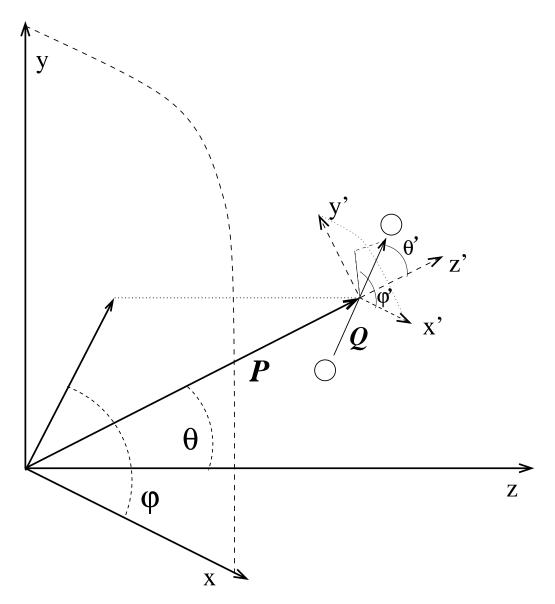


Figure 7.1: Q_{trans} and Q_{long} input distributions for Coulomb correlated pairs.

In general we have used experimental input for the laboratory Center of Mass momentum. The measured two dimensional spectra, as a function of P and θ^{-1} ,

¹The ϕ angle is considered to be independent.

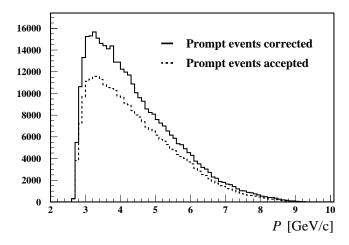


Figure 7.2: Total absolute momentum distribution P of the input (solid line) and after acceptance of the setup (dashed line) for time correlated (prompt) events. The dashed line coincides with the experimentally measured time correlated P spectrum.

have been divided by the spectrometer acceptance calculated with the help of the GEANT-DIRAC program for an initial (\vec{P}, θ) isotropic distribution with only geometric cuts. Figure 7.2 displays the momentum distribution for time correlated events (prompt events) of the input corrected for the acceptance. The dashed distribution shows the P spectrum after acceptance of the setup. It coincides with the experimentally measured (prompt) spectrum. The p spectrum of time uncorrelated pion pairs is obtained in the same manner.

7.1.1 Atomic pair generator

The P distribution of the atomic pairs follows the one of the Coulomb pairs (see below). Their Q distribution are generated using the spectra which are described in [27]. Figure 7.3 illustrates the Q_{long} and Q_{trans} distributions of atomic pairs after break-up. The asymmetry between the two components stems from the breakup process which is favors breakup from transversal photons.

7.1.2 Coulomb, non-Coulomb and accidental pair generator

Accidental and non-Coulomb pairs are produced isotropically in the center of mass system. This means that if we consider \vec{Q} , the Jacobian differential ele-

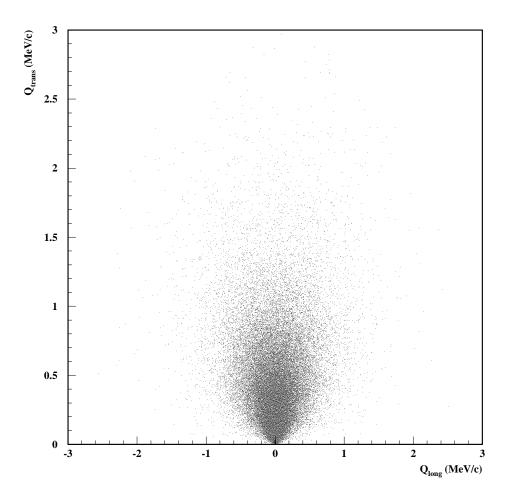


Figure 7.3: Q_{long} versus Q_{trans} for atomic pairs at breakup.

ment produces a $Q^2 sin(\theta')$ dependence. θ' is the angle between the total and the relative momenta see figure 7.1. For Coulomb pairs the Coulomb correlation has to be considered. This yields a $A_c(Q)Q^2 sin(\theta)$.

The total momentum spectra of the different pairs are obtained from the measured ones, taking into account the efficiency and the acceptance of the detector. The p spectrum of accidental pairs follows the measured one. The momentum spectrum of Coulomb and non-Coulomb pairs is extracted from the measured prompt spectrum. The measured prompt spectrum is split for this purpose into an uncorrelated accidental background and a mixture of long-lived and short lived sources. The relative abundances are obtained from FRITIOF.

The input distributions to the Monte Carlo are required to be smaller than

$$Q_{trans} < 7 \text{ MeV/c} \text{ and } |Q_{long}| < 18 \text{ MeV/c}$$
 (7.1)

These cuts are three standard deviations above the analysis cuts. To verify that these cuts do not distort the distributions after reconstruction, i.e. that the resulting distributions are independent on these input cuts, we use a special sample of Coulomb pairs with input cuts of $Q_{trans} < 10 \, \text{MeV/c}$ and $|Q_{long}| < 27 \, \text{MeV/c}$ and compare the reconstructed Q_{long} and Q_{trans} distributions from this sample to the ones using the smaller input cuts from equation 7.1. Figure 7.4 shows the acceptance of events from the subsample with tighter input cuts. We can see that below the analysis cut of $Q_{trans} < 4 \, \text{MeV/c}$ and $|Q_{long}| < 15 \, \text{MeV/c}$ the acceptance is unity within errors which allows to use the tighter subsample.

The error induced by the cuts is estimated by taking the sample with wider cuts ($|Q_l| < 27 \text{ MeV/c}$, $Q_{trans} < 10 \text{ MeV/c}$). This wider sample is split into two non-overlapping subsamples: The first one (sample A) corresponds to the one from equation 7.1, the second one is the complementary sample (B=all-A). The number of events within the analysis cuts ($|Q_l| < 15 \text{ MeV/c}$, $Q_{trans} < 4 \text{ MeV/c}$) coming from sample B is compared to the number of events coming from sample A. The resulting error (events from sample B / events from sample A) is 2×10^{-4} for Q_l and 1×10^{-4} for Q.

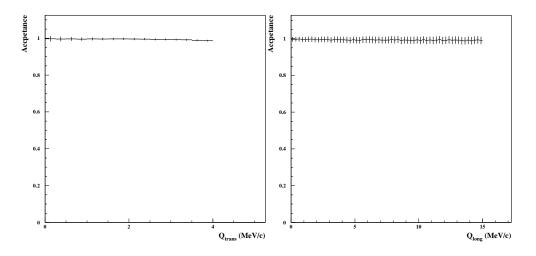


Figure 7.4: Acceptance of events from the subsample with tighter cuts. The left plot illustrates the acceptance in Q_{trans} , the right one in Q_{long} .

The input Q_{long} and Q_{trans} distributions with the input cuts from equation 7.1 for Coulomb and accidental pairs are shown in figure 7.5 and 7.6.

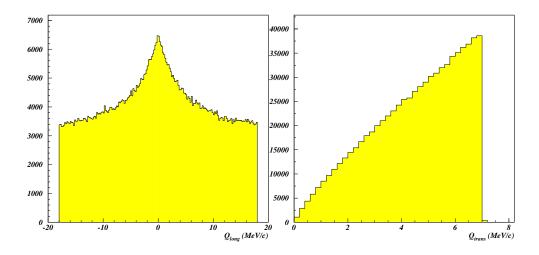


Figure 7.5: Q_{trans} and Q_{long} input distributions for Coulomb correlated pairs.

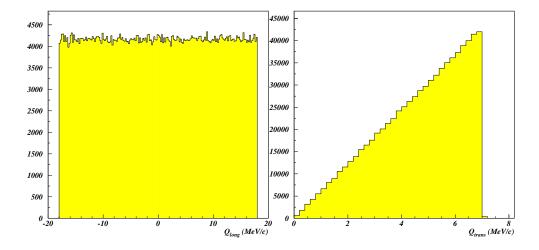


Figure 7.6: Q_{trans} and Q_{long} input distributions for non-Coulomb and accidental pairs.

7.2 Detector digitalization

The influence of the DIRAC apparatus has been simulated in a joint effort. A detailed manual can be found here [71]. In short the detector characteristics, namely the time resolution as well as specific inefficiencies have been simulated according to the experimental measurements. The author also participated in the effort and helped to develop the simulation for the vertical and horizontal hodoscopes [73]. The determination of the relative momentum depends crucially on the response

of the SFD detector A dedicated simulation of this detector has therefore been performed for each period separately.

7.2.1 SFD Simulation

The simulation of the SFD detector is crucial for the analysis because the determination of the relative momentum as well as the shape of the background in the very low Q region is defined by the SFD response. In addition, since we look for an enhancement of $\pi^+\pi^-$ pairs with very low Q values, the shape of the background in this region has to be modeled correct. The simulation has to consider three detector characteristics

- 1. The time resolution
- 2. The peak sensing circuit
- 3. The single track inefficiency incurred due to the chosen threshold value.

The time resolution of the SFD detector is determined from experimental data. As a first step minimum bias trigger data is used and events with only one drift chamber track in one arm are selected. In addition only events for which there is only one good hit fiber in each SFD plane are tagged for further processing. In a next step the time difference between the vertical hodoscopes and each SFD plane are calculated taking onto account the path length of the track. Figure 6.4 shows this time difference and the corresponding σ to be of the order of 1 [ns]. Clearly this measured uncertainty σ_{Meas} includes the uncertainty of the SFD plane as well as the one of the vertical hodoscopes,

$$\sigma_{Meas} = \sqrt{\sigma_{VH}^2 + \sigma_{SFD}^2}$$

The time resolution in the vertical hodoscopes is estimated to be σ_{VH} =0.12 [ns], see in chapter DIRAC apparatus.Because this is small compared to the measured one, we can approximate $\sigma_{SFD} = \sigma_{Meas}$ = 1.0 [ns]²³. The so obtained time resolution is used to jitter the time of each recorded SFD fiber hit in the Monte Carlo.

²Using the above equation and plugging in the values 1 and 0.12 for σ_{Meas} and σ_{VH} , we would obtain 0.99 ns for the resolution of the SFD.

³The difference between the calculated value of $\sigma_{SFD}=1$ ns and the one obtained as the difference between the two SFD planes ($\sigma_{SFD}=0.8$ ns) comes from time jitter in the trigger subsystem.

A peak sensing circuit (PSC) is installed in the SFD detector to remove noise and optical cross talk. It is explained in detail in [50] as well as in the chapter DIRAC apparatus. The result of this merging are inefficiencies in the SFD X (Y) plane for events with adjacent hits, which distorts the Q_x (Q_y) determination. In addition there is a threshold cut on the relative difference between adjacent columns. For consistency the Monte Carlo events have to be treated accordingly, which means simulating this algorithm. It is placed inside the offline code ARIANE and invoked before the tracking routines start. It removes with a certain probability one hit or two hits in the Monte Carlo data for an two adjacent fiber hit event.

The destruction probabilities are obtained from experimental data via a recursive method.

- 1. A Monte Carlo sample of atomic pairs is processed using the software merging algorithm with some destruction probability.
- 2. The difference of hit fibers per SFD plane of the experimental prompt spectrum as well as of the Monte Carlo sample of atomic pairs is calculated.
- 3. The difference of hit fibers per SFD plane of the experimental prompt spectrum is corrected (netted) for the atomic pairs it consists⁴. The resulting netted fiber difference distributions should contain only the influence of Coulomb pairs.
- 4. The inefficiency for events (=destruction probability) with a fiber difference of plus (minus) one is obtained from this netted fiber difference distribution by comparing the number of events in the bin with plus (minus) one with the number of events in the bin with a fiber difference of plus (minus) two. A schematic view is illustrated in figure 7.7.
- 5. If the destruction probability obtained in step 4 does not match the one used in step 1, steps 1 to 4 have to be repeated using the new destruction probabilities of step 4 until the probability in step 1 and step 4 are consistent.

Figure 7.7 shows schematically the slab difference for a SFD plane and how the destruction probability is defined. Most events which are merged, are not lost. They appear in the bin with zero slab difference in figure 7.7.

⁴This means that the SFD distribution of a given amount of atomic pairs is subtracted from the experimental SFD distribution to yield the Coulomb SFD distribution.

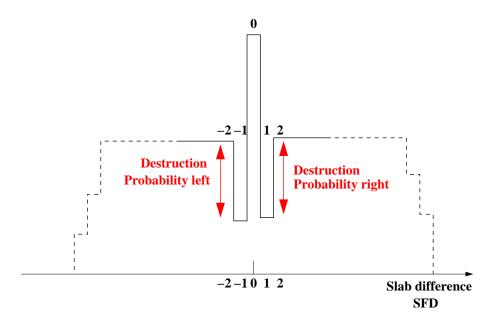


Figure 7.7: Schematic view of the hit fiber difference in a SFD plane. There is an inefficiency for events with a hit fiber difference of plus or minus one due to the peak sensing circuit. The destruction probability is defined as the difference between the number of events in the bin with plus (minus) one and with the number of events in the bin with a fiber difference of plus (minus) two.

The single track inefficiency takes into account the probability that the light output of a particle passing through a SFD fiber is below a given threshold. It is clear that the threshold has to be chosen to minimize electronic noise while still accept all relevant hits. The single track inefficiency was estimated by D. Goldin and L. Tauscher [51], F. Takeutchi [52] and V. Yazkov [74]. Goldin estimates the single track inefficiency for 2001 to be 5%, in accordance with the estimation of V. Yazkov. This value is used for the analysis presented in this document.

How well the SFD simulation compares to the measured data is investigated in detail in the following section.

7.2.2 VH and HH detectors

The simulation of the VH and HH was performed by the author and is described in [73].

7.3 Comparing Monte Carlo data to measured data

A crucial test of the Monte Carlo is the comparison with measured data. For this purpose we use the measured accidentals since their distribution is produced by one physics channel only as compared to the measured prompt events which are a mixture of different sources.

For this analysis we use the measured accidental and compare them to the Monte Carlo ones. The left plot in figure 7.8 shows the absolute momentum distribution for measured (red) and Monte Carlo accidentals (black) traveling through the negative arm. The corresponding ratio of Monte Carlo accidentals over mea-

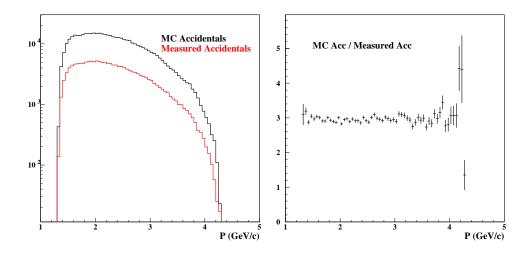


Figure 7.8: Comparison of the absolute momentum spectrum for measured (red) and Monte Carlo (black) accidentals is presented in the left plot (logarithmic scale). The corresponding ratio of Monte Carlo accidentals over measured accidentals is shown in the right plot.

sured accidentals is shown in the right plot. The ratio is flat which highlights the good agreement of the two p spectra. The ratio for the positive arm behaves correspondingly. If we look as a next step at the difference of the selected fiber candidates on the level of the SFD X and Y we see a similar picture. Figure 7.9 presents in the left plots the difference of selected fibers in the X and the Y layer of the SFD detector. The right plots show the corresponding ratios which are flat for the X as well as for the Y plane.

Finally we can also compare the Q distributions for measured and Monte Carlo accidentals. Figure 7.10 presents the Q_l and the Q_{trans} for measured (red) and Monte Carlo (black) accidentals in the left plot (logarithmic scale). The right plot displays the corresponding ratios. As before we can conclude that the Monte

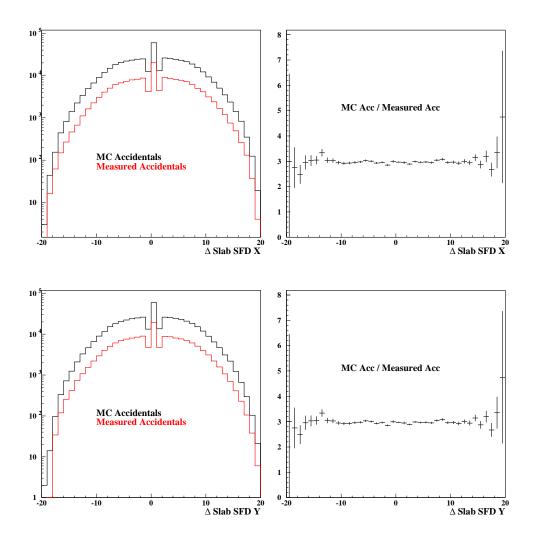


Figure 7.9: The comparison of the fiber difference at the level of SFD X(top) and Y(top) (bottom) for measured (red) and Monte Carlo (black) accidentals is presented in the left plot (logarithmic scale). The corresponding ratio of Monte Carlo accidentals over measured accidentals is shown in the right plot.

Carlo accidentals behave as the measured ones. This is very important since we will use Monte Carlo data for some background contributions in the later analysis.

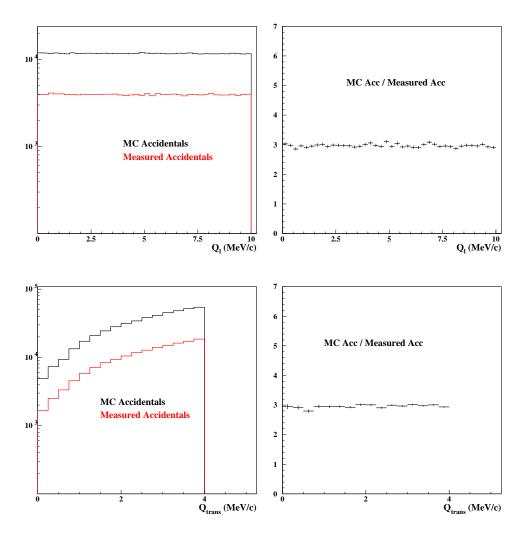


Figure 7.10: The comparison of the Q_l and the Q_{trans} for measured (red) and Monte Carlo (black) accidentals is presented in the left plot (logarithmic scale). The corresponding ratio of Monte Carlo accidentals over measured accidentals is shown in the right plot.

Chapter 8

Calibration Measurements and Resolution

The DIRAC experiment can be checked and calibrated using experimental data with two dedicated measurements: the use of the Λ decay into a proton and a negative pion and the detection of e^+e^- pairs. Furthermore the resolution of the setup and the off-line reconstruction algorithm can be examined using Monte Carlo data.

8.1 \wedge decay

The DIRAC spectrometer is able to capture some Λ decays into a proton and a negative pion:

$$\Lambda \to p + \pi^- \tag{8.1}$$

But due to the kinematics of this asymmetric decay the symmetric spectrometer can only capture events where the proton is reasonably fast. Hence a dedicated Λ trigger (see chapter 4) was implemented, which triggers only the innermost slab of the vertical hodoscopes on the positive arm, while accepting signals from all vertical hodoscopes slabs on the negative arm.

The reconstruction of the $p\pi^-$ invariant mass can be used to calibrate the spectrometer. For the nickel 2001 running period this was done and figure 8.1 shows the invariant mass of a proton and negative pion pair. The total momentum was restricted to be 4.7 GeV/c $< p_\Lambda <$ 6.5 GeV/c. The red line represents a Gaussian fit to the distribution with a mean value of 1115.6 MeV/ c^2 and a width of σ_Λ =0.54 MeV/c in agreement with the PDG [34].

Figure 8.1 further establishes the resolution for Q. The Λ mass in the center of mass system is equal to

$$m_{\Lambda}^2 = (E_p + E_{\pi})^2 = (\sqrt{m_p^2 + p^2} + \sqrt{m_{\pi}^2 + p^2})^2$$
 (8.2)

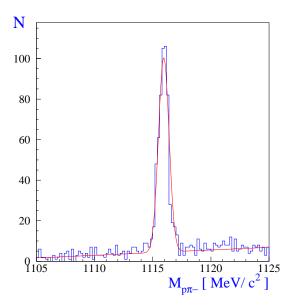


Figure 8.1: Mass distribution of $p\pi^-$ pairs from Λ decay at 4.7 < p_{Λ} < 6.5 GeV/c

The relative momentum Q on the other hand can be written as:

$$Q^2 = (E_p - E_\pi)^2 - 4p^2 (8.3)$$

Connecting the two equations and differentiating partially, one obtains:

$$dQ = \frac{m_{\Lambda}}{Q} \cdot dm_{\Lambda} \tag{8.4}$$

An estimated uncertainty in the Λ mass of σ_{Λ} =0.54 MeV/c, as shown in figure 8.1, translates therefore into an Q uncertainty of σ_{Q} =0.81 MeV/c.

8.2 Track reconstruction efficiency and resolution of atomic pairs

The reconstruction efficiency and resolution can be checked using Monte Carlo data. First we look at the efficiency for atomic pairs. In a second step we determine the resolution of the absolute and relative momenta. Since the track reconstruction efficiency and resolution function for atomic pairs using Monte Carlo has been studied previously [75], some of the results in this section are based on this previous study.

The track reconstruction efficiency and resolution can be estimated in the following way: A known sample of atomic pairs is processed through the Monte Carlo program. Then the detector and trigger simulations are run and the resulting events are processed with the offline tracking program. Since each event has a unique number, we can define for each event exactly the changes that occur during its virtual flight through the (GEANT) setup and the following reconstruction. Comparing the reconstructed Q's with the input ones leads to the efficiency, acceptance and resolution functions.

We use atomic pairs originating from $A_{2\pi}$ breakup as our input¹. Figure 8.2 shows the input distribution at production for the three momentum projections. These distributions exhibit a large part (around 70%) of the statistic at very low Q < 0.1 MeV/c, while the rest is found in a tail extending up to 2 MeV/c. Before traveling through the setup, the atomic pairs are scattered in the target, which widens (mostly) the Q_x and Q_y momentum distributions.

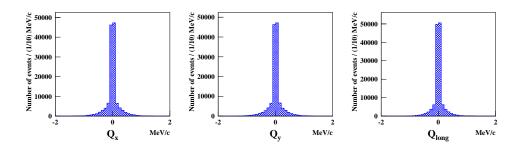


Figure 8.2: Relative momentum Q_x , Q_y and Q_l in [MeV/c] at production.

If we look in two dimension we can see the asymmetry between Q_{long} and Q_{trans} at breakup for the atomic pairs as illustrated in figure 7.3 When the atom travels through the target, it interacts with the electromagnetic field of the target nuclei by exchanging photons. Since the probability of this exchange depends on the distance between the atom and the nucleus, smaller distances are more likely which translates into a preferred breakup induced by transversal photons. As a result the atomic pairs transversal relative momentum component is wider than the longitudinal one.

The reconstruction efficiency for Monte Carlo atomic pairs is estimated to be around 62%, see table 8.1. The inefficiency in the reconstruction arises from the simulated detector responses and the cuts from the tracking algorithm.

To check the reconstruction algorithm we can compare the input distributions with the output ones. Figure 8.3 shows the input distribution (blue, fine filling) and

¹Th atomic pairs are produced by the generator explained in section 7.1 and in [72].

rable 8.1. Reconstruction efficiency for atomic pairs (Monte Carlo data).			
Nb. of Events	% total	% accepted	
75000	100.00	-	
45354	60.47	100.00	
28034	37.38	61.81	
	Nb. of Events 75000 45354	Nb. of Events % total 75000 100.00 45354 60.47	

Table 8.1: Reconstruction efficiency for atomic pairs (Monte Carlo data).

the reconstructed ones (black, coarse filling). We can then define the difference

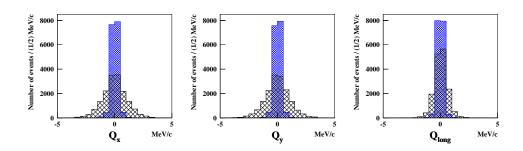


Figure 8.3: Relative momentum projections Q_x, Q_y and Q_{long} in [MeV/c] at the input (blue) and after reconstruction (black).

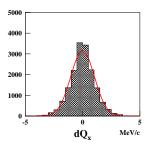
between the input Q and the reconstructed Q as the reconstruction resolution:

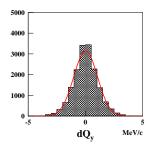
$$dQ = Q_{Input} - Q_{Rec} (8.5)$$

as is shown in figure 8.4 for Q_x , Q_y and Q_{long} . A Gauss function has been fitted to the distributions and yielded a mean and a standard deviation as described in table 8.2. From the fit we can see that the differences are centered at zero. The standard deviation for Q_x and Q_y is around 1 MeV/c, while the one of Q_{long} is around 0.5 MeV/c.

Table 8.2: The μ and σ in [MeV/c] of the difference in the Q_i , dQ_i between the GEANT input and the reconstructed value.

	μ	0
Q_x	$5.0 \cdot 10^{-3}$	1.03
Q_y	$9.5\cdot10^{-3}$	1.04
Q_{long}	$3.6 \cdot 10^{-2}$	0.52





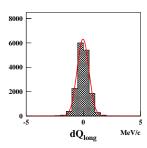


Figure 8.4: Difference dQ_i of the relative momentum projections Q_x, Q_y and Q_{long} in [MeV/c] between the input and the reconstruction.

The uncertainty in the reconstruction resolution is due to the multiple scattering in the target and not the reconstruction; the resolution of the tracking excluding the multiple scattering in the target have been studied [77] to be $\sigma=0.5~{\rm MeV/c}$ for Q_x,Q_y and Q_l .

Figure 8.5 shows the impact of the multiple scattering and the track reconstruction in a two-dimensional surface Q_{trans} vs Q_{long} . We can see (by comparing to figure 7.3) the effect of the multiple scattering (and to less degree the tracking) on the transversal component, while the longitudinal one is less affected.

Atomic pair spectrum at production The atomic pair spectrum at production is composed of breakup spectra from various atom states according to [76]. Specifically, the Q value of the peak for the spectrum of principal quantum number n_i scales as $\frac{1}{2n_i}$, while the peak amplitude is proportional to $\frac{1}{n_i^2}$ (see figure 8.6). The spectrum with the widest Q spectrum at breakup is hence coming from 1s state. The smallest possible Q spectrum originates from a very high n and can be approximated by setting Q=0 MeV/c for all atomic pairs at breakup. Figure 8.7 shows the reconstructed Q spectrum from the standard case (black) where breakup is considered from all states. The red distribution denotes breakup from 1s states only, while the green one comes from atomic pairs with Q=0 MeV/c at breakup. The difference between the three spectra is most pronounced at Q<2.5 MeV/c. When integrating over the signal (i.e. up to Q=4 MeV/c), the difference vanishes.

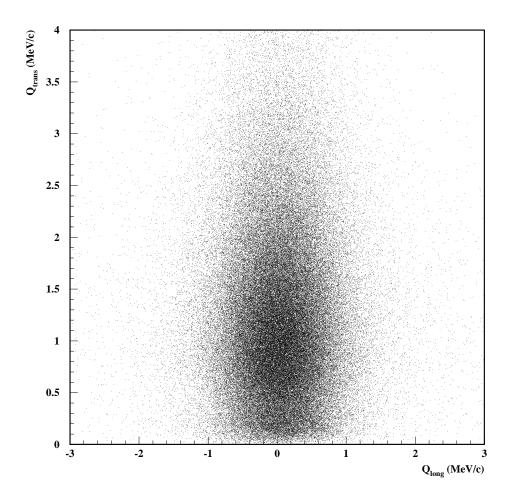


Figure 8.5: Q_{long} versus Q_{trans} for atomic pairs after multiple scattering the setup and reconstruction.

8.3 Track reconstruction efficiency and resolution of Coulomb and accidental pairs

We use simulated Coulomb and accidental pairs as our input. They are produced using a dedicated generator, which is described in short in the previous chapter (see section 7.1) and in length here [72]. The basic idea is to produce them according to their phase space. In addition, for Coulomb pairs the Coulomb correlation between the two pions at production is taking into account, which is strongest for very small Q values. The input distributions are also found in the previous

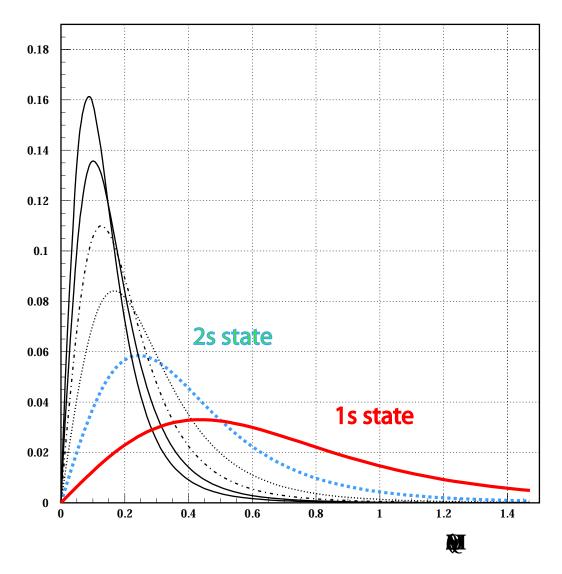


Figure 8.6: Q spectra at breakup for various s-states. The widest spectrum corresponds to the 1s state, while the spectra of higher principal quantum number are peaked at lower Q's.

chapter, section 7.1.

We can estimate the reconstruction efficiency by comparing the number of Coulomb and accidental input pairs and the number of reconstructed pairs. Table 8.3 shows the reconstruction efficiency in the DIRAC apparatus to be 64.5% for both pairs. A comparison with atomic pairs reveals a higher reconstruction efficiency for Coulomb pairs as well as for accidental pairs. The lower efficiency of atomic pairs can be attributed to the merging algorithm of the PSC.

The reconstruction efficiency is checked by calculating the difference between

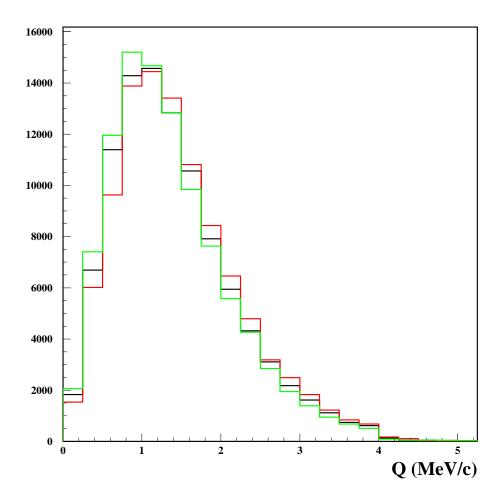


Figure 8.7: Reconstructed atomic pair spectrum after reconstruction which originate from breakup from all states (black) or from 1s (red). The green spectrum originates from atomic pairs with $Q=0~{\rm MeV/c}$ at breakup. A cut on $Q_{trans}<4~{\rm MeV/c}$ is applied.

the input and the reconstructed Q

$$dQ = Q_{Input} - Q_{Rec} (8.6)$$

Figure 8.8 (8.9) shows the Q distributions for the input (black) and the reconstruction (blue) for Coulomb (accidental) pairs. The input and reconstructed events were required to be within ($Q_{trans} < 4 \text{ MeV/c}$ and $|Q_{long}| < 15 \text{ MeV/c}$).

The enhancement for small Q_x and Q_y values stems from the merging of the peak sensing circuit in the SFD detector as well as the single track inefficiency in the same detector.

Level	Nb. of Events	% total	% accepted
~			
Coulomb pairs			
Input	75000	100.00	-
Accepted by DIRAC apparatus	42644	56.86	100.00
(Acceptance and trigger)			
After tracking	27493	36.66	64.47
Accidental pairs			
Input	75000	100.00	-
Accepted by DIRAC apparatus	42420	56.56	100.00
(Acceptance and trigger)			
After tracking	27435	36.58	64.67

Table 8.3: Reconstruction efficiency for Coulomb and accidental pairs.

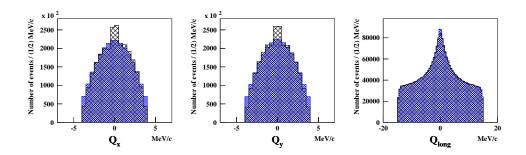


Figure 8.8: Relative momentum projections Q_x, Q_y and Q_{long} in [MeV/c] at the input (blue, fine) and after reconstruction (black, coarse) for Coulomb pairs.

We first calculate the difference in the reconstructed Q with respect to the input Q as indicated in equation 8.6. The result for the three Q projections from Coulomb (accidental) pairs are shown in figure 8.10 (8.11). A Gauss fit has been applied to the distributions to yield a mean (μ) and a standard deviation (σ) as reported in table 8.4 (8.5). The results are similar to the ones obtained for the atomic pairs.

The tails in Q_x and Q_y are due to the SFD single track inefficiency. This we can see by noting that the difference of the absolute Q_x and Q_y values from equation ?? exhibit a tail on the right side, as displayed in figure 8.12 for Coulomb pairs. A tail on the right side implies a higher value for the input than for the reconstruction which can be explained by losing one hit fiber due to an inefficiency.

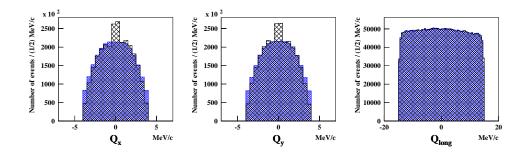


Figure 8.9: Relative momentum projections Q_x, Q_y and Q_{long} in [MeV/c] at the input (blue, fine) and after reconstruction (black, coarse) for accidental pairs.

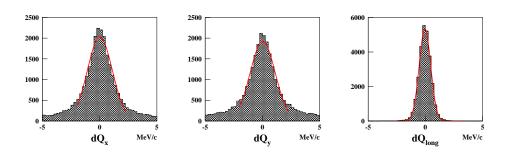


Figure 8.10: Difference dQ_i of the relative momentum projections Q_x, Q_y and Q_{long} in [MeV/c] between the input and the reconstruction for Coulomb pairs.

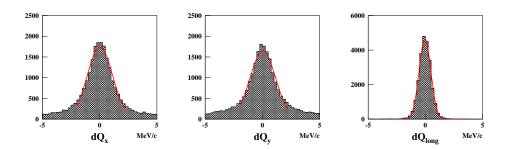


Figure 8.11: Difference dQ_i of the relative momentum projections Q_x, Q_y and Q_{long} in [MeV/c] between the input and the reconstruction for accidental pairs.

If for example an event has a positive Q_x of 4 MeV/c, then two (close-lying) SFD fibers are hit. Due to the inefficiency one hit is not recorded. Subsequently the tracking sees only one hit, which makes the reconstructed Q_x close to zero.

Table 8.4: The μ and σ in [MeV/c] of the difference in the Q_i , dQ_i between the GEANT input and the reconstructed value for Coulomb pairs.

	μ	σ
Q_x	$2.0 \cdot 10^{-2}$	1.09
Q_y	$1.6 \cdot 10^{-2}$	1.09
Q_{long}	$3.3 \cdot 10^{-2}$	0.50

Table 8.5: The μ and σ in [MeV/c] of the difference in the Q_i , dQ_i between the GEANT input and the reconstructed value for accidental pairs.

	μ	σ
Q_x	$1.4 \cdot 10^{-2}$	1.10
Q_y	$2.6\cdot10^{-2}$	1.11
Q_{long}	$3.1\cdot10^{-2}$	0.51

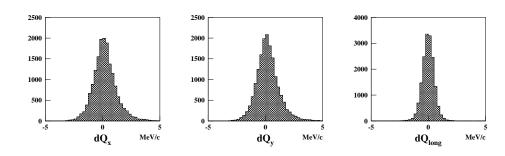


Figure 8.12: Difference of absolute dQ_i of the relative momentum projections Q_x, Q_y and Q_{long} in [MeV/c] between the absolute values of the input and the reconstruction for Coulomb pairs.

Figure 8.13 shows the effect of the tracking on Q_x . We can see a diagonal from the lower left to the upper right representing a correct hit assignment in the SFD X. The less pronounced diagonal from upper left to lower right originates from a false hit assignment. The vertical line in the middle of the plot comes from the single track inefficiency. If we split the events into correct or false hit assignment groups we can estimate their resolution due to tracking and multiple scattering separately. For Q_x we obtain from a Gauss fit a $\sigma_{Q_x}=1.05~{\rm MeV/c}$ for

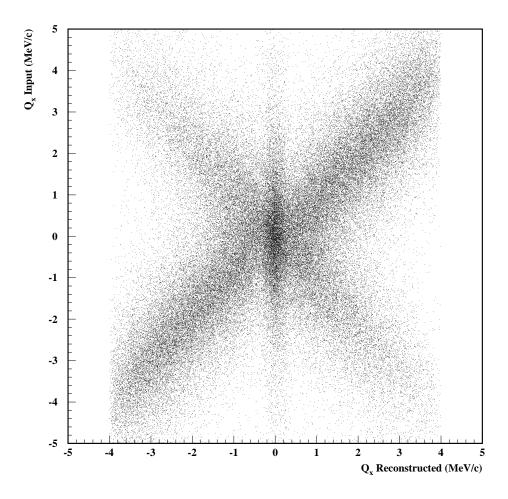


Figure 8.13: Q_x input versus Q_x reconstructed for Coulomb pairs. A cut on the reconstructed value of $|Q_x^{Rec}| < 4 \text{ MeV/c}$ was applied. Events with one or two time and space correlated hits per SFD plane were selected.

events with correct hit assignment and $\sigma_{Q_x} = 1.30 \, \text{MeV/c}$ for events with false hit assignment. If we take into account that a wrong hit assignment changes the sign of Q_x , we obtain $\sigma_{Q_x} = 1.1$ MeV/c also for events with a false hit assignment. The events in the vertical line produce an uncertainty of $\sigma_{Q_x}=1.17$ MeV/c. The numbers for Q_y are analogous.

Chapter 9

Experimental k-factor

The theoretical k-factor (k^{th}) from equation 2.28 relates the number of produced atoms to the number of produced Coulomb pairs at production. It is the normalization used to relate the number of observed atomic pairs to the number of produced atoms. But measuring the number of Coulomb and atomic pairs with DIRAC influences this normalization because of multiple scattering in the target and in the setup, after geometrical acceptance, trigger, detector and tracking inefficiencies. We have therefore to correct it and determine the experimental value of the k-factor (k^{exp}) , which is different from the theoretical one. This chapter explains how to obtain the experimental k-factor using Monte Carlo.

9.1 Calculation

The theoretical k-factor (k^{th}) from equation 2.28 relates the number of produced atoms (N_i^A) to the number of produced Coulomb pairs with Q less than 2 MeV/c $(N^{Coul}(Q < 2 \text{ MeV/c}))$ at production. The experimental value of the k-factor (k^{exp}) is different from the theoretical one because of multiple scattering in the target and in the setup, because of geometrical acceptance, trigger, detector and tracking inefficiencies. We define the breakup probability P_{br} as the number of broken up atoms (n_i^A) to the number of produced atoms (N_i^A) . The latter can be replaced with the number of produced Coulomb pairs multiplied with the k-factor. As a result we can write:

$$P_{br} = \frac{n_i^A}{N_i^A} = \frac{n_i^A}{k^{th} \cdot N^{Coul}(Q^{initial} < 2)}$$
(9.1)

 n_i^A, N_i^A and N^{Coul} are defined at production (the subscript i stands for 'initial'). The Coulomb pairs considered have an initial Q of less than 2 MeV/c which corresponds to the Q range of the atomic pairs. By considering Coulomb pairs only

for Q less than 2 MeV/c we make sure that the reconstruction efficiency is comparable for atomic and Coulomb pairs.

The measurement on the other hand yields the number of reconstructed atomic $(n^A(Q^{rec} < Q^{cut}))$ and Coulomb pairs $(N^{Coul}(Q^{rec} < Q^{cut}))$ below a certain Q^{cut} . We can relate these measured values to the ones at production in the following way

$$\frac{n_i^A}{k^{th} \cdot N^{Coul}(Q^{init} < 2)} \stackrel{!}{=} \frac{n^A(Q^{rec} < Q^{cut})}{k^{exp} \cdot N^{Coul}(Q^{rec} < Q^{cut})}$$
(9.2)

to yield an equation for the the experimental k-factor, k^{exp} as a function of the relative (cut) momentum Q^{cut} :

$$k^{exp}(Q^{cut}) = k^{th} \frac{n^A(Q^{rec} < Q^{cut})}{n_i^A} \frac{N^{Coul}(Q^{init} < 2)}{N^{Coul}(Q^{rec} < Q^{cut})}$$
(9.3)

The same methodology can also be applied to Q_l to yield:

$$k^{exp}(Q_l^{cut}) = k^{th} \frac{n^A(Q_l^{rec} < Q^{cut})}{n_i^A} \frac{N^{Coul}(Q^{init} < 2)}{N^{Coul}(Q_l^{rec} < Q^{cut})}$$
(9.4)

The above equations 9.3 and 9.4 show that the experimental k-factor can be regarded as the theoretical one after taking into account the reconstruction probabilities for Coulomb and atomic pairs. To illustrate this, consider for example equation 9.4. We can define the probability of reconstructing an atomic pair below a given cut as:

$$\frac{n^A(Q_l^{rec} < Q^{cut})}{n_i^A} = P_A(Q^{cut}) \tag{9.5}$$

In analogy we can define the probability of reconstructing a Coulomb pair below a given cut from an initial sample of $Q^{init} < 2 \text{ MeV/c}$ as

$$\frac{N^{Coul}(Q_l^{rec} < Q^{cut})}{N^{Coul}(Q^{init} < 2)} = P_{Coul}(Q^{cut})$$
(9.6)

The experimental k-factor from equation 9.4 becomes then

$$k^{exp}(Q^{cut}) = k^{th} \frac{P_A(Q^{cut})}{P_{Coul}(Q^{cut})}$$

In short we can calculate the breakup probability from the measured Coulomb and atomic pairs according to the following equation 9.7

$$P_{br} = \frac{n^A(Q^{rec} < Q^{cut})}{k^{exp} \cdot N^{Coul}(Q^{rec} < Q^{cut})}$$

$$(9.7)$$

9.2 Results for Nickel 2001

For the Nickel 2001 data we evaluate k^{exp} for two target thicknesses: 94 and 98 μ m. We require the events to pass a time correlation in the two arms of the vertical hodoscopes of $|dt_{VH}| < 0.5$ ns. In addition we accept only events with a maximum of two good hits per SFD plane (to remove hit assignment ambiguity, hence suppressing background) and low Q's:

$$|Q_{trans}| < 4 \text{ MeV/c} \text{ and } |Q_{long}| < 15 \text{ MeV/c}$$
 (9.8)

9.2.1 94 μ **m** target

Table 9.1 shows the result for the 94 μ m target case. The experimental k-factors are calculated using a Monte Carlo sample of 15 Mio events for Coulomb pairs and 600 thousand events for atomic pairs. The size of the sample explains the very small statistical error on the resulting values. The errors have been calculated using binomial error theory².

Table 9.1: Detected Coulomb and atomic pairs for the 94 μ m target for reconstructed Q and Q_l after setup acceptance, trigger and reconstruction efficiencies, time and analysis cuts. Using equation 9.3 and the known input factors n_i^A = 599267 and $N^{Coul}(Q^{init} < 2)$ = 315568, the experimental k-factor can be calculated in dependence on the reconstructed relative momentum.

e momentum.	n^A	N^{Coul}	k^{exp}
Total produced	599267	14892663	
Produced with	594799	315568	
$Q^{init} < 2~{ m MeV/c}$			
$Q^{Rec} < 2 \text{ MeV/c}$	105451±124	61694±16	0.5535 ± 0.0007
$Q^{Rec} < 3 \text{ MeV/c}$	125913 ± 145	158948 ± 41	0.2565 ± 0.0003
$Q^{Rec} < 4 \ \mathrm{MeV/c}$	131300 ± 150	307297 ± 79	0.1384 ± 0.0002
$Q_l^{Rec} < 1 \text{ MeV/c}$	120872 ± 140	128173 ± 33	0.3054 ± 0.0004
$Q_l^{Rec} < 2 \text{ MeV/c}$	130217 ± 149	237736 ± 61	0.1774 ± 0.0002

¹The definition of good hits in the SFD can be found in [63]. Stated simply, we require the hit fibers to be time correlated with the reconstructed track in the drift chambers as well as within a geometrical tracking window.

²We assume a binomial distribution. The Variance is then given by $V(r) = E(r^2) - (E(r))^2 = n(n-1)p^2 + np - (np)^2 = np(1-p)$ where n denotes number of trials and p the probability of a success. More details can be found in [78].

9.2.2 98 μ **m** Target

Table 9.2 shows the result for the 98 μ m target case. The results for the experimental k-factor differ slightly from the ones for the 94 μ m target. The reason for this difference can be attributed to a different SFD response and a slightly bigger multiple scattering than in the 98 μ m case.

Table 9.2: Detected Coulomb and atomic pairs for the 98 μ m target for reconstructed Q and Q_l after setup acceptance, trigger and reconstruction efficiencies, time and analysis cuts. Using equation 9.3 and the known input factors $n_i^A = 599252$ and $N^{Coul}(Q^{init} < 2) = 316481$, the experimental k-factor can be calculated in dependence on the reconstructed relative momentum.

	n^A	N^{Coul}	k^{exp}
Total produced	599252	14947054	
Produced with	594711	316481	
$Q^{init} < 2 \text{ MeV/c}$			
$Q^{Rec} < 2 \text{ MeV/c}$	102005 ± 120	60483 ± 16	0.5478 ± 0.0007
$Q^{Rec} < 3 \mathrm{MeV/c}$	122853 ± 142	156118 ± 40	0.2556 ± 0.0003
$Q^{Rec} < 4~{ m MeV/c}$	128286 ± 147	301222 ± 77	0.1383 ± 0.0002
$Q_l^{Rec} < 1 \text{ MeV/c}$	117731±137	125627 ± 32	0.3044 ± 0.0003
$Q_l^{Rec} < 2 \mathrm{MeV/c}$	127242 ± 146	232647 ± 60	0.1776 ± 0.0002

9.3 Systematic influences

The evaluation of the experimental k-factor should also consider systematic influences. In this section we examine how a change of the multiple scattering of 5% influences the experimental k-factors.

In order to study this effect, we increase (decrease) the multiple scattering angle calculated by GEANT by 5%. Then we redo the above explained analysis. Because the statistical errors are very small³ a systematic influence can become easily dominant.

First we can compare the influence of changing the multiple scattering on the background. For this study we use the reconstruction probabilities for Coulomb, $P_{CC}(Q^{cut})$, and for atomic pairs, $P_A(Q^{cut})$, as defined above in equation 9.5 and 9.6 and calculate the relative changes of these probabilities due to a change in the

³Especially as compared to the error of the DIRAC measurement, which is of the order of 5%.

multiple scattering:

$$\Delta P_{j}(Q^{cut}) = \frac{P_{j}(Q^{cut})|_{\mathbf{MS} \pm 5\%} - P_{j}(Q^{cut})|_{\mathbf{standard\ MS}}}{P_{j}(Q^{cut})|_{\mathbf{standard\ MS}}} \quad j = A, CC \quad (9.9)$$

Figure 9.1 illustrates the changes to the background for both Coulomb and atomic pairs (in percent). The atomic pairs are more affected by a change in the multiple scattering than the Coulomb pairs, especially for low Q values. The

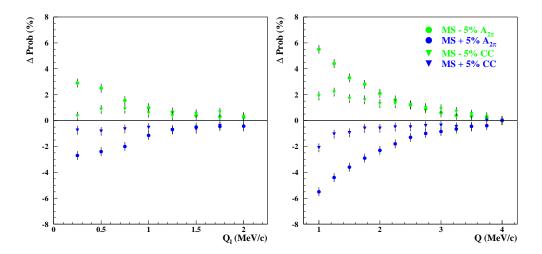


Figure 9.1: Change in the background reconstruction probability $\Delta P_j(Q^{cut})$ in Q_l , Q_l for Coulomb and atomic pairs as defined in equation 9.9 for increasing and decreasing the multiple scattering by 5%.

Coulomb pair background is mostly affected for small Q < 1.5 MeV/c. The atomic pair on the other hand change their shape in the total Q spectrum up to 4 MeV/c. The effect becomes very dominant for Q < 2 MeV/c. It is more pronounced in Q than in Q_l . We expect these changes (especially the atomic pairs) to influence the experimental k-factor.

Table 9.3 (9.4) displays the results obtained for the 94 μ m target increasing (decreasing) the multiple scattering angle by 5%. We notice that increasing (or decreasing) the multiple scattering of 5% introduces a negliable effect for $Q^{Rec} < 4$ MeV/c and $Q_l^{Rec} < 2$ MeV/c, while an important change is found for smaller cut, i.e. $Q^{Rec} < 2$ MeV/c and $Q_l^{Rec} < 1$ MeV/c. Since the pionic atom signal extends up to 4 MeV in Q and up to 2 MeV in Q_l , we have to take this source of systematic error into account when cutting into the signal.

We can define an error on the experimental k-factor by calculating the percentage difference in the k-factor value of the standard and the increased (decreased)

Table 9.3: Detected Coulomb and atomic pairs for the 94 μm target after **increasing** the multiple scattering angle by 5%. The table shows the resulting values for reconstructed Q and Q_l after setup acceptance, trigger and reconstruction efficiencies, time and analysis cuts. Using equation 9.3 and the known input factors $n_A^i = 599237$ and $N_{Coul}(Q^{init} < 2) = 203206$, the experimental k-factor can be calculated in dependence on the reconstructed relative momentum.

	n_A	N_{Coul}	k^{exp}
Total produced	599237	9592560	
Produced with	594783	203206	
$Q^{init} < 2~{ m MeV/c}$			
$Q^{Rec} < 2 \text{ MeV/c}$	103267 ± 122	39979±13	0.5387 ± 0.0007
$Q^{Rec} < 3 \mathrm{MeV/c}$	125821 ± 145	103030 ± 33	0.2547 ± 0.0003
$Q^{Rec} < 4 \text{ MeV/c}$	132064 ± 151	199359 ± 64	0.1382 ± 0.0002
$Q_l^{Rec} < 1 \text{ MeV/c}$	120577 ± 140	83079 ± 27	0.3027 ± 0.0004
$Q_l^{Rec} < 2 \mathrm{MeV/c}$	130911 ± 150	154088 ± 49	0.1772 ± 0.0002

Table 9.4: Detected Coulomb and atomic pairs for the 94 μ m target after **decreasing** the multiple scattering angle by 5%. The table shows the resulting values for reconstructed Q and Q_l after setup acceptance, trigger and reconstruction efficiencies, time and analysis cuts. Using equation 9.3 and the known input factors n_A^i = 599234 and $N_{Coul}(Q^{init} < 2)$ = 276758, the experimental k-factor can be calculated in dependence on the reconstructed relative momentum.

	n_A	N_{Coul}	k^{exp}
Total produced	599234	13038438	
Produced with	594917	276758	
$Q^{init} < 2~{ m MeV/c}$			
$Q^{Rec} < 2 \text{ MeV/c}$	109365±128	55666±15	0.5580 ± 0.0007
$Q^{Rec} < 3 \mathrm{MeV/c}$	128217 ± 147	142574 ± 39	0.2554 ± 0.0003
$Q^{Rec} < 4 \text{ MeV/c}$	132918 ± 152	273715 ± 75	0.1379 ± 0.0002
$Q_l^{Rec} < 1 \text{ MeV/c}$	123243±140	114473 ± 32	0.3058 ± 0.0004
$Q_l^{Rec} < 2 \text{ MeV/c}$	131806 ± 150	211720 ± 58	0.1768 ± 0.0002

multiple scattering (MS):

$$\Delta k^{exp} = \frac{k^{exp}(MS \pm 5\%) - k^{exp}(\text{standard MS})}{k^{exp}(\text{standard MS})}$$
(9.10)

The resulting k factors and errors are illustrated for Q (upper plots) and Q_l (lower plots) in figure 9.2 as the blue triangles (green rectangles) for 5% bigger (smaller) multiple scattering. The relative difference is plotted in percent and as a function of the cut momentum in Q and Q_l . The statistical uncertainties of the calculated experimental k-factor value for standard multiple scattering are drawn as a magenta band.

The figures illustrate how much the low $Q(Q_l)$ region is affected by a change in multiple scattering. If we apply a strong cut on Q (i.e. Q < 1.5 MeV/c) to extract the signal, we induce an uncertainty in the k-factor which can become comparable to the expected measurement uncertainty in the experimental data (which is around 5%). In contrast, if we accept most of the pionium signal (which extends up to 4 MeV/c), the error induced due to the multiple scattering is comparable to the statistical uncertainty and about two orders of magnitude smaller than the error arising from the measurement. The asymmetric behavior of Δk^{exp} for increasing versus decreasing the multiple scattering is not caused by a different normalization (since we divide in equation 9.10 for bigger and smaller multiple scattering alike by the same value), but by the sensitivity of the Coulomb pairs to the multiple scattering change for very small Q's. Decreasing the multiple scattering by 5% increases the amount of Coulomb pairs for small Q's more than their amount is decreased by increasing the multiple scattering. On the other hand, the effect of increasing versus decreasing the multiple scattering is symmetric for atomic pairs, which explains the observed asymmetry in Δk^{exp} .

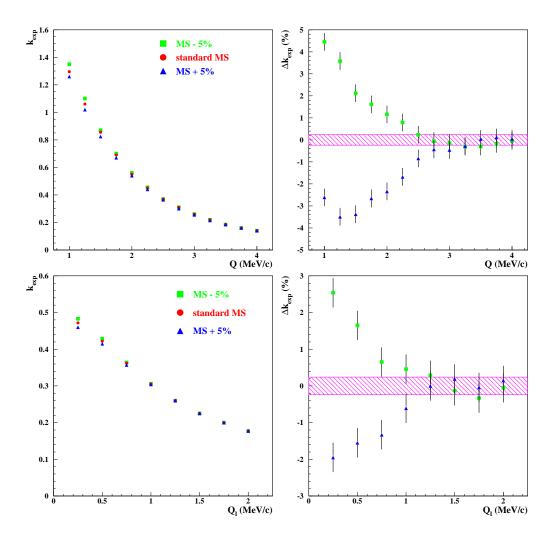


Figure 9.2: The upper left plot shows the k-factor for standard (red circles), 5% bigger (blue triangles) and 5% smaller (green rectangles) multiple scattering for Q. The relative change for bigger (and smaller) multiple scattering with respect to the standard case (in percent) is drawn in the right upper plot. The magenta band illustrates the error due to statistical uncertainty of the k-factor. The lower two plots show the k-factor (left) and the relative change for Q_l .

Chapter 10

Atomic pair detection and breakup probability determination

This chapter explains the extraction of the atomic pair signal and the determination of the corresponding breakup probability. In short we extract the atomic pairs from a measured spectrum of time correlated events by subtracting all background sources and determine the breakup probability by relating the number of measured Coulomb pairs to the number of measured atomic pairs using the experimental k-factor from the previous chapter. The lifetime can be calculated in the last step from the breakup probability.

The last part in the chapter discusses constraint fits and systematic effects.

10.1 Variables

From the discussion of the pionium, we notice that the binding energy of the atom and hence the initial relative momentum distribution of the atomic pairs is very small, which poses a serious challenge to any experiment to measure such small energy differences. The DIRAC experiment has chosen to exploit this special property of the atomic pairs by looking for excess $\pi^+\pi^-$ pairs with very small relative momentum Q.

While traveling through the target, the atomic pairs are distorted by multiple scattering which deteriorates the transversal component of Q while leaving the longitudinal component nearly untouched. As a result, the atomic pair spectrum after the target is much wider in Q_{trans} than in Q_{long} . Accordingly, the resolution after the target (and hence after reconstruction) in Q_{long} is much better than in Q_{trans} .

Monte Carlo data for atomic pairs confirms this pattern. Figure 8.3 in chapter 9 illustrates the input Q_{long} and Q_x and Q_y together with the reconstructed value.

The difference between input and reconstructed value is plotted in figure 8.4. Table 8.2 displays the mean and standard deviation of a fit assuming a Gaussian shape to this difference. We can clearly see from the table that the effect of multiple scattering deteriorates the transversal components much more ($\sigma_{Q_x,Q_y} \approx 1 \text{ MeV/c}$) than the longitudinal one ($\sigma_{Q_{long}} \approx 0.5 \text{ MeV/c}$).

As a consequence, if we apply a soft Q_{trans} cut to include the full atomic pairs spectrum (i.e. $Q_{trans} < 4 \text{ MeV/c}$) and look in Q_l , we are not very sensitive on the multiple scattering which suggest to use just this configuration for the analysis. In addition, if we also use the total relative momentum Q for the analysis, we can compare the results obtained from Q_l with the ones obtained from Q. The better both agree, the better is our background simulated. On the other hand, using Q we can better estimate the accuracy of the multiple scattering description in the Monte Carlo by comparing data and simulation.

As a summary we can conclude that the difference in Q_l with a soft Q_{trans} cut, and Q gives us an estimate of systematics in the background construction, while differences in simulation and data in Q are mainly induced by multiple scattering description.

10.2 Description of the method

This section is intended to give an overview of the analysis method. The details on each step are found in the remainder of this chapter. The extraction of the atomic pairs, the determination of the breakup probability and the lifetime is performed in multiple steps.

First, the measured data sample is restricted to time-correlated events with a small relative momentum Q. Q is split into its longitudinal (Q_{long}) and transversal (Q_{trans}) components. Because the fast triggers preselect events with very small transversal Q, the restriction on Q_{trans} is already strong. In order to adjust the various background sources to the measured spectrum, we need a big enough data sample. Hence we accept higher Q_{long} values. This makes the cut on Q_{long} loser than on Q_{trans} .

The measured time-correlated spectrum consists of atomic, Coulomb, non-Coulomb and accidental pairs. In the second step we remove the accidental pairs from the time-correlated events by subtracting them. The accidental pair spectrum is measured in parallel. The amount of accidental pairs to subtract is determined using the time difference at the level of the vertical hodoscopes. The remaining events are called real pairs.

The two remaining physics channels besides the signal in the measured real pairs are simulated using Monte Carlo. In the third step we fit their relative momentum distributions simultaneously to the measurement above the signal region.

These background contributions are then extrapolated in the signal region.

The atomic pairs can be extracted in the fourth step by subtracting the Coulomb and non-Coulomb background from the measured \mathcal{Q} spectrum. Also the amount of Coulomb and non-Coulomb pairs in the signal region can be extracted at this step.

The breakup probability which is defined as the number of broken up atoms to the number of produced ones can now be calculated from the amount of extracted atomic and Coulomb pairs, taking into account the normalization and the acceptance and efficiency of the setup. The acceptance and efficiency of the setup is determined using Monte Carlo and is used to evaluate the acceptance and efficiency corrected normalization with high precision. The breakup probability determination is nearly independent on Q due to the cancellation of systematic effects by using the efficiency and acceptance corrected normalization.

Lastly, we calculate the lifetime of $A_{2\pi}$ from the breakup probability.

10.3 Event selection

This analysis is based on the data sample which was recorded with a nickel target in 2001. The first part of the sample uses a $94\mu m$ target, the second part a 98μ target thickness. The trigger during the measurement was $T1*\pi\pi*Copl*DNA*T4$. We use the BASEL tracking (see chapter 6) and the BASEL SFD Y determination [68] for both measured data and Monte Carlo data.

The event selection has two stages. The preselection restricts the measured data to events with

- $\pi^+\pi^-$ signature (removal of muons and electrons).
- One (and only one) fitted and reconstructed drift chamber track per arm.
- a maximum of four time and space correlated hits per SFD plane and an overall of six correlated hit fibers in both SFD planes.
- $|Q_x| < 6 \text{ MeV/c}$, $|Q_y| < 6 \text{ MeV/c}$ and $|Q_{long}| < 45 \text{ MeV/c}$.
- P < 4 GeV/c for positive particles (to remove time-correlated protons).

The preselection reduces the number of accepted $\pi^+\pi^-$ events from 681 Million to 40 Mio (30 Mio for the 94 μ m target and 10 Mio for the 98 μ m target).

For the final analysis further cuts are applied:

 Time correlation as measured by the vertical hodoscopes allows to split the events into

- 1. **Time correlated** events are defined to arrive within 0.5 ns at the level of VH. These events are henceforth called **prompt event**.
- 2. **Time uncorrelated** events have a time difference at the VH of -15 ns $< dt_{VH} <$ 5 ns. They are called **accidental events**. The choice of the accidental region ranging from -15 ns < dt < to -5 ns is motivated by the fact that there are no time correlated protons in this interval and that at time differences greater than 5 ns the SFD readout has no merging.
- Only events with at most two time- and space correlated events per SFD plane are accepted. This provides the cleanest possible event pattern.
- The unique characteristic of the atomic pairs are exploited to select the signal region: $Q_{trans} < 4 \text{ MeV/c}$ and $|Q_{long}| < 15 \text{ MeV/c}$. These specific cuts have been chosen to include the total signal without being biased by the trigger (as for Q_{trans}) as well as having a range to fit the background (as for Q_l).

The final analysis cuts leaves 358251 prompt events for the $94\mu m$ target, 83357 prompt events for the $98\mu m$ target and 236011 accidental events for the $94\mu m$ target and 52424 accidental events for the $98\mu m$ target. The time difference distribution as measured by the vertical hodoscopes after the above selection criteria is shown in figure 10.1.

10.4 Background description

The measured prompt spectrum incorporates besides atomic pairs also accidental, non-Coulomb and Coulomb pairs. The accidental and non-Coulomb are created isotropically, while the Coulomb pairs are in addition Coulomb correlated. In general we can write the measured prompt spectrum as a sum of four different contributions:

$$\frac{dN^{Meas}}{dQ} = \underbrace{\alpha \cdot \frac{dN^{A_{2\pi}}}{dQ}}_{Atomic-pairs} + \underbrace{\beta \cdot \frac{dN^{Coul}}{dQ}}_{Coulomb} + \underbrace{\gamma \cdot \frac{dN^{NC}}{dQ}}_{non-Coulomb} + \underbrace{\delta \cdot \frac{dN^{Acc}}{dQ}}_{Accidentals}$$
(10.1)

where α , β , γ and δ represent the relative share of atomic, Coulomb, non-Coulomb and accidental pairs¹ in the total measured spectrum. These variables are unconstrained by default and are later fixed by the fitting procedure. To distinguish between free and fixed variables, an asterisk is attached to the latter; if for example the variable δ is fixed to a real number, it is denoted as δ^* .

¹as obtained from Monte Carlo.

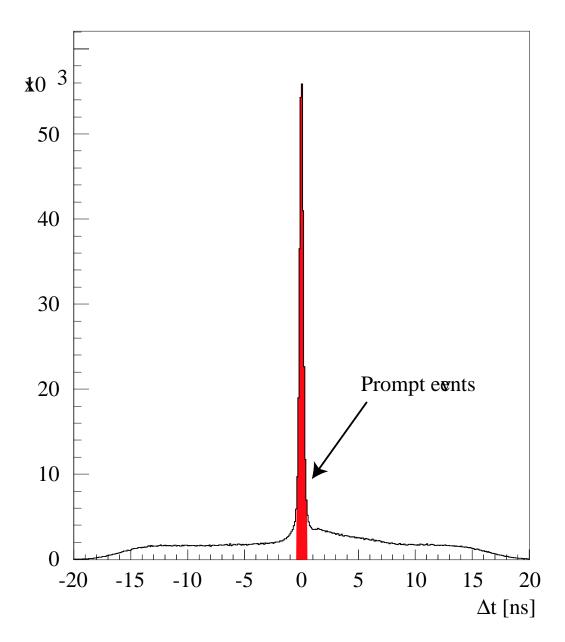


Figure 10.1: Time difference between positive and negative pion measured by the vertical hodoscopes for the selected events for $94\mu m$ target. The asymmetry on the right is due to protons. The (time correlated) prompt events are highlighted in red.

The range of the atomic pairs extends up to $Q=4~{\rm MeV/c}$ and $Q_l=2~{\rm MeV/c}$ as can be seen from figure 8.3. The Coulomb, accidental and non-Coulomb pairs on the other hand extend over the full Q range and are only limited by the event selection. Figure 8.8 (8.9) illustrates the Q projections of the Coulomb (accidental and non-Coulomb) pairs.

The production mechanisms of the three background contributions (accidental, non-Coulomb and Coulomb pairs) are described in detail in chapter 2. They are modeled using special Monte Carlo generators as described in chapter 7. The measured accidental pairs can be directly compared to Monte Carlo data. They match the MC data with high accuracy (see section 7.3 in chapter 7).

10.4.1 Accidental pairs

The time difference plot (figure 10.1) helps to identify the amount of accidental pairs $(\delta^*)^2$ in the prompt spectrum. If a constant fit is applied in the region of -12 ns $< dt_{VH} < -5$ ns, the accidental pair contamination for the $94\mu m$ target in the prompt region is $\delta^* = 6.8 \pm 0.1\%$ ($\delta^* = 7.2 \pm 0.1\%$ for the $98\mu m$). A linear fit yields for the $94\mu m$ target $\delta^* = 7.4 \pm 0.1\%$ (for $98 \mu m$ $\delta^* = 8.2 \pm 0.1\%$). In the following we assume that δ is uniformly distributed among these two extreme values. This leads to an average value for the $94\mu m$ target of $\delta^* = 7.1 \pm 0.17\%$ and for the $98\mu m$ target of $\delta^* = 7.7 \pm 0.3\%$.

10.4.2 Coulomb and non-Coulomb pairs

Subtracting the accidental pairs contamination from the prompt spectrum gives the sum of the atomic, Coulomb and non-Coulomb pairs:

$$\frac{dN^{Real}}{dQ} = \frac{dN^{Meas}}{dQ} - \delta^* \frac{dN^{Acc}}{dQ} = \alpha \frac{A_{2\pi}}{dQ} + \beta \frac{dN^{Coul}}{dQ} + \gamma \frac{dN^{Non-Coul}}{dQ} \quad (10.2)$$

We will call the sum of these three time correlated pairs **real pairs**. The Coulomb and non-Coulomb contributions in the real pair spectrum is evaluated by fitting them to the real pair spectrum above the signal region.

Fitting procedure

The atomic pairs are found below Q < 4 MeV/c and $Q_l < 2$ MeV/c. The background contributions (Coulomb and non-Coulomb pairs) are fitted simultaneously to the real spectrum above the signal region. With the above cuts (section 10.3) this translates into a fit of the background contributions Coulomb and non-Coulomb pairs to the real spectrum in Q_{long} within $2 < Q_{long} < 15$ MeV/c and in Q within 4 < Q < 15.5 MeV/c. The fitting algorithm uses a χ^2 minimization and it is based on Minuit[79].

²The * of the δ^* denotes that the free parameter δ has been fixed to the value δ^* .

We first normalize each background contribution to one, i.e.

$$\sum_{i=1}^{n} \left(\frac{dN_i^{Coul}}{dQ} \right) = \sum_{i=1}^{n} \left(\frac{dN_i^{NC}}{dQ} \right) = 1$$
 (10.3)

to have the additional convenience that the result of the fit, β^* and γ^{*3} , correspond to the total amount of observed Coulomb and non-Coulomb pairs in the sample. The χ^2 function to be minimized can then be written as the difference between the real spectrum and the background components. We can write in Q (Coul stands for Coulomb pairs, NC for Non-Coulomb and Acc for accidentals pairs):

$$\min \sum_{i=m}^{n} \left(\frac{\left(\frac{dN_i^{Real}}{dQ} - \beta \frac{dN_i^{Coul}}{dQ} - \gamma \cdot \frac{dN_i^{NC}}{dQ}\right)^2}{(\sigma_i^{Meas})^2 + (\delta^* \cdot \sigma_i^{Acc})^2 + (\beta \cdot \sigma_i^{Coul})^2 + (\gamma \cdot \sigma_i^{NC})^2} \right)$$
(10.4)

where i sums over the number of bins, starting from bin m, which is just outside the signal region. In the case of a 0.25 MeV/c binning, we start in Q the fit with bin number 17 (the signal extends up to 4 MeV/c which are the first 16 bins) and end with bin number 62 (= 15.5 MeV/c). The error terms per bin, σ_i^{Meas} , are calculated as the square root of the measured bin content. The error terms for the Monte Carlo background are calculated as the square root of the total Monte Carlo statistics in a particular bin. The final parameters β^* and γ^* which minimize function 10.4 are the relative background strengths. Once the values β^* and γ^* are found, the full background contribution can be subtracted in the signal region to obtained the signal as the residual between the measurement and the full background.

The procedure works in Q_{long} analogously. The fit extends from bin number 9 (from 2 MeV/c) up to bin number 60 (=15 MeV/c). In addition we can combine the Q and Q_l fit to a combined fit. The resulting χ^2 function is then defined as

$$\chi^{2} = \frac{1}{2} \sum_{i=m}^{n} \left(\frac{\left(\frac{dN_{i}^{Real}}{dQ} - \beta \frac{dN_{i}^{Coul}}{dQ} - \gamma \cdot \frac{dN_{i}^{NC}}{dQ}\right)^{2}}{(\sigma_{i}^{Meas})^{2} + (\sigma_{i}^{Acc})^{2} + (\sigma_{i}^{Coul})^{2} + (\sigma_{i}^{NC})^{2}} \right) + \frac{1}{2} \sum_{i=m}^{n} \left(\frac{\left(\frac{dN_{i}^{Real}}{dQ_{l}} - \beta \frac{dN_{i}^{Coul}}{dQ_{l}} - \gamma \cdot \frac{dN_{i}^{NC}}{dQ_{l}}\right)^{2}}{(\sigma_{i}^{Meas})^{2} + (\sigma_{i}^{Acc})^{2} + (\sigma_{i}^{Coul})^{2} + (\sigma_{i}^{NC})^{2}} \right)$$
(10.5)

The factor $\frac{1}{2}$ has been introduced to correct the double counting⁴. The combined fit yields one value for β and one for γ .

³The asterisk denotes that the parameter is fixed.

⁴Each event in Q is also found in Q_l . Hence the above χ^2 sum adds all events twice. The factor $\frac{1}{2}$ corrects for that.

Fit stability

The fit stability has been tested by changing the end of the fit range in equation 10.4 and is discussed as a systematical error in the following chapter.

Fit results

The background contributions from Coulomb and non-Coulomb pairs using a combined fit in Q and Q_{long} are shown in figure 10.2. The upper end of the fit

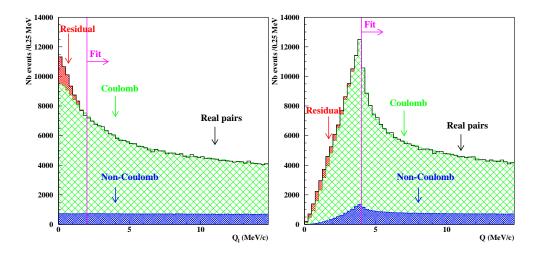


Figure 10.2: Real spectrum (black), fitted Coulomb (green) and non-Coulomb (blue) background and the resulting residual (red) in Q_l (left) and Q (right) for selected events from $94\mu m$ target. The magenta line denotes the start of the fit region.

range is chosen to be 15 MeV/c. Its stability is discussed below. The magenta line denotes the start of the fit region (which is above the signal region). The red residuals mark the expected atomic pair signals. The found fit parameters β^* and γ^* are printed in table 10.1. The errors are calculated by MINOS [79] and take into account the correlations between the parameters. The goodness of the fit is $\chi^2/ndf = 0.92$ (1.13) for the 94 (98) μ m target. The ratio of β^*/γ^* is equal for

Table 10.1: Fit parameter results for Coulomb (β^*) and non-Coulomb (γ^*) pairs. The errors are calculated with MINOS [79].

	$\beta^* (= N_{Coul})$	$\gamma^* (= N_{NC})$
94 μ m target	285199 ± 4743	42505±4193
98 μ m target	88823 ± 2633	14033 ± 2330

both targets within errors. The two fit parameters are correlated: If the amount of Coulomb pairs increases, the amount of non-Coulomb pairs naturally has to decrease. The correlation between the two parameter is $\rho =$ -0.99 for both targets as estimated by MINOS.

The parameters were unconstrained up to this point. To study a possible influence of constraining them on the error, the large negative correlation is used to constrain one parameter (i.e. γ) by knowing the measured number of events and the other parameter (β). If we take the amount of measured signal (α^* , taken from the residual fit) as given, we can use the constraint

$$\gamma = \text{Number of real events} - \alpha^* - \beta$$
 (10.6)

and obtain the fit results in table 10.2. The relative error on β decreases by about 25%, while for γ it decreases by 17% (94 μ m target). Due to the constraint, the error on γ is equal to the error on β .

Table 10.2: Fit results for Coulomb (β^*) and non-Coulomb (γ^*) pairs using the constraint of equation 10.6.

	$\beta^* (= N_{Coul})$	$\gamma^* (= N_{NC})$
94 μ m target	285199 ± 3475	42505±3475
98 μ m target	88823 ± 1918	14033 ± 1918

10.5 Atomic pair signal

The residuals in figure 10.2 are the excess events over the two background contributions and can be identified (according to equation 10.1) with the atomic pair signal. Subtracting the accidental, Coulomb and non-Coulomb contributions from the measured prompt spectrum yields the signal (see figure 10.3, red crosses). The black shape illustrates the signal of atomic pairs from Monte Carlo. The number of atomic pairs used in the black signal shape corresponds to the amount of residual events found for Q < 4 MeV/c. As the two plots show, there is a good agreement between the Monte Carlo signal and the one extracted from the measurement. The $98\mu\text{m}$ target signal extraction is analogous.

Table 10.3 summarizes the amount of atomic pairs for different cuts in Q and Q_{long} for the 94 μ m and 98 μ m target.

The residual signals in Q_l and Q agree on the percent level which demonstrates that the background is consistent and simulated very well.

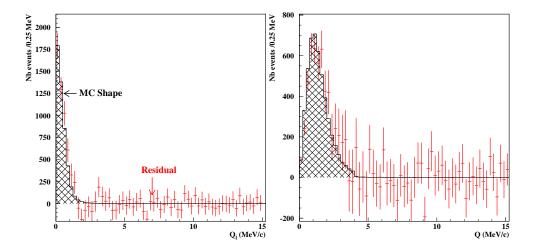


Figure 10.3: Residual of the measurement and the fitted background (red crosses) for Q_l and Q for the 94 μ m target. The black shape illustrates the signal from atomic pairs obtained with Monte Carlo. The number of atomic pairs used in the black signal shape corresponds to the amount of residual events found for Q < 4 MeV/c.

Table 10.3: Atomic pairs for the 94 μ m and the 98 μ m target for various Q_l and Q values for selected Ni 2001 events.

	94 μ m target	$98\mu m$ target	Ni 2001
Q < 3 MeV/c	4774±239	1505±130	6279 ± 271
Q < 4 MeV/c	5096 ± 328	1422 ± 178	6518 ± 373
$Q_l < 1 \text{ MeV/c}$	4726 ± 217	1304 ± 117	6030 ± 247
$Q_l < 2 \text{ MeV/c}$	5063 ± 290	$1446 {\pm} 157$	6509 ± 330

10.6 Breakup probability

The breakup probability P_{br} can be estimated according to equation 9.7. Taking the experimental k-factor from chapter 9 and the measured atomic and Coulomb pairs from the previous section yields directly the breakup probability. Table 10.4 illustrates the breakup probability for different Q_l , Q cuts. The breakup probability should be independent of the cut. Figure 10.4 shows P_{br} as a function of Q_l and Q cuts for the 94 μ m target. The breakup probability is stable above $Q_l > 0.75$ MeV/c and Q > 3 MeV/c. These are the regions where most of the signal is included in the calculations.

The reason for the deviation of P_{br} for small Q and for $1 < Q_l < 2$ MeV/c

1able 10.4	1 1	98 μ m target	00,0
Q < 3 MeV/c	0.443 ± 0.023	0.448 ± 0.041	0.444 ± 0.020
Q < 4 MeV/c	0.454 ± 0.030	0.406 ± 0.052	0.442 ± 0.026
$Q_l < 1~{ m MeV/c}$	0.458 ± 0.023	$0.406 {\pm} 0.038$	$0.444 {\pm} 0.020$
$Q_l < 2 \text{ MeV/c}$	0.455 ± 0.027	0.416 ± 0.047	0.445 ± 0.023

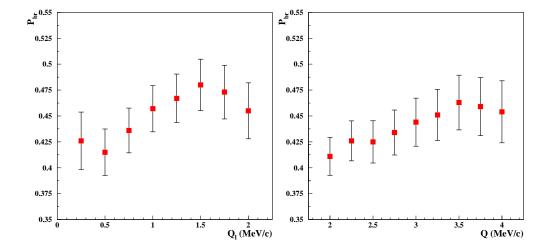


Figure 10.4: Breakup probability P_{br} as a function of the cut in Q_l and Q for $94\mu m$ target.

may be linked to a small error in the Monte Carlo atomic pair signal. The breakup probability can be rewritten (from equation 9.7):

$$\begin{split} P_{br} &= \frac{n_A^{Residual}(Q^{rec} < Q^{cut})}{N_{Coul}(Q^{rec} < Q^{cut})} \frac{1}{k^{exp}} = \\ &= \frac{n_A^{Residual}(Q^{rec} < Q^{cut})}{N_{Coul}(Q^{rec} < Q^{cut})} \frac{n_A^i N_{Coul}(Q^{rec} < Q^{cut})}{k^{th} n_A^{MC-Shape}(Q^{rec} < Q^{cut}) N_{Coul}(Q^{init} < 2)} \end{split}$$

The first part in the upper equation $(\frac{n_A^{Residual}(Q^{rec} < Q^{cut})}{N_{Coul}(Q^{rec} < Q^{cut})})$ comes from the measurement, while the second part $(\frac{1}{k^{exp}})$ comes from Monte Carlo. Please note the difference in the determination of the atomic pairs, which are either the residual of the measurement and the background $(n_A^{Residual})$ or which come from the Monte Carlo $(n_A^{MC-Shape})$.

To demonstrate the dependence of P_{br} on the atomic pair Monte Carlo shape,

we simplify this equation leaving the constants away and assuming that the input distribution of the Coulomb pairs are known without errors⁵. This leaves us with

$$P_{br} \propto \frac{n_A^{Residual}(Q^{rec} < Q^{cut})}{N_{Coul}(Q^{rec} < Q^{cut})} \frac{N_{Coul}(Q^{rec} < Q^{cut})}{n_A^{MC-Shape}(Q^{rec} < Q^{cut})}$$
(10.7)

When we construct the background to obtain $n_A^{Residual}$ from the measurement, we use the Monte Carlo background for the Coulomb pairs as we do for the Coulomb pairs in the k-factor calculation. Hence the two $N_{Coul}(Q^{rec} < Q^{cut})$ in equation 10.7 stem from the same Monte Carlo distribution, which means that their ratio is some constant. Finally we are left with a dependence of P_{br} on the ratio of residual atomic pairs and atomic pairs coming from the Monte Carlo shape:

$$P_{br} \propto \frac{n_A^{Residual}(Q^{rec} < Q^{cut})}{n_A^{MC-Shape}(Q^{rec} < Q^{cut})}$$
(10.8)

If the residual form of the atomic pairs obtained from the measurements does not perfectly coincide with the distributions obtained from Monte Carlo, we expect to see a dependence of P_{br} on Q_l and Q. Possible reasons for this mismatch are the description of the atomic pair shape at production or the description of the multiple scattering in GEANT. They are discussed in the following chapter (systematic errors).

Figure 10.3 shows the residual and the Monte Carlo shape of the atomic pairs signal in Q and Q_l . The mismatch in Q_l yields not enough pairs from Monte Carlo as compared to the residual around $Q_l = 1$ MeV/c, which is compensated by fewer atomic pairs within $1 < Q_l < 2$ MeV/c. The impact on the breakup probability is clearly visible (figure 10.4). The Q plot of figure 10.3 shows a shift of the atomic pair shape toward lower Q values. As a result the shape overestimates the amount of atomic pairs in the lower Q region (below Q < 2 MeV/c), while it underestimates it above 2 MeV/c. This translates into a linear dependence on P_{br} below 3.5 MeV/c. The integrated signals are nearly equal for Q and Q_l (see table 10.4), which translates into approximately equal breakup probabilities from both integrated signals. Since P_{br} from the integrated signals do not depend on the atomic pair shape they can be most trusted. In addition, the breakup probability obtained by cutting in the signal region have to be attached with a systematical error from the atomic pair shape (see next chapter).

⁵Which seems to be reasonable given that the Coulomb pairs are produced according to phase space and taking into account the Coulomb interaction at production.

10.7 Fitting with atomic pair shape constraint

The idea of the shape fit is to add to the fit equation 10.4 the Monte Carlo atomic pair shape to yield a new fit function 10.9.

$$\min \sum_{i=1}^{n} \left(\frac{\left(\frac{dN_i^{Real}}{dQ} - \alpha \frac{dN_i^{A_{2\pi}}}{dQ} - \beta \frac{dN_i^{Coul}}{dQ} - \gamma \cdot \frac{dN_i^{NC}}{dQ} \right)^2}{(\sigma_i^{Meas})^2 + (\sigma_i^{A_{2\pi}})^2 + (\sigma_i^{Coul})^2 + (\sigma_i^{NC})^2 + (\sigma_i^{Acc})^2} \right)$$
(10.9)

Since we include the atomic pair shape in the fit, we can start to fit from Q=0 MeV/c and extend over the whole momentum region. In addition, if we normalize the atomic pair Monte Carlo distribution to one (as shown in equation 10.3), the fit will give us directly the number of atomic pairs found in the sample (the parameter α) bundled with its error.

The result of fitting with the atomic pair shape depends on the accuracy of the used shape. For the residual plot (figure 10.3) we use the standard atomic pair shape which incorporates breakup from all states (for more details, see chapter 8). The residual plot shows a slight disagreement between residuals and Monte Carlo shape, so that a shape fit with this standard shape is not optimal. This problem can be resolved by using a phenomenological shape, which follows the measured residuals. Specifically since the standard atomic pair shape is to narrow, we increase the multiple scattering angle in GEANT by 10% for each scattering to obtain a wider atomic pair shape. This shape is then slightly adapted to follow the measured residuals (for a comparison of the shape and the residuals after the fit see figure 10.5).

This phenomenological shape can be used since the atomic pair input has never been experimentally verified. In addition, the only measurement which exists about the atomic pair shape are the residuals. Doing the minimization of equation 10.9 yields the fit parameters of table 10.5. The momenta distributions of the measurement and the background contributions are illustrated in figure 10.5. The fit values for Coulomb and non-Coulomb pairs are equal within error to those for the fit without atomic pair shape (background fit), but the errors on the fit parameters are clearly better. In the case of the atomic pairs, the error quoted in the previous section has been calculated according to the nominator in equation 10.4, while in the case of the shape fit, the atomic pair error is calculated by MINOS. The MINOS determines the errors an a given parameter by varying this parameter until the χ^2 function increases by one. This error analysis takes automatically into account the correlation between the three parameters and is hence very reliable.

The correlation between the three parameters read for the 94 (98) μ m target: $\rho_{\alpha\beta}$ =-0.626 (-0.631), $\rho_{\alpha\gamma}$ =0.585 (0.589) and $\rho_{\beta\gamma}$ =-0.977 (-0.977). An increase

Table 10.5: Fit parameters for atomic (α^*) , Coulomb (β^*) and non-Coulomb (γ^*) pairs with MINOS errors.

	$\alpha^* (= n_A)$	$\beta^* (= N_{Coul})$	$\gamma^* (= N_{NC})$
94 μ m target	5090 ± 256	285459 ± 3110	42229 ± 2926
98 μ m target	1468 ± 147	88823 ± 1734	13984 ± 1624
Ni 2001	$6558 {\pm} 295$	374282 ± 3561	56213 ± 3346

of atomic pairs is compensated by the fit with less Coulomb pairs and more non-Coulomb pairs.

Looking at the χ^2 function space reveals the contour of the parameters. Figure 10.6 shows the contour of atomic pairs to Coulomb pairs for 90% and 99% CL with the non-Coulomb as a free parameter⁶.

The total atomic pair signal in 2001 can be quoted with an accuracy of 4.5% to be

$$n_A^{2001} = 6558 \pm 295 \; (stat)$$
 (10.10)

The Coulomb pair background is determined with an accuracy of better than 0.7%, the non-Coulomb one with 4.2%. When restricting the signal to the Q and Q_l cuts from the previous section its strength changes slightly(table 10.6).

The contributions of the background from the shape fit below the signal in Q and Q_l is shown in table 10.6. Because of the shape fit the breakup probabilities⁷

Table 10.6: Atomic, Coulomb, non-Coulomb and real pairs from the shape fit for the 94 μ m and the 98 μ m target below the full signal.

	n_A	N^{Coul}	$N^{non-Coul}$	N^{Real}
94 μ m target				
$Q < 4 \ \mathrm{MeV/c}$	5057 ± 254	81218 ± 885	7808 ± 542	94101 ± 445
$Q_l < 2 \text{ MeV/c}$	5079 ± 255	62775 ± 685	5756 ± 399	73574 ± 393
98 μ m target				
$Q < 4 \ \mathrm{MeV/c}$	1458 ± 146	25331 ± 495	2547 ± 296	29320 ± 249
$Q_l < 2 \text{ MeV/c}$	1465 ± 147	19570 ± 382	1881 ± 188	22919 ± 219

in Q and Q_l are now equal and read $P_{br}^{94}=0.456\pm0.026,$ $P_{br}^{98}=0.415\pm0.046$ and

$$P_{br}^{2001} = 0.447 \pm 0.023 \tag{10.11}$$

⁶This figure was obtained by a fit of the 94 and 98μ m target together.

⁷The k-factor have to be adjusted for the phenomenological atomic pair shape used.

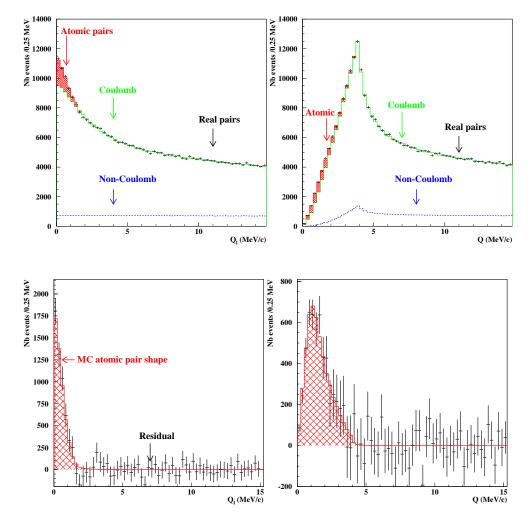


Figure 10.5: $94\mu m$ target data, shape fit. Top: Fit of the atomic (red), Coulomb (green) and non-Coulomb (blue) pairs to the measured spectra (black) in Q_l and Q. Bottom: Residual of the measurement and the fitted background (Coulomb and non-Coulomb) for Q_l and Q. The black shape illustrates the signal from atomic pairs obtained with Monte Carlo which was included in the fit.

They are compatible with the breakup probabilities from the background fit (table 10.4), which did not use the atomic pair shape in the fit. The errors on the other hand are smaller (figure 10.7).

The following section provides a cross check on the results by increasing the two hit requirement per SFD plane to three. The last section investigates the effect of finite size correction of the Coulomb enhancement function at production.

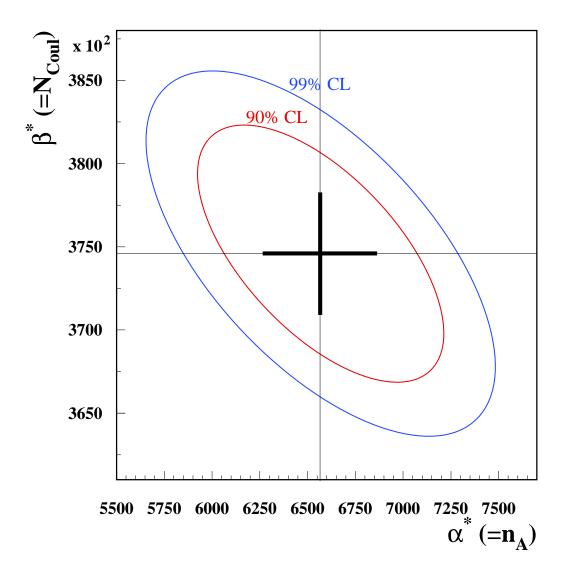


Figure 10.6: 90% CL and 99% CL of the fit results for atomic (α^*) versus Coulomb pairs (β^*) with the non-Coulomb pairs as a free parameter. The black point shows the central value.

10.8 Three hit events

The analysis up to this point is based on the event selection of section 10.3. Specifically the number of hit candidates per SFD plane was restricted to one or two to provide the cleanest possible event pattern. By increasing the number of accepted hit candidates to three per SFD plane while still restricting the number of accepted tracks per arm to one, we enlarge the data sample but introduce ambiguity in the SFD hit assignment.

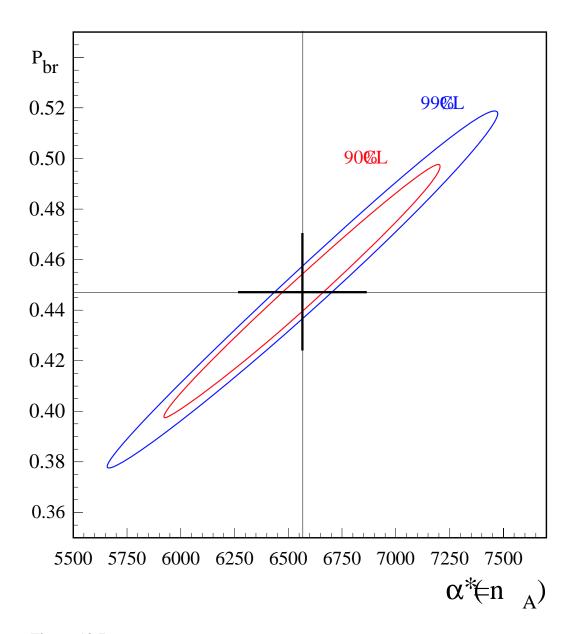


Figure 10.7: 90% CL and 99% CL of the fit results of the breakup probability versus atomic pairs (α^*) using the fit results shown in the previous figure 10.6. The black line displays the central value with its statistical measurement error.

The three hit events analysis provides a way to increase the signal strength with the back draw of introducing ambiguity in the SFD hit selection. It should provide a qualitative cross check of the above analysis.

The background contributions for three hit events are different. The accidental pair contamination is now for 94 (98) target $\delta^* = 8.3 \pm 0.2\%$ ($\delta^* = 9.1 \pm 0.2$).

A combined Q and Q_l fit as described in subsection 10.4.2 yields the number of Coulomb and non-Coulomb pairs (see table 10.7). The goodness of the fit is $\chi^2/ndf = 1.2$ (1.1) for the 94 (98) μ m target. The fit extends up to $Q_l = 15$ MeV/c and Q = 15.5 MeV/c. The ratio of β^*/γ^* is equal for both targets within errors.

Table 10.7: Fit parameter values for Coulomb (β^*) and non-Coulomb (γ^*) pairs for selected Ni 2001 events including three hit events. The errors are calculated with MI-NOS [79].

	$\beta^* (= N_{Coul})$	$\gamma^* (= N_{NC})$
94 μ m target	362630 ± 6685	65719 ± 6053
98 μ m target	113427 ± 3625	21673 ± 3285

By accepting three hit events the non-Coulomb background increases compared to the Coulomb pairs. The relative errors on the fit parameters increase as compared to the two hit events.

The atomic pair signal from three hit events is shown in table 10.8. The sig-

Table 10.8: Atomic pairs for the 94 μ m and the 98 μ m target for various Q_l and Q values with $Q_{trans} < 4$ MeV/c for selected Ni 2001 events including three hit events.

	$94\mu m$ target	$98\mu m$ target	Ni 2001
Q < 3 MeV/c	5924±277	1875±150	7799±315
$Q < 4 \ \mathrm{MeV/c}$	6443 ± 384	1790 ± 206	8233 ± 436
$Q_l < 1 \text{ MeV/c}$	5691 ± 252	1644 ± 135	7335 ± 286
$Q_l < 2 \text{ MeV/c}$	6211 ± 338	1836 ± 181	8047 ± 383

nal in Q and Q_l is equal within errors. Assuming a uniform distribution for the true signal strength yields a systematic error due to the difference Q and Q_l signal strengths of $\sigma(\Delta_{Q,Q_l})=53$ for $94\mu\mathrm{m}$, $\sigma(\Delta_{Q,Q_l})=18$ for $98~\mu\mathrm{m}$ target and $\sigma(\Delta_{Q,Q_l})=35$ for the total Ni 2001 data.

By accepting three hit events the total Ni 2001 statistics increases by 41.5%. The signal (+25%) and the Coulomb pairs (+27%) increase less than proportional, while the non-Coulomb (+54%) and accidental (+55%) pairs augment more than proportional. The bigger increase in background makes the relative error on the signal stay the same. The three hit analysis does hence not improve the relative signal uncertainty. On the other hand it induces uncertainty through ambigous SFD hit selection which compromises the background (the χ^2 deteriorates).

Table 10.9 summarizes the breakup probabilities for the three hit event analysis. The breakup probabilities from the $94\mu m$ target are higher than the ones from

	$94\mu m$ target	$98\mu m$ target	Ni 2001
Q < 3 MeV/c	0.437 ± 0.022	0.440 ± 0.035	0.438 ± 0.019
$Q < 4~{ m MeV/c}$	$0.454 {\pm} 0.028$	0.401 ± 0.047	0.440 ± 0.024
$Q_l < 1 \text{ MeV/c}$	0.440 ± 0.020	0.401 ± 0.033	0.430 ± 0.017
$Q_l < 2 \text{ MeV/c}$	0.435 ± 0.025	0.415 ± 0.041	0.430 ± 0.021

Table 10.9: Breakup probability P_{br} for cuts in Q_l , Q for three hit events.

the 98 target, in agreement with the two hit analysis. Overall the probabilities decrease (within the statistical error) for three hits as compared to two hits. This is due to relative more Coulomb background per signal for the 94 μ m target as compared to the 98 one.

10.9 Finite size correction

The theoretical Coulomb enhancement function used in the generator for Coulomb pairs can be corrected for finite size effects in the production process of the pions [80]⁸. Preliminary studies by Lednicky *et al.* [42] point out a possible correction for $A_c(Q)$ of the order of 2-3%. They propose the following Coulomb enhancement function:

$$A_c^{fs}(Q) = A_c(Q)(1.0017 - 0.0285((1 + (0.278 \cdot Q)^2)^{-0.421} - 1))$$
 (10.12)

where fs denotes finite size and $A_c(Q)$ is the theoretical Coulomb enhancement. The results from the fit (equation 10.4) are shown in table 10.10. The finite size

Table 10.10: Fit parameters for Coulomb (β) and non-Coulomb (γ) pairs with MINOS errors.

	$\beta^* (= N_{Coul})$	$\gamma^* (= N_{NC})$
94 μ m target	301419±5077	26559 ± 4510
98 μ m target	94055 ± 2799	8871 ± 2489

corrections affect the spectra of the Coulomb pairs by increasing higher Q while decreasing lower Q's, which leads to a fit with more Coulomb pairs and fewer

⁸The use of the square of the Sommerfeld functions at origin as the Coulomb enhancement parametrization assumes that the two pions of a Coulomb correlated pair are created at zero distance. This is of course not true and the small correction of the creation distance, which has nuclear range, receives the name of finite size effect.

non-Coulomb pairs. The residual signal is illustrated in table 10.11. It decreases by 4.6% in Q and 5.9% in Q_l . Figure 10.8 displays the spectra in Q_l and Q_l

Table 10.11: Residual atomic pair signal for the 94 μ m and the 98 μ m target using finite size corrections.

	94 μ m target	$98\mu m$ target	Ni 2001
Q < 4 MeV/c	4853 ± 332	1366±179	6219 ± 377
$Q_l < 2 \text{ MeV/c}$	4760 ± 293	1367 ± 158	6127±333

for the fit results and the residual with the (standard) MC atomic pair shape as comparison. The residual and the Monte Carlo shape agree well, but as before the MC shape seems to be to narrow.

The experimental k-factor is also influenced by the correction: The theoretical one changes from $k^{th}=0.6146$ to $k^{th,fs}=0.6142$. In addition, the changing Coulomb enhancement function changes the reconstructed spectra in Q and Q_l . The finite size corrected experimental k-factors are for the 94 (98) μ m target $k^{exp,fs}(Q=4{\rm MeV/c})=0.1360$ (0.1362) and $k^{exp,fs}(Q_l=2{\rm MeV/c})=0.1745$ (0.1747), which is a correction of 1.7%. The resulting breakup probabilities (see table 10.12) combine the two effects – less atomic pairs and more Coulomb pairs in the low Q region on the one hand, and a smaller k-factor on the other hand – which partially cancel each other out. Nevertheless the final breakup probabilities are about 6.6% (7.9%) smaller for $Q(Q_l)$ with the finite size corrections.

Table 10.12: Breakup probability P_{br} using finite size corrections.

	$94 \mu \mathrm{m}$ target	$98\mu\mathrm{m}$ target	Ni 2001
Q < 4 MeV/c	0.423 ± 0.029	0.382 ± 0.051	0.413 ± 0.025
$Q_l < 2 \text{ MeV/c}$	0.419 ± 0.027	0.385 ± 0.045	0.410 ± 0.023

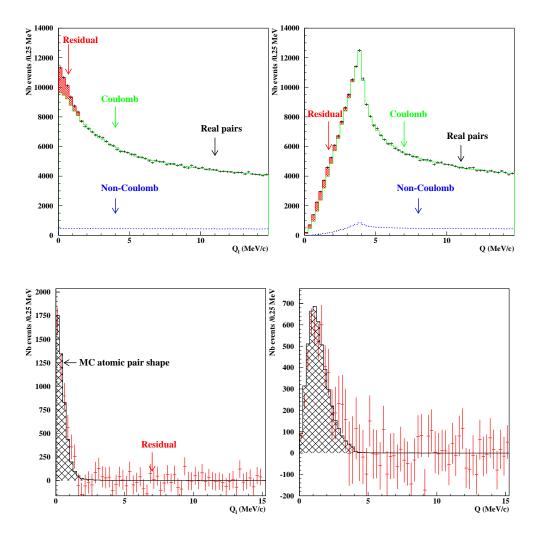


Figure 10.8: 94μ m target data. Top: Fitted Coulomb (green) and non-Coulomb (blue) pairs to the measured spectra (black) in Q_l and Q using finite size corrections. The residual signal is shown in red. Bottom: Residual of the measurement and the fitted background (Coulomb and non-Coulomb) for Q_l and Q. The black shape illustrates the signal from atomic pairs obtained with Monte Carlo. The number of atomic pairs used in the black signal shape corresponds to the amount of residual events found for Q < 4 MeV/c.

Chapter 11

Systematic effects

This chapter analysis systematic effects which may affect the breakup probability determination of the previous chapter for the background and the shape fit.

11.1 Accidental background

A systematical error can be attached to the accidental background (see section 10.4). The accidental pair contamination is estimated to be $\delta^* = 6.6 \pm 0.17\%$ for the $94\mu \text{m}$ and $\delta^* = 7.1 \pm 0.2\%$ for the $98\mu \text{m}$ target. This translates into changes of P_{br} as summarized in table 11.1. The accidental pairs are very similar to the non-

Table 11.1: Systematic change of P_{br} induced by the amount of accidental pairs (δ^*) in the spectrum for different Q, $|Q_l|$ cuts.

	$94\mu \mathrm{m}$ target	$98\mu m$ target
Q < 3 MeV/c	0.0006	0.0003
$Q < 4~\mathrm{MeV/c}$	0.0005	0.0002
$Q_l < 1 \text{ MeV/c}$	0.0004	0.0002
$Q_l < 2 \text{ MeV/c}$	0.0004	0.0002

Coulomb pairs. A change in δ^* is compensated by the fit with a similar change in the number of non-Coulomb pairs. The overall breakup probability is not affected.

11.2 Coulomb and non-Coulomb background

The Coulomb (β^*) and non-Coulomb (γ^*) background contributions are determined by fitting them simultaneously to the real pair spectrum (section 10.4.2)

in Q and $|Q_{long}|$. The influence of the fit range on the ratio β^*/γ^* is illustrated in figure 11.1. The fit range is stable in Q, $|Q_l|$ and for the combined fit while

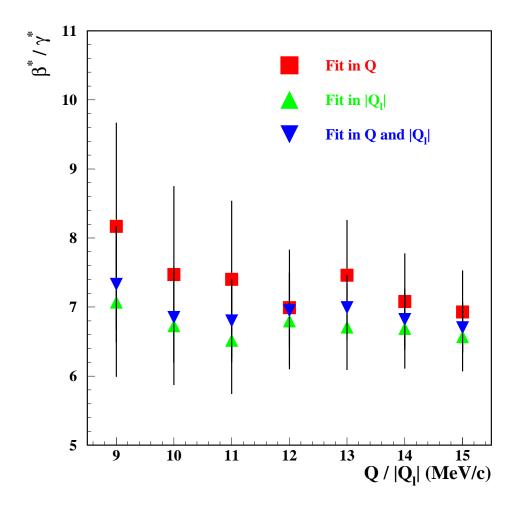


Figure 11.1: Ratio of Coulomb to non-Coulomb pairs (β^*/γ^*) for the $94\mu m$ target obtained from the fit in Q (red), $|Q_l|$ (green) and a combined fit in Q and $|Q_l|$ (blue).

changing the fit range. The relative error decreases as a function of the fit range, which is due to more degrees of freedom in the fit. The resulting ratio from Q and $|Q_l|$ can be regarded as two extreme values, the combined fit produces a ratio somewhere in the middle. The difference between the two extreme ratios per fit range define a systematic error. The optimal fit range with respect to the relative error as well as with respect to the systematic deviation is Q, $|Q_l| = 15 \text{ MeV/c}$. At this point, the systematical uncertainty of the fit on the breakup probability is

0.026. Dividing by $\sqrt{12}$ yields a systematical deviation in the breakup probability of $\sigma_{bk-cc/nc}=0.008$.

11.3 Additional restrictions in Q_{trans}

A further restriction on Q_{trans} from $Q_{trans} < 4$ MeV/c to $Q_{trans} < 3$ MeV/c means cutting into the signal region. This reduces the background more than the signal, which increases the relative accuracy on the signal strength. The drawback of a tighter cut is the systematical uncertainty induced by the (not measured) atomic pair shape in the breakup calculation.

Table 11.2 shows the atomic pair signal for different Q_{trans} cuts. The signal strengths decrease with tighter Q_{trans} cuts. Nevertheless, when comparing in Q the results are consistent when considering the cuts: The results for Q < 3 MeV/c are nearly identical for $Q_{trans} < 4$ MeV/c as well as for $Q_{trans} < 3$ MeV/c. Since the distribution in Q_l is integrated over all Q_{trans} we do not expect to see identical number of events.

Table 11.2: Atomic pairs for the 94 μ m and the 98 μ m target for various Q_l , Q_{trans} and Q values for selected Ni 2001 events.

	$94\mu\mathrm{m}$ target	$98\mu m$ target	Ni 2001
0	71		
$Q_{trans} < 4 \text{ MeV}$	V/C		
Q < 3 MeV/c	4774 ± 239	1505 ± 130	6279 ± 271
$Q < 4~\mathrm{MeV/c}$	5096 ± 328	1422 ± 178	6518±373
$Q_l < 1 \text{ MeV/c}$	4726±217	1304±117	6030±247
$Q_l < 2 \text{ MeV/c}$	5063 ± 290	1446 ± 157	6509 ± 330
$Q_{trans} < 3~{ m MeV/c}$			
Q < 3 MeV/c		1455±130	6267±271
$Q_l < 1 \text{ MeV/c}$	4428±180	1244±98	5672±205
$Q_l < 2 \text{ MeV/c}$	4749±236	1367 ± 129	6116 ± 269

The breakup probabilities for different Q_{trans} are shown in table 11.3. There is a tendency toward lower P_{br} for tighter Q_{trans} cut as we have already seen for tighter Q or Q_l cuts (See figure 10.4). This can be explained with the increasing dependence of the breakup probability on the atomic pair shape (through the k-factor calculation). If the atomic pair shape from Monte Carlo is under estimated

as compared to the measured residual, the k-factor is overestimated for tight Q_{trans} cuts, which translates into a too small breakup probability.

Table 11.3: Breakup probability P_{br} for the 94 μ m and the 98 μ m target for various Q_l , Q_{trans} and Q values for selected Ni 2001 events.

	$94\mu\mathrm{m}$ target	$98\mu\mathrm{m}$ target	Ni 2001
$Q_{trans} < 4 \mathrm{MeV}$	V/ c		
Q < 3 MeV/c	0.443 ± 0.023	0.448 ± 0.041	0.444 ± 0.020
Q < 4 MeV/c	0.454 ± 0.030	0.406 ± 0.052	0.442 ± 0.026
$Q_l < 1 \text{ MeV/c}$	0.458±0.023	0.406±0.038	0.444±0.020
$Q_l < 2 \text{ MeV/c}$	0.455 ± 0.027	0.416 ± 0.047	0.445 ± 0.023
$Q_{trans} < 3~{ m MeV/c}$			
Q < 3 MeV/c	0.449 ± 0.023	0.429 ± 0.040	0.444 ± 0.020
$Q_l < 1 \text{ MeV/c}$	0.446 ± 0.019	0.397 ± 0.033	0.434 ± 0.016
$Q_l < 2 \ \mathrm{MeV/c}$	0.444 ± 0.023	$0.404{\pm}0.040$	0.434 ± 0.020

The statistical error for $Q_{trans} < 3$ MeV/c is smaller, but a systematical error has to be attached due to the uncertainty of the atomic pair shape, which becomes bigger, the tighter the cuts. This is illustrated in the following section.

The systematical error when applying a Q_{trans} cut can be estimated by changing the cut and looking for the difference in P_{br} (figure 11.3). When applying a $Q_{trans} < 4$ MeV/c cut, the two extreme values are $P_{br} = 0.449$ ($Q_{trans} < 2$ MeV/c) and $P_{br} = 0.454$ ($Q_{trans} < 4$ MeV/c), so that the difference of the two extreme values amounts to 0.005. Assuming that the true value is uniformly distributed in between, we can quote a systematical error on $Q_{trans} < 4$ MeV/c of $\sigma_{Q_{trans}} = 0.005/\sqrt{12} = 0.0014$.

11.4 Atomic pair shape

Figure 10.4 as well as table 11.3 highlight a dependence of the breakup probability on the cut when cutting into the signal. This systematic deviation comes from a mismatch between the atomic pair shape (simulated, from Monte Carlo) and the atomic pair signal (which is the measured residual) and which enters the breakup probability through the k-factor calculation. The shape is shifted toward smaller Q values as compared to the residuals (see figure 10.3). A possible reason

is the Monte Carlo input spectrum of the atomic pairs, where we rely on calculations only. The input spectrum is composed of the spectra of the different pionium atom states after breakup according to [27]. Specifically, the Q value of the peak for principal quantum number n_i scales as $\frac{1}{2n_i}$, while the peak amplitude is proportional to $\frac{1}{n_i^2}$. To estimate a possible systematic error introduced by this signal shape, we compare it with the two extreme cases available in the model: All atoms break up with zero relative momentum Q, which gives the smallest possible Q distribution, and all atoms break up in 1s, which yields the biggest Q distributions for the atoms. The k-factors and the corresponding breakup probabilities are then evaluated as a function of the cut. The results for $Q_{trans} < 4 \text{ MeV/c}$ are presented in figure 11.2.

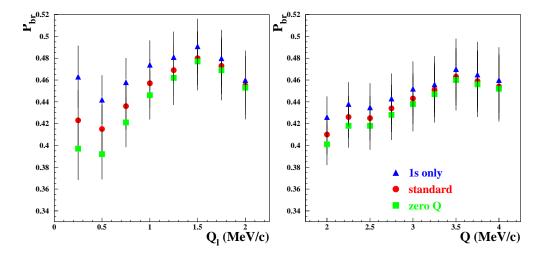


Figure 11.2: Breakup probability P_{br} as a function of the cut for atomic pair shape modeled as standard (red circles), 1s breakup only (blue triangles) and zero Q (green boxes) breakup for $94\mu m$ target Ni 2001 selected events.

Figure 11.3 illustrates P_{br} for different cuts in Q_{trans} as well as the systematical error induced by cutting in Q_{trans} due to different atomic pair shapes. The breakup probability is stable above Q=3 MeV/c and independent on the Q_{trans} cut due to the fact that the whole signal is considered in the calculation. When cutting into the signal, the breakup probability decreases (as we have seen already in the previous figure 11.2), while the dependency on the atomic pair shape and hence the systematical error increases.

The breakup from 1s states only is less dependent on the cut in Q as well as in Q_l . The case where all atoms break up with zero Q seems to be the least favorable. These results show that our signal starts to become sensitive to details of the atomic pair shape, which must not necessarily have a physics origin, but

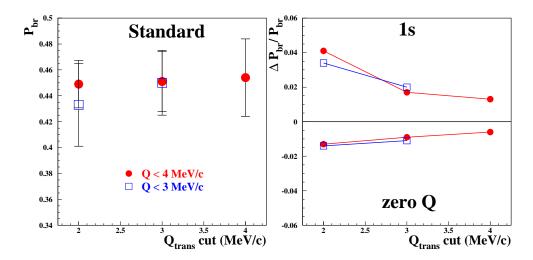


Figure 11.3: Left plot: Breakup probability P_{br} as a function of the cut in Q_{trans} for Q < 3 MeV/c (blue) and Q < 4 MeV/c (red) for 94 μ m target. Right plot: systematical error ($\Delta P_{br}/P_{br}$) on the breakup probability for 1s (top) and Zero Q (bottom) atomic pair shape relative to the standard one.

might be introduced by an insufficient simulation of additional hits (cross-talk, backscattered particles).

The plots show clearly the influence of the atomic pair shape on the breakup probability when cutting into the signal region which translates into a systematic uncertainty. For Q=4 MeV/c the difference ΔP_{br} between the two extreme cases is only 0.008, while for Q=2 MeV/c it is already 0.025. The most reliable breakup probability estimation with the smallest systematic error is hence obtained by integrating over the signal (i.e. $Q_{trans} < 4$ MeV/c and Q=2 MeV/c, $|Q_l|=2$ MeV/c) and yields a systematical uncertainty of $\sigma_{Shape}(Q=4$ MeV/c) = $0.008/\sqrt{12}=0.0023$.

11.5 Influence of multiple scattering

The multiple scattering in the Monte Carlo is based on the GEANT cross sections. In our momentum range they are no better than 5% [81]. To be sensitive to systematic influences of multiple scattering, the multiple scattering angle in GEANT was increased or decreased by 5% for each scattering calculation. This changes the Monte Carlo background. In addition, the experimental k-factor is recalculated. The resulting breakup probability as a function of the cut in Q and Q_l is drawn in figure 11.4. The values for standard (red circles), 5% bigger (blue

triangles), 10% bigger (magenta triangles) and 5% smaller (green boxes) multiple scattering are shown.

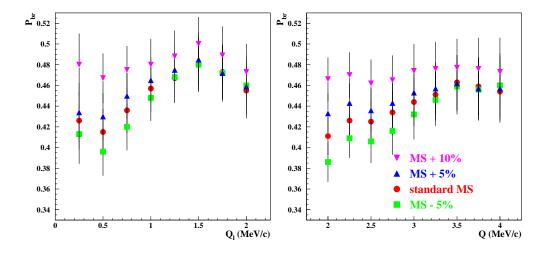


Figure 11.4: Breakup probability P_{br} for the 94 μ m target as a function of the cut for standard (red circles), 5% bigger (blue triangles), 10% bigger (magenta triangles) and 5% smaller (green boxes) multiple scattering.

The breakup probabilities when changing the multiple scattering by 5% in figure 11.4 converge toward the the values from the standard multiple scattering for higher Q and Q_l values. This implies a smaller systematic error from a multiple scattering uncertainty at higher cuts. The deviation on the breakup probability at $Q=4\,\mathrm{MeV/c}$ for more and less multiple scattering amounts to 1% while at $Q=2\,\mathrm{MeV/c}$ the difference is already 4.7%. When increasing the multiple scattering by 10%, the breakup probability curve as a function of the cut in Q and Q_l increases by around 1.5%. It seems that when increasing the multiple scattering by 10%, the background changes significantly. The assumption that the multiple scattering is wrong by 10% seems very strong in the light of precise measurements of this quantity in other momentum conditions. A somewhat smaller error of 5% is more realistic and used for the determination of the systematical error.

The change in the breakup probability due to a change in the multiple scattering angle by 5% amounts to 0.003 on both sides. This corresponds to a change per 1% in the ms angle of $\Delta(P_{br})=0.0006$. The breakup probabilities stabilizes for higher Q's which is most pronounced for the case where the multiple scattering was increased by 5%. This might indicate that the multiple scattering description in GEANT slightly under estimates nature in this momentum region. The atomic pair signal with 5% more multiple scattering is shown in figure 11.5. The Monte Carlo shape fits the residuals well.

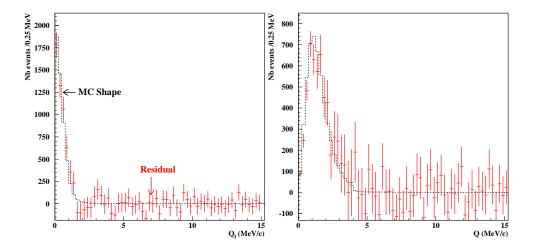


Figure 11.5: Atomic pair signal in Q_l and Q for $94\mu m$ target with 5% increased multiple scattering.

When comparing to the standard analysis (see figure 10.3), we note that the shape and the residuals in the analysis with 5% more MS fit in particular better in the momentum range between 2 MeV/c < Q < 4 MeV/c.

11.6 Summary

Systematical influences on the breakup probability were studied. Their strength depends strongly on the cut applied. When taking the total signal as for the shape fit, the systematical uncertainties turn out to be small and non-dominant as compared to the statistical error. The systematical uncertainties on the breakup probability studied are summarized in table 11.4.

The systematical error on the background for accidental and Coulomb/non-Coulomb pairs is estimated to be

$$\sigma_{Bk-acc} = 0.0005$$

$$\sigma_{Bk-Coul,NC} = 0.008^*$$

where the * denotes that the error was estimated having two extreme cases. The error due to the $Q_{trans} < 4~{\rm MeV/c}$ cut reads

$$\sigma_{Q_{trans}} = 0.0014^*$$

Table 11.4: Studied systematic errors on the breakup probability as well as on the lifetime. The errors with an asterisk (*) are errors calculated from two extreme values, assuming the true value to be uniformly distributed in between them.

Error source	Description	σ_{syst} (full signal)
Accidentals (δ^*)	Influence on P_{br} when	0.0005
	changing δ by 1σ	
$CC / NC (\beta^*/\gamma^*)$	Change in P_{br} for	
	Q_l or Q fit separately	0.008^{*}
	ΔP_{br} =0.026	
$Q_{trans} < 4 \text{ MeV/c}$	Change in P_{br} for	
	$Q_{trans} < 3 \text{ MeV/c}$:	0.0023*
	ΔP_{br} =0.008	
Multiple scattering	Change in P_{br} for	
	changing multiple scattering angle	0.0006
	by 1%	
Atomic pair shape	Change in P_{br} for	
	1s or $Q = 0$ MeV/c atomic pair input	0.0023*
	ΔP_{br} =0.008	
Total		0.009
Finite size corrections	Change of the central value of P_{br}	-0.0355
	using finite size corrections	

The systematical error due to the multiple scattering per 1% change in the scattering angle is

$$\sigma_{MS-per1\%} = 0.0006$$

Finally, the uncertainty due to the atomic pair shape is

$$\sigma_{Shape} = 0.0023^*$$

Taking all those errors together (using a deviation of the multiple scattering by 5%, which is the precision with which the ms has been measured for our conditions) yields a total systematical error of

$$\sigma_{syst} = 0.009 \tag{11.1}$$

which is roughly half the statistical error from the shape fit.

This leads to the following final value of the breakup probability taking into account all studied errors of

$$P_{br}^{Ni-2001} = 0.447$$
 $\pm 0.023 \, (stat)$ $\pm 0.0081^* \, (bk)$ $\pm 0.0014^* \, (Q_{trans})$ $\pm 0.003 \, (5\% - MS)$ $\pm 0.0023^* \, (shape)$

adding all error sources together yields:

$$P_{br}^{Ni-2001} = 0.447 \pm 0.025 \ (tot)$$
 (11.2)

and taking into account finite size corrections lowers the breakup probability to

$$P_{br,finite-size}^{Ni-2001} = 0.412 \pm 0.025 \ (tot) \tag{11.3}$$

Chapter 12

Lifetime determination

The lifetime τ can be calculated from the breakup probability of equation 10.11 using the cross section from Glauber as described in a paper by Santamarina *et al.* [30] (figure 12.1) and reads

$$\tau^{Ni-2001} = 2.85^{+0.45}_{-0.38} (stat) \text{ [fs]}$$
 (12.1)

using the statistical uncertainty only. When taking into account the systematical uncertainties as well (see equation 11.2), the total error on the lifetime becomes

$$\tau^{Ni-2001} = 2.85^{+0.48}_{-0.41} (tot) [fs]$$
 (12.2)

which is compatible with the theoretical prediction [7, 10]. The errors are asymmetric due to the nonlinear relationship between P_{br} and τ . An error of around 5% on P_{br} translates into an asymmetric error of +17% and -14%. Figure 12.2 shows the 90% and 99% CL of the lifetime. The shaded areas show the influence of the systematical errors.

The target thickness enters the into the calculation of the lifetime for a given breakup probability. Assuming an uncertainty of $\pm 2\mu$ m, the systematical error induced by the target thickness for a breakup probability of $P_{br}=0.447$ is

$$\sigma_{\tau}(P_{br} = 0.447) = 2.85^{+0.02}_{-0.02}$$
 (12.3)

This value is the difference between the evaluated lifetime for a 92 and a 94 μ m and a 96 and a 94 μ m target for a breakup probability of $P_{br}=0.447$. The finite size corrections change the lifetime to

$$\tau_{finite-size}^{Ni-2001} = 2.29_{-0.34}^{+0.39} (tot) [fs]$$
 (12.4)

which is also consistent with the theoretical value.

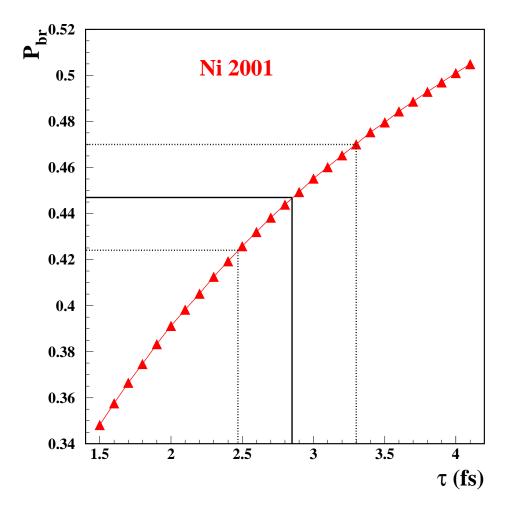


Figure 12.1: Determination of the life time τ and its error using the Glauber cross section as described in [30] for Ni 2001.

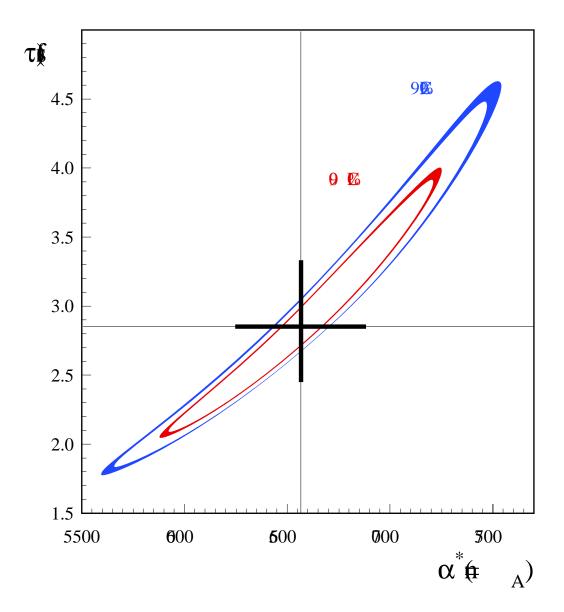


Figure 12.2: 90% and 99% CL of the lifetime τ . The shaded areas show the influence of the systematical errors. The black cross displays the central value with its error.

Chapter 13

Summary and conclusion

The DIRAC collaboration has successfully observed high statistics $\pi^+\pi^-$ pairs from pionium breakup and has measured the breakup probability in a dedicated Nickel run in 2001. The Nickel 2001 data is the largest homogeneous piece of data the DIRAC collaboration has recorded to date. Accordingly, the observed signal strength and breakup probability of this sample is the main contribution to the final results which will include all recorded data.

The Nickel 2001 analysis extracts the atomic pair signal from breakup on top of a dominant background at very small relative momenta by simulating the signal and the different background contributions using dedicated generators and high statistics Monte Carlo data. The precise simulation of the signal and the background allows to measure the signal strength with a statistical uncertainty of only 4.5% using an atomic pair shape in the fit. It is measured to be

$$n_A^{Ni-2001} = 6558 \pm 295 \; (stat)$$

The breakup probability is calculated using the fact that the pionium atoms and the Coulomb pairs are produced in the same process and taking into account the setup efficiency and acceptance. The observed breakup probability is $P_{br} = 0.447 \pm 0.023$ (stat).

Systematical influences on the breakup probability were studied. Their strength depends strongly on the cut applied. When taking the total signal as for the shape fit, the systematical uncertainties turn out to be small and non-dominant as compared to the statistical error. The total systematic error is estimated to be $\sigma_{syst} = 0.009$. This yields a final breakup probability of

$$P_{br}^{Ni-2001} = 0.447 \pm 0.023 \; (stat) \; \pm 0.009 \; (syst) = 0.447 \pm 0.025 \; (tot)$$

The corresponding lifetime τ for the pionium atom can then be calculated to be:

$$\tau^{Ni-2001} = 2.85^{+0.48}_{-0.41} (tot)$$

The finite size corrections change the lifetime to

$$\tau_{finite-size}^{Ni-2001} = 2.29_{-0.34}^{+0.39} (tot) [fs]$$

Both results are consistent with the theoretical prediction of $\tau = 2.9 \pm 0.1$ [fs] [7, 10].

The primary goal of observing high statistics $\pi^+\pi^-$ pairs from pionium breakup and measuring their breakup probability with an accuracy of about 5% has been achieved. The corresponding lifetime τ of the atom is measured with 16%. Combining the measurements from 2000 to 2003 should lower the error on the lifetime to under 10%.

Bibliography

- [1] B. Adeva et al., DIRAC proposal, CERN/SPSLC 95-1, SPSLC/P 284 (1995).
- [2] S. Deser et al., Phys. Rev. 96 (1954) 774.
- [3] J. Uretsky and J. Palfrey, Phys. Rev. 121 (1961) 1798.
- [4] S. M. Bilenky et al., Yad. Phys. 10 (1969) 812; (Sov. J. Nucl. Phys. 10 (1969) 469).
- [5] H. Jallouli and H. Sazdjian, Phys. Rev. D58 (1998) 014011; Erratum: ibid., D58 (1998) 099901.
- [6] M. A. Ivanov et al. Phys. Rev. D58 (1998) 094024.
- [7] J. Gasser et al., Phys.Rev. D64 (2001) 016008; hep-ph/0103157.
- [8] A. Gashi et al., Nucl. Phys. A699 (2002) 732.
- [9] S. Weinberg, Physica A96 (1979) 327,
 J. Gasser and H. Leutwyler, Phys. Lett. B125 (1983) 325 and Nucl. Phys. B250 465, 517, 539.
- [10] G. Colangelo, J. Gasser and H. Leutwyler, Nucl. Phys. B603 (2001) 125.
- [11] G. Colangelo, J. Gasser and H. Leutwyler, Phys. Rev. Lett. 86 (2001) 5008.
- [12] S. Pislak et al., Phys. Rev. Lett. 87 (2001) 221801.
- [13] S. Pislak et al., Phys. Rev. D 67 (2003) 072004.
- [14] M. Knecht et al., Nucl. Phys. B457 (1995) 513.
- [15] L. L. Nemenov, Yad. Fiz. 41 (1985) 980; Sov. J. Nucl. Phys. 41 (1985) 629).
- [16] O. E. Gorchakov et al., Yad. Fiz. 59 (1996) 2015; (Phys. At. Nucl. 59 (1996) 1942).

[17] O. E. Gorchakov et al., Yad. Fiz. 63 (2000) 1936; (Phys. At. Nucl. 63 (2000) 1847).

- [18] L. S. Dulian and A. M. Kotsinian, Yad.Fiz. 37 (1983) 137; (Sov. J. Nucl. Phys. 37 (1983) 78).
- [19] S. Mrówczyński, Phys. Rev. A33 (1986) 1549,S. Mrówczyński, Phys. Rev. D36 (1987) 1520,K. G. Denisenko and S. Mrówczyński, ibid. D36 (1987) 1529.
- [20] L. G. Afanasyev and A.V. Tarasov, Yad. Fiz. 59 (1996) 2212, (Phys. At. Nucl. 59 (1996) 2130).
- [21] Z. Halabuka et al., Nucl. Phys. B554 (1999) 86.
- [22] A. V. Tarasov and I.U. Khristova, JINR-P2-91-10, Dubna 1991.
- [23] O. O. Voskresenskaya, S.R. Gevorkyan and A.V. Tarasov, Phys. At. Nucl. 61 (1998) 1517.
- [24] L. Afanasyev, A. Tarasov and O. Voskresenskaya, J. Phys. G 25 (1999).
- [25] D. Yu. Ivanov, L. Szymanowski, Eur. Phys. J. A5 (1999) 117.
- [26] T. A. Heim et al., J. Phys. B33 (2000) 3583.
- [27] T. A. Heim et al., J. Phys. B34 (2001) 3763.
- [28] M. Schumann et al., J. Phys. B35 (2002) 2683.
- [29] L. Afanasyev, A. Tarasov and O. Voskresenskaya, Phys.Rev.D 65 (2002) 096001, hep-ph/0109208.
- [30] C. Santamarina et al., J. Phys. B36 (2003) 4273.
- [31] L.G. Afanasyev et al., Phys. Lett. B308 (1993) 200.
- [32] L.G. Afanasyev et al., Phys. Lett. B338 (1994) 478.
- [33] L.G. Afanasyev et al., Communication JINR P1-97-306, Dubna, 1997.
- [34] D. E. Groom *et al.*, Eur. Phys. J. **C15** 1 (2000).
- [35] Barry R. Holstein, hep-ph/9510344, (1995).
- [36] S. Weinberg, Phys. Rev. Lett. 17 616 (1966).

- [37] J. Gasser and H. Leutwyler, Ann. Phys. **158** 142 (1984).
- [38] H. W. Hammer et al. Eur. Phys. J. A 6 115 (1999).
- [39] A. D. Sakharov, Zh. Eksp. Teor. Fiz. 18 631 (1948).
- [40] R. Lednický, Proceedings of the HadAtom 99 Workshop, BUTP-99/26 (1999).
- [41] Z.K. Silagadze, JETP. Lett. **60** 689 (1996).
- [42] R. Lednický and J. Smolik, Private communication (2003).
- [43] I. Amirkhanov, I. Puzynin, A. Tarasov, O. Voskresenskaya and O. Zeinalova, Phys. Lett. **B452** 155 (1999).
- [44] L.G. Afanasyev et al., Phys. At. Nucl. 60 938 (1997).
- [45] FRITIOF 6, available from CERN.
- [46] Gillespie, G. H., Phys. Rev. A18 1967 (1978).
- [47] C. Santamarina, PhD thesis, University of Santiago de Compostella (2001).
- [48] B. Adeva et al., Nucl. Instr. Meth. **A515** 467 (2003).
- [49] F. Gomez, private communication (2003).
- [50] A. Gorin *et al.* NIM **A452** 280 (2000).
- [51] D. Goldin and L. Tauscher, DIRAC Internal Note 2002-07 (2002).
- [52] F. Takeutchi, Presentation at DIRAC analysis meeting, unpublished (2002).
- [53] M. Gallas *et al.*, DIRAC Internal Note 1998-06 (1998).
- [54] B. Adeva et al., NIM **A491** 41 (2002).
- [55] A. Lanaro, DIRAC Internal Note 2002-02 (2002).
- [56] L. Afanasyev et al., Nucl. Instr. Meth. A491 376 (2002).
- [57] S. Vlachos, DIRAC Internal Note 2003-04 (2003).
- [58] P. Kokkas, M. Steinacher, L. Tauscher, S. Vlachos, Nucl. Instr. Meth. A471 358 (2001).
- [59] FERA, LeCroy Corporation, Application Note AN-4004A.

- [60] F. Gomez and P. Vasquez, DIRAC Internal Note 2000-01 (2000).
- [61] V. Karpukhin and A. Kulikov, JINR E10-2001-2 (2001).
- [62] V.G.Olshevsky and S.V.Trusov, NIM **A469** 216 (2001).
- [63] Ch. P. Schuetz and L. Tauscher, DIRAC Internal Note 2003-06 (2003).
- [64] DIRAC offline analysis code ARIANE, 304-34 (2003).
- [65] P. Maybeck, Stochastic Models, Estimation and Control, Volume 1. Academic Press, New York (1979).
- [66] V. Yazkov, Description of the subroutine ClCovMtrDC, unpublished (2002).
- [67] R. Fernow, Introduction to experimental particle physics, Paperback, Cambridge University Press (1989).
- [68] Ch. P. Schuetz and L. Tauscher, DIRAC Internal Note 2002-04 (2002).
- [69] Monte Carlo program GEANT, version 3.21 adapted to DIRAC in its version 2.63 (2003).
- [70] http://zrelov.home.cern.ch/zrelov/dirac/montecarlo/instruction/instruct26.html.
- [71] http://dirac.web.cern.ch/DIRAC/offlinedocs/SimulData.html.
- [72] C. Santamarina and Ch. P. Schuetz, DIRAC Internal Note 2003-09 (2003).
- [73] Ch. P. Schuetz, DIRAC Internal Note 2001-07 (2001).
- [74] V. Yazkov, private communication (2003).
- [75] Ch. P. Schuetz and L. Tauscher, DIRAC note 2002-01 (2002).
- [76] T. A. Heim, Talk at the HadAtom01 hep-ph/0112293 (2001).
- [77] O. Gortchakov and C. Santamarina, DIRAC note 2004-01 (2004).
- [78] Frodesen, Skjeggestad and Tofte, Probability and statistics in particle physics, Universitetsforlaget (1979).
- [79] MINUIT version 94.1, http://wwwasdoc.web.cern.ch/wwwasdoc/minuit/minmain.html.
- [80] R. Lednicky and V.L. Lyuboshitz, Sov. J. Nucl. Phys. **35** 1316 (1982).
- [81] V. Krouglov, Accuracy of the multiple scattering description of GEANT for the DIRAC conditions. Talk given at a DIRAC meeting, unpublished (2003).

[82] A. Kouptsov, Presentation made in DIRAC analysis meeting, unpublished (2002).

Acknowledgments

The last four years were a very interesting and challenging time for me. I enjoyed the very personal atmosphere in the Basel group working for the DIRAC experiment at CERN and teaching in Basel. I would like to thank everyone who contributed to this work and would like to mention specially

- Ludwig Tauscher who supported me during my work and help and taught me a lot about physics as well as about life. The discussions during work, lunch and occasional skiing trips are always remembered.
- Leonid Nemenov for sharing with me his very profound knowledge about exotic atoms and the idea behind the DIRAC experiment.
- Cibran Santamarina for explaining me the underlying concepts of DIRAC many times without getting mad and for all the excellent dinners we had together.
- Daniel Goldin for years of common work place and home place, for the many evenings we spent together and the many discussions we had about work and not so work related items.
- Angela Benelli for the good atmosphere in our office and the many good ideas she shared with me.
- Sotiris Vlachos for teaching me lots of statistical concepts.
- Panos Kokkas for his initial support before he went to Greece.
- Valeri Yazkov for helping me with ARIANE and reading carefully the manuscript.
- Valeri Brekhovskhi, Oleg Gortchakov, Juerg Schacher, Valeri Yazkov and all other collaborators from DIRAC for running this great experiment.

Above all I would like to thank my parents and my brothers for their relentless help and support and to my love Alexia for her love, support and understanding.

Curriculum vitae

Christian Peter Schütz

Mühlestiegrain 40 CH-4125 Riehen

Date of Birth May 11, 1975 Citizenship Swiss

Education and Employment

2000-2004	PhD Thesis in experimental physics (summa cum laude), Basel University
	Research with the DIRAC experiment at CERN
	Teaching at the University of Basel
	Supervisor: Ludwig Tauscher
1999-2003	Lizenziat in Wirtschaftswissenschaften (Master in Finance and Capital Markets)
	WWZ, Basel University
	Thesis: Predictability of asset returns using liquidity measures.
	Supervisor: Heinz Zimmermann
1995-2000	Master (Diplom) in experimental physics, Basel University
	Thesis: Coulomb correlation in the DIRAC experiment
	Supervisor: Ludwig Tauscher
1994-1995	1. Vordiplom in Chemie (chemistry), University of Basel
1992-1998	IT and network support with Ciba-Geigy AG, Basel
1986-1994	Matura Typus B, Bäumlihof Gymnasium, Basel

The following professors contributed to my education:

C. Bandle, S. Borner, M. Bruhn, R. Capitelli, E. Constable, W. Drobetz, R. Frey, H.J. Güntherodt, E. Heri, J. Jourdan, H. Kraft, P. Kugler, C. Lenz, D. Loss, D. Masser, W. Müller, G. Plattner, H. Rudin, B. Scarpellini, H. Schierenbeck, P. Schiess, C. Schönenberger, I. Sick, T. Studer, L. Tauscher, F. K. Thielemann, D. Trautmann, C. Ullrich, R. Weder, B. Wöhle, H. Zimmermann, A. Zuberbühler.

Zusammenfassung

Die DIRAC Kollaboration versucht die Lebensdauer vom Pionium Atom, einem gebundenen Zustand aus π^+ und π^- , durch die Messung der Aufbruchwahrscheinlichkeit dieses Atoms zu bestimmen. Die Aufbruchwahrscheinlichkeitsmessung mit dem DIRAC Spektrometer am CERN sucht nach $\pi^+\pi^-$ Paare vom Aufbruch bei sehr kleinen relativen Impulsen (Q<4 MeV/c), welche zusätzlich zum dominanten Hintergrund aus korrelierten und unkorrelierten Pion Paaren aus der Protonenstrahl - Targetatom Interaktion detektiert werden. Die Zahl der gefundenen Pion Paaren, welche vom Aufbruch kommen, dividiert durch die Anzahl der produzierten Atome definiert die Aufbruchwahrscheinlichkeit. Die Zahl der produzierten Atome steht in Beziehung zur Anzahl der produzierten $\pi^+\pi^-$ Paare mit Coulombinteraktion im Endzustand da beide aus dem gleichen Produktionsprozess hervorgehen.

Die Messungen am Nickel Target entsprechen dem grössten homogenen von der DIRAC Kollaboration gemessenen Datenstück, was einen kleinen statistischen Fehler zur Folge hat. Systematische Einflüsse wurden untersucht und sind nicht dominant.

The Messung der Aufbruchwahrscheinlichkeit and darausfolgend die Bestimmung der Lebensdauer von Pionium erlaubt die Berechnung der Differenz zwischen der isoskalaren und isotensoriellen $\pi\pi$ Streulängen unter ausschliesslicher Benützung von Quantummechanik. Diese Berechnung kann benützt werden, um Voraussagen der Chiralen Störungsrechnung zu überprüfen.